university of groningen

umcg

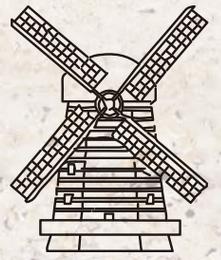
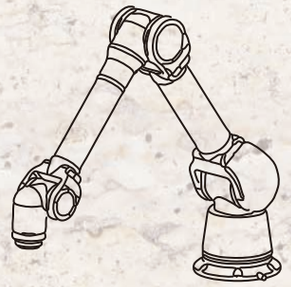

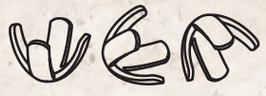

ISBN: 978-94-6536-204-5

Magnetic soft robots toward localized therapy: Magnetization Programming and Multimaterial Integration Zhuoyue Wang

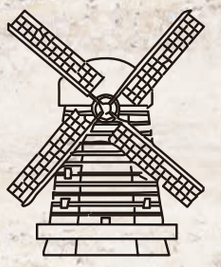

# Magnetic Soft Robots

## Toward Localized Therapy:

### Magnetization Programming and Multimaterial Integration

Zhuoyue Wang（王卓越）

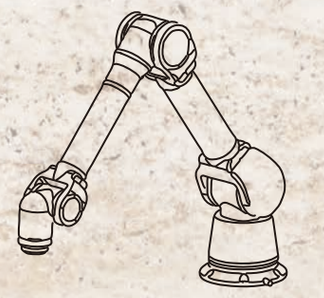

# Magnetic Soft Robots toward Localized Therapy: Magnetization Programming and Multimaterial Integration

*Zhuoyue Wang*

university of groningen

# Magnetic Soft Robots toward Localized Therapy:

# Magnetization Programming and Multi-material Integration

**PhD thesis**

to obtain the degree of PhD at the
University of Groningen
on the authority of the
Rector Magnificus Prof. J.M.A. Scherpen
and in accordance with
the decision by the College of Deans.

This thesis will be defended in public on

Wednesday 26 August 2026 at 12:45 hours

by

**Zhuoyue Wang**

born on 15 November 1995
in Pingliang, China

## Supervisor
Prof. S. Misra
## Co-supervisor
Dr. V. K. Venkiteswaran

## Assessment Committee
Prof. J.T.B. Overvelde
Prof. R. Schirhagl
Prof. A. Sadeghi

**This work is part of the research project MAESTRO.**

This work was supported by the European Research Council (ERC) under the European Union's Horizon 2020 Research and Innovation programme under grant 866494 project-MAESTRO, and financial support from the China Scholarship Council (CSC No. 202106180026) is acknowledged.

This dissertation has been approved by:

**Prof. Dr. Sarthak Misra**
**Dr. Venkatasubramanian Kalpathy Venkiteswaran**

Cover design: Zhuoyue Wang
Lay-out: Zhuoyue Wang
©2025 Zhuoyue Wang, The Netherlands. All rights reserved. No parts of this thesis may be reproduced, stored in a retrieval system or transmitted in any form or by any means without permission of the author. Alle rechten voorbehouden. Niets uit deze uitgave mag worden vermenigvuldigd, in enige vorm of op enige wijze, zonder voorafgaande schriftelijke toestemming van de auteur.

*Dedicated to my family*

# Samenvatting

Magnetisch aangedreven zachte robots worden steeds vaker beschouwd als veelbelovende systemen voor minimaal invasieve chirurgie en gelokaliseerde medische interventies. Hun vermogen om externe magnetische velden om te zetten in gecontroleerde vervorming en voortbeweging maakt draadloze, niet-gebonden werking zonder ingebouwde energievoorziening mogelijk. Dit is bijzonder voordelig in beperkte en vervormbare fysiologische omgevingen. Door magnetische deeltjes in zachte matrices in te bedden combineren deze systemen externe activering met mechanische flexibiliteit. Hierdoor kunnen zij door complexe biologische omgevingen navigeren terwijl structurele aanpasbaarheid behouden blijft. In recente studies zijn diverse vervormings- en voortbewegingsmechanismen aangetoond en zijn basisprincipes voor magnetische respons onder externe velden vastgesteld. De praktische toepassing van magnetische zachte robots in klinische contexten, zoals gelokaliseerde sensing, minimaal invasieve chirurgie en medicijnafgifte, wordt echter nog beperkt door twee belangrijke factoren: schaalbare driedimensionale magnetisatieprogrammering en betrouwbare integratie van meerdere materialen.

Programmeerbare driedimensionale magnetisatie is essentieel omdat deze bepaalt waar magnetische krachten en koppels in het systeem ontstaan. Daarmee worden vervormings- en voortbewegingsmodi, evenals de positioneringsnauwkeurigheid, bepaald die nodig zijn voor herhaalbare en plaatsspecifieke interventies. Het realiseren van dergelijke magnetisatiepatronen blijft echter uitdagend. De meeste magnetisatiemethoden werken namelijk globaal op al het aanwezige magnetische materiaal. Het assembleren van afzonderlijk gemagnetiseerde onderdelen om lokale magnetisatie te bereiken beperkt bovendien de structurele complexiteit en bemoeilijkt een nauwkeurige uitlijning en reproduceerbare fabricage. Tegelijkertijd is betrouwbare integratie van meerdere materialen cruciaal, omdat therapeutische systemen vaak functionele componenten bevatten, zoals geneesmiddelhoudende hydrogels, chemische sensoren en mechanische actuatoren. Het behouden van interfaciale stabiliteit en functionele betrouwbaarheid onder herhaalde mechanische belasting vormt hierbij een belangrijke uitdaging.

Dit proefschrift pakt deze uitdagingen aan door twee fabricagestrate-

gieën te ontwikkelen die zowel driedimensionale magnetisatieprogrammering als robuuste integratie van magnetische zachte materialen met verschillende substraten en functionele lagen mogelijk maken. De ontwikkelde concepten worden vervolgens gevalideerd in *in vivo*-experimenten waarin magnetisch gestuurde navigatie, positionering en gelokaliseerde therapeutische toediening worden aangetoond. De bijdragen van dit proefschrift worden in de verschillende hoofdstukken gepresenteerd, beginnend met fundamentele programmeer- en fabricagemethoden en eindigend met geïntegreerde systemen en toepassingsexperimenten.

**Hoofdstuk 2** introduceert een methode voor de schaalbare fabricage van magnetische zachte metamaterialen waarbij driedimensionale magnetisatie onafhankelijk van de structurele fabricage kan worden geprogrammeerd. Hiervoor wordt een voxelgebaseerde roosterstructuur gebruikt die de architectuur opsplitst in afzonderlijke responsieve modules. Elke module kan een vooraf bepaalde magnetisatierichting krijgen. De magnetisatie wordt na fabricage van de structuur geïntroduceerd met behulp van een fluïdische programmeermethode. Geselecteerde voxels worden gevuld met magnetische inkt, waarna de deeltjes tijdens het proces worden uitgelijnd en via opeenvolgende uithardingsstappen meerdere magnetisatierichtingen in één continue structuur worden vastgelegd. Deze aanpak maakt het mogelijk om elastische knik gecontroleerd te activeren door middel van magnetische velden. De resulterende instabiliteit versterkt de vervorming en maakt herconfigureerbare mechanische responsen en een schakelbare Poisson-ratio mogelijk bij relatief lage activeringsvelden. Deze methode vormt de basis voor de verdere fabricage- en integratiestrategieën die in de volgende hoofdstukken worden ontwikkeld.

**Hoofdstuk 3** presenteert een schaalbare fabricage- en magnetisatiebenadering gebaseerd op meerlagige zeefdruk. Met een laag-voor-laag depositieproces worden zachte robots vervaardigd met gepatroneerde magnetische elastomeren op verschillende substraatmaterialen. In deze aanpak wordt de magnetische oriëntatie direct geïntegreerd in de printsequentie. Door verschillende functionele materialen in zorgvuldig ontworpen patronen te combineren worden meerdere apparaatconcepten gedemonstreerd. Zo worden biomedische zachte robots geprint die zich onder magnetische activering in een vasculair model kunnen voortbewegen. Daarnaast worden zachte systemen met geïntegreerde elektronica ontwikkeld die tussen verschillende werkingsmodi kunnen schakelen. Ook worden bio-geïnspireerde

robots met fluorescente nagloeiing gerealiseerd voor visuele feedback. Deze demonstraties tonen de veelzijdigheid en schaalbaarheid van de meerlagige zeefdrukstrategie aan en vormen de technologische basis voor de *in vivo* therapeutische validatie die in het volgende hoofdstuk wordt gepresenteerd.

**Hoofdstuk 4** bouwt voort op de in de vorige hoofdstukken ontwikkelde fabricagemethoden en introduceert een biohybride magnetische dragerrobot voor microbiome-gebaseerde therapie bij colitis ulcerosa. De robot bestaat uit een magnetisch responsieve actuatielaag gecombineerd met een hydrogel die probiotische bacteriën bevat. Deze tweelaagse structuur maakt nauwkeurige magnetisch gestuurde voortbeweging mogelijk en maakt tegelijkertijd plaats-specifieke afgifte van probiotica mogelijk. *In vivo*-experimenten in een muismodel met DSS-geïnduceerde colitis tonen aan dat de probioticahydrogel-geïntegreerde drager een verbeterde lokalisatie en retentie in de dikke darm bereikt, wat resulteert in een duidelijk therapeutisch herstel. Deze resultaten laten zien dat magnetische zachte robots kunnen worden ingezet voor gelokaliseerde, niet-invasieve therapeutische toepassingen.

Ten slotte vat **hoofdstuk 5** de belangrijkste resultaten van dit proefschrift samen. De gecombineerde vooruitgangen op het gebied van driedimensionale magnetisatieprogrammering, schaalbare fabricage en multi-materiaalintegratie worden daarbij in samenhang besproken. Daarnaast worden toekomstige onderzoeksrichtingen geschetst voor de verdere ontwikkeling van programmeerbare magnetische zachte robots richting klinische toepassingen. Hierbij wordt met name aandacht besteed aan gesloten-lusregeling, robuuste bio-interfaces, steriliseerbaarheid en biocompatibiliteit, en integratie met bestaande medische procedures en werkprocessen.

# Summary

Magnetic soft robots have emerged as promising candidates for minimally invasive surgery and localized intervention. Their ability to convert externally applied magnetic fields into controlled deformation and locomotion enables wireless, untethered operation without on-board power, which is particularly advantageous in confined and deformable physiological environments. By embedding magnetic particles within soft matrices, these systems combine remote actuation with mechanical adaptability, allowing navigation through complex biological spaces while maintaining structural compliance. Diverse deformation and locomotion modes have been demonstrated in recent studies, and design principles for magnetic response under applied fields have been established. However, practical translation of magnetic soft robots toward clinical applications (e.g., localized sensing, minimally invasive surgery, and drug delivery) is still limited by two factors: scalable three-dimensional magnetization programming for controllable deformation and locomotion, and reliable multi-material integration for incorporating functional components.

Programmable three-dimensional magnetization is essential because it defines the deformation and locomotion modes by determining where magnetic torques and forces arise when the material is subjected to magnetic fields. The encoding of magnetization remains challenging because most magnetizing methods act globally on the entire magnetic material, and assembling separately magnetized components to localize magnetization compromises structural complexity, alignment, and manufacturing precision. In parallel, reliable multi-material integration is critical because therapeutic operation depends on the incorporation of functional materials or components (e.g., drug-loaded hydrogels, chemical sensing elements, and actuation mechanisms). It is challenging to keep interfacial integrity and functional stability under repeated loading.

This thesis addresses these challenges by introducing two fabrication strategies that enable controllable three-dimensional magnetization programming and robust integration of magnetic soft materials with diverse substrates and functional layers. These advances are validated through *in vivo* experiments that demonstrate magnetically guided navigation, posi-

tioning, and localized therapeutic delivery. The contributions of this thesis are presented across the chapters, moving from foundational programming and fabrication methods to integrated systems and application-level validation.

**Chapter 2** establishes a methodology for scalable fabrication of magnetic soft metamaterials while preserving three-dimensional magnetization programming that is decoupled from structural fabrication. This chapter uses a voxel-based lattice that partitions the structure into responsive modules, where each unit can be assigned a prescribed magnetization direction. In order to achieve this, the chapter establishes a fluidic programming method that encodes these directions after the lattice is formed. The selected voxel groups are filled with magnetic ink, particles are aligned during processing, and sequential curing fixes multiple magnetization directions within a single continuous structure. This framework is subsequently used to guide elastic buckling through magnetic actuation. The controlled instability amplifies deformation and enables reconfigurable responses and switchable Poisson's ratio under modest actuation conditions. Importantly, this three-dimensional magnetization programming capability provides a foundation for **Chapter 3** and **Chapter 4**, where the same magnetization principles are incorporated into scalable fabrication workflows and extended to integrated multi-material devices.

**Chapter 3** establishes a scalable fabrication and magnetic programming strategy based on multi-layer screen printing. A layer-by-layer deposition technique is developed to fabricate soft robots with patterned magnetic elastomers on various substrate materials. In this chapter, magnetic orientation is integrated directly into the printing sequences. By stacking different functional materials with carefully designed patterns, several devices are demonstrated. Biomedical soft robots are printed to travel within a vascular model under magnetic actuation. Soft devices integrated with on-board electronics are fabricated to switch among multiple operating modes. Bio-inspired robots are created with fluorescent afterglow for visual feedback. These demonstrations validate the versatility and scalability of the multi-layer screen-printing strategy and provide the fabrication and integration basis for the *in vivo* therapeutic validation presented in **Chapter 4**.

**Chapter 4** builds on the fabrication methods established in the previous chapters and develops a bi-layer biohybrid magnetic carrier robot

for microbiome-based therapy in ulcerative colitis. The robot integrates a magnetically responsive actuation layer with a bacteria-loaded hydrogel layer in a tightly coupled architecture. This bi-layer design enables precise, controllable locomotion together with site-specific release of probiotics. *In vivo* studies further show that the probiotic hydrogel–integrated magnetic carrier improves localization and retention in the colon, leading to a pronounced therapeutic recovery in a mouse model of colitis. This chapter provides a foundation for magnetic soft robots in localized, non-invasive diagnosis and therapy.

Finally, **Chapter 5** concludes the thesis by synthesizing the main contributions in three-dimensional magnetization programming, scalable fabrication, and multi-material integration for magnetic soft robots toward localized therapy. It consolidates the technical advances presented in the preceding chapters, from fluidic-based magnetization encoding and multi-layer screen-printing strategies to bio-hybrid system validation in *in vivo* intestinal therapy. Building on these results, this chapter further outlines future directions for translating programmable magnetic soft robots into clinically usable systems, with emphasis on closed-loop control, bio-interface robustness, sterilization and biocompatibility constraints, and integration within existing therapeutic workflows.

# Contents


**1 Introduction** **1**
1.1 Development of Magnetic Soft Robots . . . . . 1
1.1.1 Magnetic Programming and Actuating Mechanism . 4
1.1.2 Magnetic Soft Robots for Biomedical Applications . 6
1.2 Research Contribution . . . . . 8
1.3 Outline of the Thesis . . . . . 14
1.4 Research Framework Funding . . . . . 16
1.5 Scientific Output . . . . . 16
1.5.1 Peer-Reviewed Journal Articles . . . . . 16
1.5.2 Conference Proceedings . . . . . 17

**2 Fluidic control programming for 3D magnetic soft metamaterials with reconfigurable mechanical behaviors** **19**
2.1 Introduction . . . . . 20
2.2 Results and Discussion . . . . . 23
2.2.1 Design and fabrication of reconfigurable base unit . 23
2.2.2 Multi-step fluidic control programming and 3D magnetic orientation . . . . . 26
2.2.3 MSM lattice with switchable Poisson's ratio . . . . . 30
2.2.4 MSM lattice with reconfigurable orthotropic behaviors 33
2.2.5 MSMs with programmable mechanical-based functions 35
2.3 Conclusions . . . . . 38
2.4 Experimental procedures . . . . . 38
2.4.1 Preparation of magnetic composite . . . . . 38
2.4.2 Multi-step injection and weak field orientation . . . 39
2.4.3 *In situ* mechanical tests . . . . . 39
2.4.4 Finite element analysis . . . . . 39
2.4.5 Material mechanical characterization . . . . . 40

**3 Multi-layer screen-printing of magnetic soft robots with integrated materials and functions** **41**
3.1 Introduction . . . . . 42

3.2 Results . . . 45
3.2.1 Multi-layer screen-printing and magnetic programming . . . 45
3.2.2 Screen-printed MSRs with diverse patterns and substrate materials . . . 50
3.2.3 Screen-printing of magnetic soft gripper robots . . . 54
3.2.4 Multi-modal MSRs embedded with on-board circuitry 56
3.2.5 Bio-inspired magnetic soft robot with fluorescent coloration . . . 58
3.3 Discussion . . . 60
3.4 Materials and methods . . . 62
3.4.1 Ink Preparation . . . 62
3.4.1.1 Magnetic Ink Preparation . . . 62
3.4.1.2 Conductive ink preparation . . . 63
3.4.1.3 Fluorescent ink preparation . . . 63
3.4.2 Screen-Printing Procedures . . . 63
3.4.3 Magnetic programming . . . 63
3.4.4 Rheological Test . . . 64
3.4.5 Surface Morphology Test . . . 65
3.4.6 SEM Characterization . . . 65
3.4.7 Finite element analysis . . . 65
3.4.8 Material mechanical characterization . . . 65

**4 Biohybrid Magnetic Soft Robots for Targeted Microbial Colonization in Ulcerative Colitis Treatment 67**
4.1 Introduction . . . 68
4.2 Results and Discussion . . . 72
4.2.1 Fabrication and Characterization of MCRs . . . 72
4.2.2 Programmable Locomotion of MCRs . . . 75
4.2.3 Bacteria Releasing of Magnetic Carrier Robots . . . 79
4.2.4 *In Vivo* Therapeutic Effects of MCRs Delivered Probiotics Against DSS-Induced Ulcerative Colitis . . . 81
4.2.5 Gut Microbiota Restoration Mechanism of MCRs on UC . . . 84
4.3 Conclusion . . . 88
4.4 Materials and Methods . . . 90
4.4.1 Ink Preparation . . . 90

4.4.2 Screen-Printing Procedures . . . . . 90
4.4.3 Rheological Test . . . . . 91
4.4.4 SEM Characterization . . . . . 91
4.4.5 Material mechanical characterization . . . . . 91
4.4.6 Animal Experiment . . . . . 91
4.4.7 Histological Assessment . . . . . 92
4.4.8 Gut microbiota 16s sequencing assay . . . . . 92

**5 Conclusions** **95**
5.1 Three-dimensional magnetization programming based on fluidic control . . . . . 96
5.2 Scalable fabrication and multi-material integration based on multi-layer screen-printing . . . . . 96
5.3 Bio-hybrid magnetic soft robots for *in vivo* intestinal disease therapy . . . . . 97
5.4 Outlook . . . . . 98
5.4.1 From magnetization programming to therapy-oriented closed-loop control . . . . . 98
5.4.2 Multi-material integration under sterilization, biocompatibility, and payload performance constraints . . . 99
5.4.3 Clinical workflow integration and optimization with existing therapeutic procedures . . . . . 99

**References** **118**

**Acknowledgements** **119**

**About the author** **125**

# 1



# Introduction

## 1.1 Development of Magnetic Soft Robots

Soft, compliant materials are reshaping how robotic technologies can be introduced into the human body for diagnosis and therapy[1], [2]. In contrast to rigid instruments that interact with tissue through concentrated contact forces, soft robotic devices can deform continuously and conform to complex anatomy, enabling gentle and mechanically compatible interaction with organs and lumens. This capability is particularly relevant for localized interventions, where a device must navigate confined, deformable environments and operate safely at the target site while minimizing trauma to surrounding tissue. As biomedical care increasingly shifts toward minimally invasive and site-specific strategies such as targeted drug delivery, focal stimulation, and local sensing, soft robotic platforms offer strong potential to extend clinical functionality beyond what conventional tools can achieve.

Based on whether energy and control are delivered through physical connections, soft robots can be categorized into tethered and untethered systems. In the tethered class, actuation is typically provided through pneumatic lines, hydraulic circuits, electrical connections, or mechanical transmission elements. Pneumatic actuators can generate large deformations with simple structures and quick responses, which makes them common in bending fingers and continuum bodies, but the need for air supply, valves, and tubing increases system volume and constrains mobility[3]. Hydraulic actuation can deliver stronger forces and improved stiffness mod-

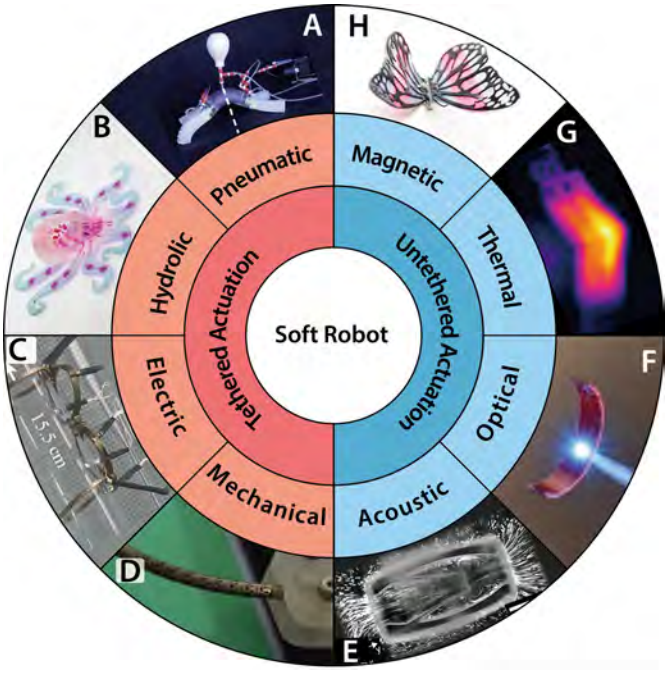


Figure 1.1: Overview of soft-robot actuation modalities grouped by energy delivery mode. Tethered actuation requires a physical connection to off-board sources and control hardware, including (A) pneumatically powered systems that inflate chambers to generate motion, reproduced from [3] under CC BY 4.0 license, (B) hydraulically driven robots that use pressurized liquids for high-force deformation, reproduced from [4], © 2016 Springer Nature, (C) electro-active actuators in which electrical input induces strain in functional polymers, reproduced from [5], copyright © 2011 IEEE, and (D) mechanically transmitted actuation where forces are delivered through cables, tendons, or rigid linkages, reproduced from [6], copyright © 2020, Sage Publications. Untethered actuation relies on remotely applied stimuli, including (E) acoustic excitation that induces vibration or streaming for propulsion and manipulation, reproduced from [7] under CC BY 4.0 license, (F) light-triggered actuation enabled by photo-responsive materials, reproduced from [8] under CC BY 4.0 license, (G) thermally driven systems that deform in response to heating through thermal expansion, reproduced from [9], copyright © 2016, American Chemical Society, and (H) magnetic actuation in which external magnetic fields generate programmable torque and force for controlled deformation and locomotion, reproduced from [10] under CC BY 4.0 license.

ulation compared with pneumatics, which is useful for load bearing tasks, yet the required pumps, reservoirs, and sealing hinder compactness and introduce concerns related to leakage and maintenance[4]. Electrically driven tethered systems utilize electro-active deformable materials such as ionic polymer metal composites (IPMCs), dielectric elastomers, and liquid crystal elastomers (LCEs)[5]. These materials can produce distributed strain and muscle-like motion under electrical stimulation and allow compact device layouts, but they often require high voltages or hydrated ionic environments, have constraints on long term stability and encapsulation, and still rely on wired power delivery for sustained operation. Mechanical approaches, including catheters and cables, can provide strong operation forces and reliable mechanical stability, but their reliance on continuous physical connections increases system bulk and limits miniaturization for deeply embedded or minimally invasive applications[6].

Untethered soft robots do not rely on physical connections to a power or actuation source. Instead, they receive energy input and control through external stimuli, such as sound, light, heat, and magnetic fields. For example, acoustic actuation, often implemented using ultrasound, can penetrate through fluids and can integrate naturally with medical imaging contexts, but it typically requires careful field shaping and remains sensitive to boundary conditions and coupling distance[7]. Light-driven approaches provide high spatial selectivity and remote triggering, which is attractive for patterned deformation; however, limited optical penetration and alignment constraints can reduce effectiveness in opaque environments and *in vivo* settings[8]. Thermal actuation can exploit phase transitions or temperature-dependent elasticity to achieve large strokes and strong holding states, but it is often constrained by heat-transfer rates and the need to manage temperature rise in surrounding media[9].

Among these approaches, magnetic actuation stands out for its ability to penetrate biological tissues with fast response and strong controllability[11]–[13]. Magnetic actuation supports wireless force and torque generation with minimal on-board components and can be controlled through programmed field sequences, enabling reversible shape change, steering, and locomotion. By embedding hard-magnetic particles or soft-magnetic fillers into soft polymers, the robot body can store a prescribed magnetization profile that converts external fields into programmable internal torques and forces. This strategy enables high-bandwidth control with-

out on-board batteries, supports miniaturization, and remains compatible with sealed and fully soft architectures, making magnetic actuation a particularly versatile approach for practical untethered soft robots. These characteristics are particularly valuable for localized therapy, where successful operation requires accurate positioning at the target site, controlled shape change or mechanical interaction in situ, and integration of therapeutic functions such as payload reservoirs, hydrogels, or sensing elements. Therefore, progress in magnetization programming and the development of robust multi-material integration strategies are essential for enabling magnetic soft robots to realize their full potential in localized therapy.

### 1.1.1 Magnetic Programming and Actuating Mechanism

Magnetic soft robots are typically realized by integrating magnetic components, such as hard-magnetic, soft-magnetic, or superparamagnetic fillers, into elastomers or hydrogels to form magnetically responsive composites. The actuation physics can be captured starting from a magnetic dipole with magnetic moment $\mathbf{m}$ placed in an external magnetic flux density $\mathbf{B}$ [14]. The dipole has magnetic potential energy

$$u_m = -\mathbf{m} \cdot \mathbf{B}. \tag{1.1}$$

Spatial variations in this energy yield a magnetic force

$$\mathbf{f}_m = (\nabla \mathbf{B})\, \mathbf{m}, \tag{1.2}$$

commonly written as

$$\mathbf{f}_m = (\mathbf{m} \cdot \nabla)\mathbf{B}, \tag{1.3}$$

while rotational variations yield a magnetic torque

$$\boldsymbol{\tau}_m = \mathbf{m} \times \mathbf{B}. \tag{1.4}$$

These expressions show two practical design principles. In a spatially uniform field, the net force vanishes and actuation is dominated by torque-driven reorientation. In a field gradient, torque can align the moment and force can translate the body toward increasing field strength, enabling combined shape change and locomotion.

To connect dipole-level behavior to continuum soft robots, the magnetic moment can be expressed as the volume integral of the magnetization $\mathbf{M}$ over the robot volume $V$:

$$\mathbf{m} = \int_V \mathbf{M}\, dV \tag{1.5}$$

In practice, hard-magnetic composites provide stable remanent magnetization below coercivity and thus generate predictable torque in uniform fields, while soft-magnetic or superparamagnetic composites often rely on induced magnetization and may require magnetic anisotropy to generate strong torque-based actuation.

At the continuum scale, magnetic soft robots deform because spatially distributed magnetic body forces and body torques generate internal stresses within the soft matrix. For a magnetized continuum subjected to an external magnetic field, the local magnetic torque density can be expressed as

$$\boldsymbol{\tau} = \mathbf{M} \times \mathbf{B}, \tag{1.6}$$

while the magnetic force density is given by

$$\mathbf{f} = (\mathbf{M} \cdot \nabla)\mathbf{B}. \tag{1.7}$$

These distributed loads enter the mechanical equilibrium equations as additional body terms and are balanced by elastic stresses in the surrounding polymer network. As a result, non-uniform magnetization or non-uniform magnetic fields generate internal stress gradients that bend, twist, stretch, or buckle the structure. In uniformly magnetized beams or sheets, a uniform external field primarily induces distributed torque, leading to bending or folding through magnetically induced curvature. In structures with programmed spatial variation of $\mathbf{M}$, differential torques arise between adjacent regions, enabling complex three-dimensional shape morphing. When a field gradient is introduced, the net magnetic force produces translational motion, allowing locomotion in addition to deformation. Therefore, magnetic programming defines the spatial distribution of $\mathbf{M}$, while the external field configuration determines whether the dominant response is reorientation, bending, buckling, or whole-body translation.

### 1.1.2 Magnetic Soft Robots for Biomedical Applications



Magnetic soft robots have attracted sustained interest for biomedical use because soft structures can reduce mechanical mismatch with tissue and magnetic actuation can enable wireless operation in confined anatomy. Various applications have been found in areas such as targeted drug delivery, minimally invasive therapeutic devices, steerable catheters, soft implantable systems, and reconfigurable electronic platforms.

For targeted transport, flexible magnetic nano-swimmers have been used to pick up drug-loaded polymeric particles and tow them under magnetic control, supporting directed delivery in biological media without chemical fuel [15]. For navigation across mixed terrains, a multi-modal magnetic miniature robot has combined helical swimming with bipedal walking to operate in open liquids, shallow layers, liquid surfaces, and solid substrates, enabling tasks such as targeted swimming, surface walking, and object retrieval [16]. Magnetic soft robots have also been explored as vehicles for transporting living therapeutics in restricted spaces. Super-soft and super-elastic magnetic hydrogel robots can navigate through narrow channels and unstructured obstacles by adapting their shape during locomotion, and cell delivery has been demonstrated using a 3D porous network with favorable biocompatibility [17]. Tissue sampling has been demonstrated using untethered micro-grippers that excise and retrieve specimens while preserving nucleic acid quality for downstream molecular analysis [18]. Temperature-responsive soft carriers have been proposed for gastrointestinal drug delivery, where shape recovery and magnetic responsiveness are combined to enable controlled release and improved retention in a large-intestine phantom environment [19]. Biodegradable multi-segmented magnetic soft robots have further been designed to dissolve and release payloads after magnetic navigation, supporting drug deployment in aqueous and mucus-like settings and highlighting the potential of transient materials for medical micro-robotics [20].

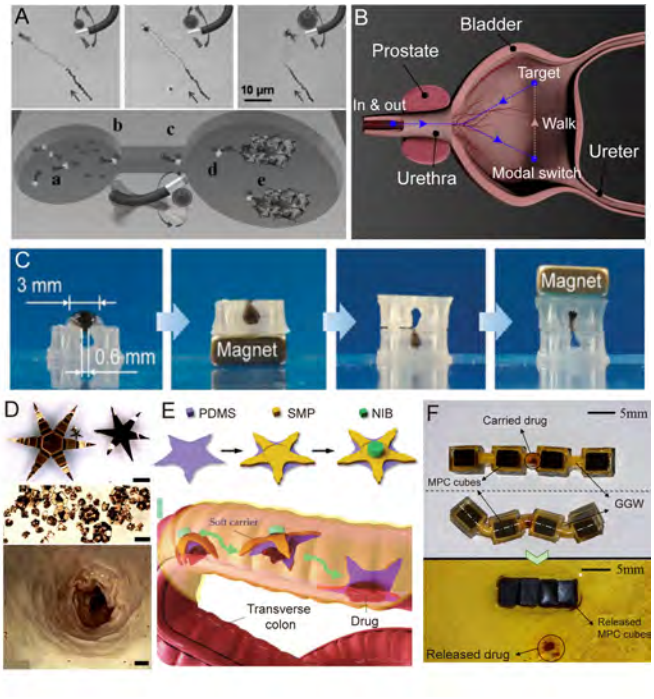


Figure 1.2: Representative biomedical applications of magnetic soft robots and microrobots. (A) Cargo towing and targeted delivery using fuel-free magnetic nanoswimmers that transport drug-loaded particles in biological media, reproduced from [15], copyright © 2012 WILEY-VCH Verlag GmbH & Co. KGaA, Weinheim. (B) Multi-modal magnetic miniature robot combines helical swimming and bipedal walking for stable amphibious navigation, reproduced from [16] under CC-BY-NC-ND license. (C) A super-soft and super-elastic magnetic hydrogel robot that performs magnetically driven navigation through confined paths to support cell delivery, reproduced from [17], copyright © 2019 Wiley-VCH Verlag GmbH & Co. KGaA, Weinheim. (D) Untethered micro-grippers for minimally invasive tissue sampling and retrieval, enabling distributed biopsy and downstream analysis, reproduced from [18], copyright © 2013 AGA Institute, published by Elsevier Inc. (E) A temperature-controlled gastrointestinal drug delivery concept based on a magnetically responsive soft carrier designed for locomotion and controlled release in the colon, reproduced from [19] under CC-BY-NC-ND license. (F) A multi-segmented magnetic soft robot that enables navigation and on-site payload release through a biodegradable and dissolvable architecture for medical use, reproduced from [20], copyright © 2022, IEEE.

## 1.2 Research Contribution



Despite rapid progress, several technical barriers continue to limit the broader deployment of magnetic soft robots, particularly in biomedical settings where reliability, reproducibility, and functional integration are required alongside wireless actuation.

The first challenge concerns three-dimensional magnetization programming at scale. Many established approaches remain constrained to effectively two-dimensional magnetization patterns, depend on assembling pre-magnetized components, or couple geometry formation and magnetic encoding in ways that restrict design freedom. As a consequence, achieving spatially addressable three-dimensional magnetization in complex architectures remains difficult, since magnetization is often coupled to geometry formation or constrained by fabrication-imposed directions, limiting design freedom in monolithic structures.

The second challenge lies in fabrication and magnetic programming with consistent quality across multiple devices. Techniques that enable high geometric resolution can be limited in throughput, whereas faster manufacturing routes may struggle to maintain pattern fidelity, inter-layer alignment, and uniform magnetic encoding. For practical deployment, these sources of variability translate into device-to-device differences in deformation modes, actuation thresholds, and repeatability, thereby weakening the robustness of experimental outcomes and complicating downstream validation.

The third challenge is the robust integration of magnetic composites with functional materials. Many application scenarios require magnetic actuation layers to be combined with drug-loaded hydrogels, conductive inks, or sensing elements, yet such integration introduces competing constraints. Interfaces between dissimilar materials can be mechanically fragile in wet and dynamic environments, and added functional layers can alter stiffness and damping, thereby reducing actuation efficiency or shifting deformation modes. Overcoming these limitations requires material and structural strategies that accommodate mechanical mismatch, stabilize interfaces in wet environments, and maintain both actuation performance and the intended functions of integrated layers.

Motivated by these considerations, this thesis aims to unify three-dimensional magnetization patterning, manufacturable fabrication strate-

gies, and robust multi-material integration to advance magnetic soft robots toward localized therapy and other application-oriented use cases. Accordingly, three research contributions (**RCs**) are formulated.



RC.1

Establish a scalable three-dimensional magnetization programming methodology

In **RC.1**, we address a key challenge in magnetic soft robots: how to program spatially varying magnetization in three-dimensional architected structures. We introduce a fluidic programming workflow that defines magnetic domains inside a single voxel-based lattice. The method combines controlled material filling, magnetic-field alignment of particles, and stepwise curing to lock in the desired directions. Because the lattice is fabricated first and magnetization is assigned afterward, the workflow reduces conflicts that often arise during post-assembly magnetization and supports multiple magnetization directions within one structure. Using this capability, we guide elastic buckling with external magnetic fields to amplify deformation, enabling lattices with reconfigurable mechanical responses under modest actuation. The contribution is developed along the following aspects:

(1) **Voxel-based architected metamaterial design for addressable magnetic domains.** We introduce a lattice architecture composed of programmable voxels and soft linking members, where each voxel serves as an individually assignable magnetic building block, enabling systematic construction of complex 3D magnetic layouts.

(2) **Fluidic control programming for selective voxel filling in three dimensions.** A multi-step injection strategy is developed to distribute magnetic composites into prescribed voxel groups inside the 3D lattice. By leveraging controlled flow paths and staged injections, targeted regions can be filled without contaminating neighboring domains, forming the basis for spatially localized magnetic programming within a monolithic body.

(3) **Sequential magnetic encoding without post-assembly conflicts.** For each programmed region, magnetic particles are oriented under a controlled external field to set the desired magnetization direction, and then cured to lock in the assigned magnetic moment. Repeating this se-

quence across voxel groups enables multiple embedded magnetization directions within one structure, including patterns that vary through thickness and along all three spatial axes. The workflow avoids the interference and misalignment that commonly arise when assembling pre-magnetized components.

(4) **Magnetic-field-guided elastic buckling and reconfigurable mechanics.** We leverage magnetic-field-guided elastic buckling to amplify actuation, where the programmed magnetization distribution steers the onset and mode of instability. This mechanism enables pronounced and switchable deformation responses, including rapid transitions between positive and negative Poisson's ratios and orthotropic, mode-dependent behaviors. These results demonstrate how 3D magnetization patterns can function as a control layer over metamaterial mechanics.

Overall, **RC.1** presents a transferable approach that treats magnetization as a key design variable in soft architected matter. First, it helps connect prescribed magnetization patterns to manufacturable 3D structures by enabling magnetization to be assigned within an already formed body at the level of voxel groups. This method reduces dependence on printing direction, single-axis magnetization, and post-assembly alignment. As a result, geometry can be chosen to tune mechanical properties such as compliance, anisotropy, and multi-stability, while magnetization can be selected with greater independence to meet actuation and control objectives. Second, the workflow offers a scalable route for programming magnetic soft systems. The repeated sequence of filling, alignment, and curing supports iteration, correction, and hierarchical patterning, which becomes increasingly important as designs grow in size and complexity. Third, using buckling as an amplification mechanism can enable large and switchable shape changes under modest fields, which is beneficial for untethered operation when field strength and available power are limited. More broadly, **RC.1** provides a magnetization programming and mechanics framework that can be adapted for manufacturable robotic prototypes and multi-material devices. It serves as a technical foundation for later contributions on scalable fabrication in **RC.2** and application-driven integration in **RC.3**, and may also be relevant to soft metamaterials, reconfigurable structures, and field-controlled machines operating in confined or unstructured settings.

RC.2

Develop a compatible fabrication and magnetic programming pipeline using multi-layer screen-printing



In **RC.2**, the limitations hindering the scalable deployment of magnetic soft robots, including low fabrication throughput, inconsistent actuation performance, and the challenge of integrating functional materials with diverse substrates, are addressed. A multi-layer screen-printing manufacturing strategy is established to fabricate magnetic soft robot bodies through layer-by-layer deposition and controlled curing, ensuring high pattern fidelity and precise inter-layer registration. To achieve rapid and reproducible magnetic encoding, a streamlined programming approach is developed through local magnetic reorientation for fast alignment. Most significantly, the seamless integration of heterogeneous substrates and functional layers, such as embedded circuitry and fluorescent materials, is demonstrated while maintaining precise programmable deformation and repeatable actuation performance.

(1) **Multi-layer screen-printing process for magnetic soft robot bodies.** We develop a layer-by-layer deposition and curing workflow that enables rapid fabrication of soft robotic architectures with controlled thickness, geometry, and material composition. The approach is designed to be compatible with magnetic-particle filled elastomers and to support repeatable transfer of fine features from the screen to the printed part.

(2) **Pattern fidelity and inter-layer registration for reliable device geometry.** We introduce printing and alignment strategies that preserve feature sharpness and dimensional accuracy across multiple layers. Registration is maintained through controlled alignment references and process parameters that reduce layer shift, distortion, and cumulative error, which is critical for devices whose actuation depends on consistent geometry and domain placement.

(3) **Batch-compatible magnetic programming for repeatable actuation.** We implement magnetic reorientation to rapidly align particles locally within printed magnetic regions, enabling efficient programming that is compatible with planar printed architectures. For designs requiring stronger magnetization and robust responses, we apply impulse magnetization to encode complex geometries with high magnetic moments. Together,

these methods provide a practical route to consistent magnetization assignment and reduced performance variance across batches.

Overall, **RC.2** addresses an important challenge in magnetic soft robotics, namely reliable multi-material integration that preserves actuation performance, interfacial integrity, and functional compatibility. A multi-layer screen-printing process is developed to assemble magnetic elastomers with a wide range of substrate and functional layers. This process enables patterned magnetic regions to be deposited and programmed directly on non-traditional substrates, including paper, fabric, and rigid surfaces, so that otherwise passive materials can exhibit magnetically driven deformation. In addition to substrate versatility, **RC.2** enables hybrid stacks that integrate functional layers such as conductive circuitry and fluorescent components, expanding magnetic soft robots beyond purely mechanical actuation toward devices that combine actuation with sensing, signaling, and interface functions.

Magnetic reorientation provides rapid local particle alignment that is compatible with the speed and parallelism of screen printing, and impulse magnetization enables strong and reliable actuation for designs that require high magnetic moments. By improving layer registration, geometric fidelity, and batch repeatability across heterogeneous materials, **RC.2** supports scalable fabrication of integrated magnetic soft robotic systems. This integrative capability enables application-oriented platforms, including the multi-material therapeutic devices in **RC.3**, where stable layer interfaces, repeatable magnetic responses, and scalable production are required. More broadly, **RC.2** provides a practical foundation for standardized and cost-effective fabrication of magnetic soft robots that integrate actuation with functional materials, supporting future biomedical devices for localized diagnosis and therapy.

RC.3

Develop Biohybrid Magnetic Carrier Robots for Localized Probiotic Therapy

In **RC.3**, we translate magnetically actuated soft robotics into a biohybrid therapeutic platform by integrating a probiotic-loaded hydrogel and validating its performance under simulated gastrointestinal conditions. We develop a screen-printed magnetic carrier robot that combines a magneti-

cally responsive NdFeB/PDMS elastomer layer for wireless actuation with a probiotic-loaded alginate hydrogel layer that protects bacteria from gastrointestinal stresses and enables localized release. The system is evaluated on colon-mimicking tracks and within a colon phantom under real-time visualization to verify controllable navigation and positioning in confined, wet, and deformable environments. It is further validated in a DSS-induced colitis mouse model, where magnet-localized delivery improves therapeutic outcomes and remodels the gut microbiota more effectively than non-localized controls. The contribution is developed along the following aspects:

(1) **Therapeutic carrier design based on screen-printed multi-material stacking.** We establish a layered carrier architecture that combines a magnetic elastomer actuation layer with a hydrogel payload layer in a single compact device. The design is compatible with scalable printing and enables geometric definition of both locomotion features and drug or probiotic reservoirs.

(2) **Precise patterning and interfacial reliability for operation in aqueous gastrointestinal conditions.** We develop fabrication and bonding strategies that maintain stable interfaces between the NdFeB PDMS layer and the alginate hydrogel layer. The printed patterns preserve functional separation between actuation and payload regions, while resisting delamination, swelling induced distortion, and mechanical fatigue during repeated magnetic actuation in wet conditions.

(3) **Wireless locomotion and controllable positioning under real time visual guidance.** We demonstrate magnetic actuation that enables directed movement, steering, and stable positioning along colon mimicking tracks and inside a colon phantom. Real-time visualization supports closed loop operator guidance and provides evidence that the carrier can be navigated to target regions and held in place to support localized release.

(4) **In vitro protection and localized release performance of probiotic payloads.** We show that the alginate hydrogel layer functions as a protective microenvironment for probiotic viability under gastrointestinal stresses, while enabling spatially confined delivery. The carrier design supports retention of payload during navigation and release upon reaching the target site, providing a practical route to improve local colonization.

**RC.3** advances magnetic soft robots toward localized therapeutic de-

livery by developing and validating a biohybrid magnetic carrier system under gastrointestinal conditions. It shows how magnetic actuation and hydrogel-based payload protection can be implemented together in a manufacturable bi-layer design to enable controllable navigation, positioning, and localized release. Specifically, a screen-printed carrier robot is developed that combines an NdFeB/PDMS magnetic elastomer layer for wireless actuation with a probiotic-loaded alginate hydrogel layer that protects bacteria from gastrointestinal stresses and supports localized deposition. The system is evaluated on colon-mimicking tracks and in a colon phantom under real-time visualization, demonstrating controllable motion and reliable positioning in gastrointestinal environments. An *in vivo* study in a DSS-induced colitis mouse model further indicates that magnet-localized delivery improves retention and therapeutic outcomes compared with non-localized controls, supporting the use of targeted microbial delivery as a practical therapeutic strategy.

Taken together, these research contributions establish a coherent progression from three-dimensional magnetization programming to scalable fabrication and, finally, to integrated bio-functional systems validated in application-relevant settings.

## 1.3 Outline of the Thesis

This thesis is organized into five chapters that collectively address key research questions in magnetic soft robotics and advance toward application-ready systems. **Chapters 2–4** consist of research studies published in peer-reviewed journal articles.

**Chapter 1** introduced the background of soft robotics and motivates magnetic actuation for untethered operation. It summarizes the state of the art in magnetic soft robots, focusing on actuation principles, magnetization strategies, fabrication routes, and representative biomedical applications. The chapter then identifies three core limitations that motivate this thesis, namely scalable 3D magnetization programming, batch-compatible fabrication and magnetization, and robust multi-material integration. Finally, it presents the three research objectives and the overall thesis structure.

**Chapter 2** links to **RC.1** by establishing a scalable strategy to encode three-dimensional magnetization profiles in architected soft metamaterials, creating the magnetic-programming and structural-design foundation that

later enables manufacturable robotic systems in **Chapters 3** and **Chapter 4**. It develops a scalable approach to encode three-dimensional magnetization profiles in architected soft metamaterials. It introduces a voxel-based metamaterial design and a fluidic control programming workflow that enables selective definition of magnetization domains within a monolithic structure. By decoupling geometry formation from magnetic encoding, the method expands design freedom for complex 3D bodies while avoiding assembly-induced magnetization conflicts. The chapter then demonstrates magnetically triggered deformation modes enabled by the programmed magnetization distribution, including reconfigurable mechanical responses driven by magnetic-field-guided instability and buckling.

**Chapter 3** links to **RC.1** and **RC.2** by translating the 3D magnetic-encoding concepts from **Chapter 2** into a high-throughput, multi-layer screen-printing manufacturing pipeline, and it directly sets up the fabrication and integration route used for the therapeutic system in **Chapter 4**. It addresses **RC.2** by establishing a high-throughput manufacturing pipeline based on multi-layer screen printing. It details the layer-by-layer deposition strategy for forming magnetic soft robots with controlled geometry, patterned magnetic regions, and consistent inter-layer registration. The chapter further presents magnetic programming approaches that are compatible with printed architectures and enable reproducible actuation across batches. In addition, it shows how the screen-printing platform supports integration of multiple functional layers, providing a manufacturable route toward multifunctional magnetic soft robots.

**Chapter 4** links to **RC.2** and **RC.3** by leveraging the multi-material screen-printing and magnetic programming capabilities developed in **Chapter 3** to realize a clinically relevant, targeted therapeutic application, while also reflecting the broader multifunctional surgical-robotics motivation underlying the thesis. It addresses **RC.3** by demonstrating robust multi-material integration in a clinically relevant therapeutic application. It presents a screen-printed magnetic carrier robot that integrates a magnetically responsive elastomer layer for wireless actuation with a probiotic-loaded hydrogel layer for protection and localized release. The chapter reports controlled navigation and positioning in colon-mimicking settings under visual guidance and evaluates functional performance in an *in vivo* colitis model. The results illustrate how manufacturable magnetic robots can achieve localized therapeutic delivery and highlight design considera-

tions for interfacial reliability and material stability in aqueous gastrointestinal environments.

Finally, we consolidate the key outcomes of this thesis, with a specific emphasis on application-oriented design and fabrication strategies for magnetic soft robotics spanning three-dimensional magnetization programming, scalable fabrication and magnetic encoding, and multi-material integration for targeted use cases in **Chapter 5**. It then discusses the remaining barriers to translation, including closed-loop control, robustness across anatomical variability, and standardization for batch manufacturing, and concludes by outlining future directions toward magnetic soft robots that unify programmable magnetization, manufacturable processes, and integrated therapeutic and diagnostic functions.

## 1.4 Research Framework Funding

All the research studies that constitute this doctoral thesis have been supported by funds from the European Research Council (ERC) under the European Union's Horizon 2020 Research and Innovation programme under grant 866494 project-MAESTRO, and financial support from the China Scholarship Council (CSC No. 202106180026 ). All the studies presented in this thesis have been performed with the experimental setups at the Surgical Robotics Laboratory (SRL), in the Department of Biomaterials and Biomedical Technology (formerly known as the Department of Biomedical Engineering) of the University of Groningen and University Medical Center Groningen, Groningen, the Netherlands.

## 1.5 Scientific Output

The studies conducted during this doctoral degree are part of the articles published in the following journals:

### 1.5.1 Peer-Reviewed Journal Articles

1. **Z. Wang**, L. Ding, S. Misra, and V. K. V. Venkiteswaran, *"Magnetic Soft Robots for Targeted Microbial Colonization in Ulcerative Colitis Treatment"*, Under review by Materials Today Bio, 2026.

2. **Z. Wang**, S. Misra, and V. K. V. Venkiteswaran, *"Multi-layer Screen-Printing of Magnetic Soft Robots with Integrated Materials and Functions"*, Cell Reports Physical Science, 6: 102614, June 2025.

3. **Z. Wang**, S. Misra, and V. K. V. Venkiteswaran, *"Fluidic Control Programming for 3D Magnetic Soft Metamaterials with Reconfigurable Mechanical Behaviors"*, Cell Reports Physical Science, 2024.

4. C. M. Heunis, **Z. Wang**, G. de Vente, S. Misra, and V. K. V. Venkiteswaran, *"A Magnetic Bio-Inspired Soft Carrier as a Temperature-Controlled Gastrointestinal Drug Delivery System"*, Macromolecular Bioscience, 23: 2200559, 2023.

### 1.5.2 Conference Proceedings

1. **Z. Wang**, *"3D Metamaterial with Magnetically Programmable Mechanical Behaviors"*, Dutch Soft Robotics Symposium 2023, March 25th–28th, 2025, Groningen, the Netherlands. (Poster Presentation)

2. **Z. Wang**, *"3D Metamaterial with Magnetically Programmable Mechanical Behaviors"*, Euromech 659 – Metamaterials in Fluid Flows and Beyond, May 16th–17th, 2023, Twente, the Netherlands. (Poster Presentation)

# 2



# Fluidic control programming for 3D magnetic soft metamaterials with reconfigurable mechanical behaviors

***Note:*** *The following chapter is adapted from the article "Fluidic control programming for 3D magnetic soft metamaterials with reconfigurable mechanical behaviors" by* ***Z. Wang****, S. Misra, and V.K.Venkiteswaran , published in "Cell Reports Physical Science", volume 5, issue no. 8, August 2024.*

Active mechanical metamaterials are an attractive proposition for soft robotics, electronic devices, and biomedical devices. However, the utilization of their uncommon physical and mechanical behaviors remains underexplored because existing fabrication processes limit the decoupling of structural frameworks from the responsive mechanisms. Herein, we propose a multi-step fluidic control programming strategy, fabricating 3D magnetic soft materials (MSMs) with reconfigurable mechanical metamaterial behaviors, enabling magnetic field-driven alteration between three different geometry modes in a single structure. The MSM lattices exhibit fast 3D transitions between positive ($\nu_{max}$ = 3.41) and negative Poisson's ratio ($\nu_{max}$ = -2.64). We then create MSMs with reconfigurable orthotropic behaviors, which demonstrate the positive and negative Poisson's effect in perpendicular planes. In further demonstrations, fast and wireless response is validated by manipulation of falling loads and switching the states of electrical circuits. This research provides a controllable workflow for future magnetic soft metamaterials.

## 2.1 Introduction

The development of intelligent technologies in industries such as automation, aerospace, electronics, and biomedicine places tremendous demand on the mechanical features of metamaterials[21]. Mechanical metamaterials with rationally designed structures offer great possibilities for programming shape change and variable macro-level material response[22], [23]. Unique properties are proven in mechanical metamaterials such as negative Poisson's ratio (auxetic)[24]–[28], negative stiffness[29], [30], negative thermal expansion[30]–[32], and twist under compression[33]. In many of these cases, the properties remain invariable after fabrication, as they are embedded within the structure of the materials. To enable the alteration of mechanical properties after fabrication, recent advances have employed stimuli-responsive materials such as shape memory polymers (SMPs)[34]–[38] , which the shape can be reprogrammed when heated above the critical temperature; hydrogels that can absorb or lose water molecules; and magnetic materials such as permanent magnets[39], [40] and magnetic soft materials (MSMs)[41]. These materials are often limited by their uniform response mode and the ability to form complex 3D structures.

Due to the rapid and wireless response in external magnetic fields, magnetic soft materials have attracted widespread interest, particularly in biomedical applications[13], [42]–[47]. Polydimethylsiloxane (PDMS) and Ecoflex are frequently used as the matrix for magnetic fillers, which can incorporate both soft and hard magnetic particles[48]. By implanting specific magnetization patterns into the materials, these soft materials can perform geometric deformations, including bending[49], [50], twisting[51], and folding[50], [52]. Generally, magnetic soft materials are shaped into wires[53], films[54], [55], cubes, origami structures[56]–[58] and lattices[39], [59] via various fabrication methods such as molding and casting[60]–[62], additive manufacturing (3D printing)[51], [53], [63]–[65], 3D micro assembling[13], and reorientation of magnetic dipoles[66], [67]. However, current fabrication techniques lack either automated workflow to build 3D structures or cannot produce 3D magnetization patterns[41], although the decoupling of structural fabrication and patterned magnetization is essential for introducing the necessary complexity and controllability for 3D magnetic-responsive metamaterials. To address this challenge, we present a strategy to imbue 3D magnetization patterns into soft metamaterial structures and achieve

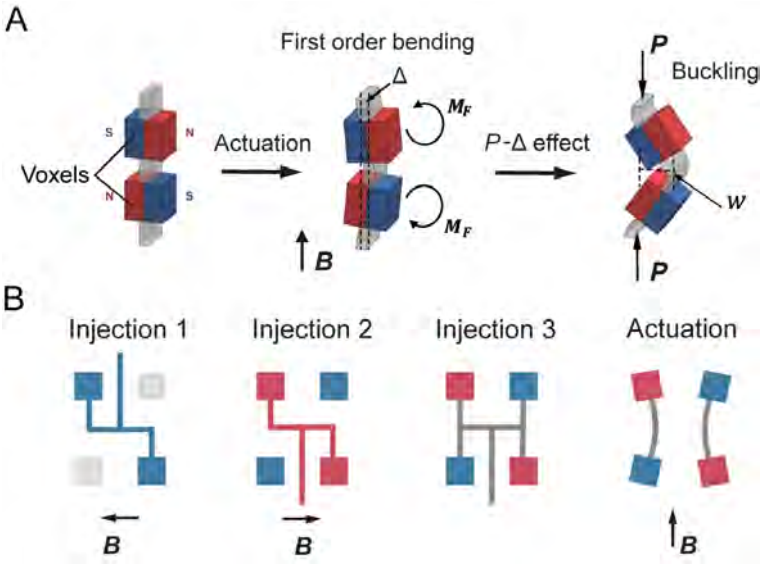


Figure 2.1: Design and fabrication of the reconfigurable base unit of magnetic soft metamaterials (MSMs). (A) Schematic diagrams illustrate the mechanism of magnetic field-guided buckling on a single beam. (B) Schematics of the concept of multi-step injection and orientation.

multi-modal deformation in three dimensions. First, MSMs are designed with stimuli-responsive voxels that can be regulated for specific magnetic moments in each segment. The segments are able to show a magnetic actuation-guided elastic buckling behavior based on a second-order effect (P-$\Delta$ effect), and the buckling direction can be controlled by the direction of the magnetic field (Figure 2.1A). To realize the individual programming of each voxel, we developed a fluidic injection technique, allowing specific voxels to be selectively filled and magnetized in disparate directions by two separate injections (Figure 2.1B). Subsequently, a third injection connects all voxels by filling the remaining spaces with non-magnetized composite material, ensuring structural continuity throughout the lattice.

Here, a systematic fabrication method based on multi-step injection and orientation of the particles in a weak field (80 mT) is developed. The voxel-dominated segments are magnetized and assembled in groups by the programming of fluidic injection channel and magnetic orientation procedures (Figure 2.2A). This approach allows multiple magnetization di-

rections embedded in the same structure without the need for assembly afterward. By assembling the segments in a pre-defined order, magnetically programmable mechanical behaviors, for instance, switching between negative and positive Poisson's ratio, are achieved (Figure 2.2B). Since the composite in each step is fully cured before injection in the next step, the conflict of magnetization directions is avoided between the adjacent elements. This fluidic control programming strategy solves the integration problem of fabricating 3D structures and 3D magnetization on arbitrary directions and creates MSMs showing unique mechanical behaviors.

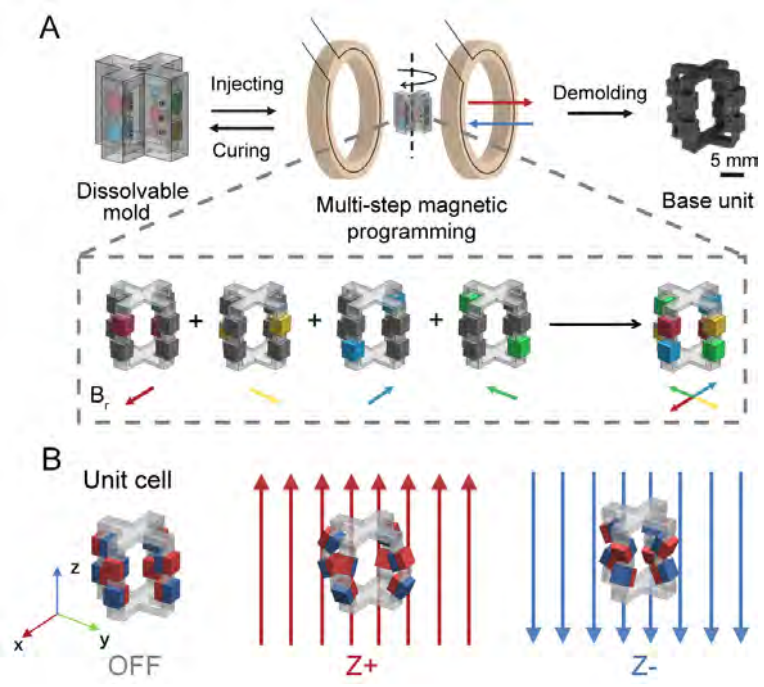


Figure 2.2: Mechanical behavior of the MSMs. (A) Iterative fluid injection programming procedure of the MSM base unit. The directions are represented by four colors (red, yellow, blue, and green). (B) Schematic diagrams illustrate the base unit when the external magnetic field is turned off (defined as OFF), upward (defined as Z+), and downward (defined as Z-).

Due to the carefully designed structures and magnetization patterns, the metamaterials exhibit sensitive responses and perform rapid switch-

ing between negative and positive Poisson's ratio and orthotropic shape-changing. This swift switching feature is further proven using a load-carrying metamaterial unit falling under gravity through a tube. We perform a series of in situ mechanical tests to characterize these behaviors in the presence of an upward vertical magnetic field (defined as Z+), a downward magnetic field (defined as Z-), and when the magnetic field is completely switched off (defined as OFF). A demonstration of our MSM lattice shows the ability to control electrical circuits with external magnetic fields. The reconfigurability of MSMs holds great potential in advancing the field of soft robots and electronics.



## 2.2 Results and Discussion

### 2.2.1 Design and fabrication of reconfigurable base unit

To achieve three-dimensional responsive deformation, we design a base unit with four segments composed of magnetically responsive voxels and linking members. In this base unit, each voxel can be magnetized in an individual direction using the fluidic control programming method developed in this study. With an alternating magnetization pattern, a lateral bending deflection is generated in the segments due to the effect of magnetic moment. By assembling the magnetized segments, variable bending modes can be achieved. Here, we use four segments with the magnetization pattern illustrated in Figure 2.1A to realize MSM units with switchable Poisson's ratio behavior.

To evaluate the programmable bending behavior, we introduce the concept of magnetic field-guided elastic buckling. Here, a programmable deformation mode of the base unit is achieved by controlling the direction of the magnetic moment via an external field and can be calculated by Equation 2.1.

$$M_{\mathrm{F}} = \mathbf{m} \times \mathbf{B} \tag{2.1}$$

where $M_F$ is the magnetic torque (N·m), $\mathbf{m}$ is the magnetic dipole moment (A·m$^2$), and $\mathbf{B}$ is the applied magnetic flux density (T). It is worth mentioning that the magnetic field provides the first-order bending moment, thereby eliminating the uncertainty in the buckling direction. When the magnetic field is turned on, each beam segment is in a slight bending equilibrium with an initial deflection $\Delta$. The addition of a further compressive

load leads to an amplification that tends to produce buckling behavior under a second-order effect (P-$\Delta$ effect) as described by beam-column theory[68] with the differential Equation 2.2:

$$EIw'''' + Pw'' = 0 \tag{2.2}$$

Where $E$ is the elastic modulus of the composite material [Pa], $I$ is the polar moment of inertia of the beam on the bending axis [$m^4$], and $P$ is the vertical compression load [N], and w is the deflection at mid-span of beam [m].



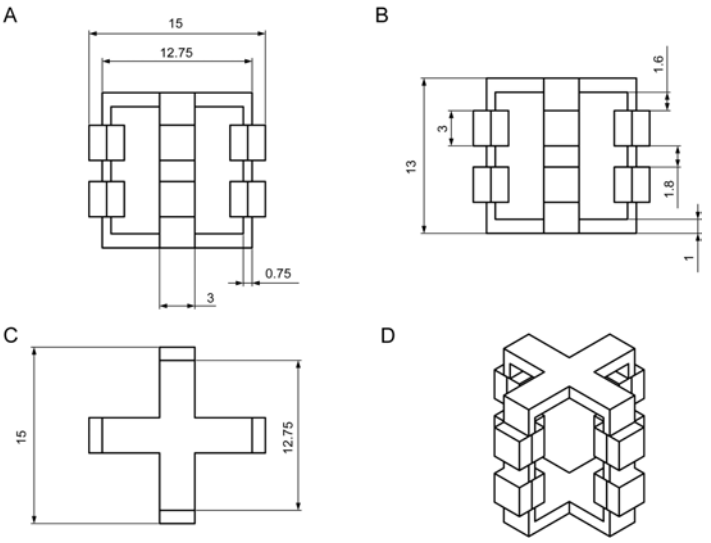


Figure 2.3: Geometrical design of the programmable metamaterial lattice. (A) Front view. (B) Side view. (C) Top view. (D) Isometric view. Unit, mm.

The base unit consists of four groups of magnetized segments, where each segment comprises two magnetic-responsive voxels (Figure 2.3). To magnetize the voxels, we sequentially deploy four steps of material injection followed by orientating and curing in a pair of Helmholtz coils. For the base unit, each voxel is magnetized to generate a magnetic moment of equal magnitude but opposite direction to its neighbor.

In mechanical tests, the programmable base unit shows a tri-state mechanical behavior where its deflection mode under compression can be altered by external magnetic fields (Figure 2.4). When the external magnetic

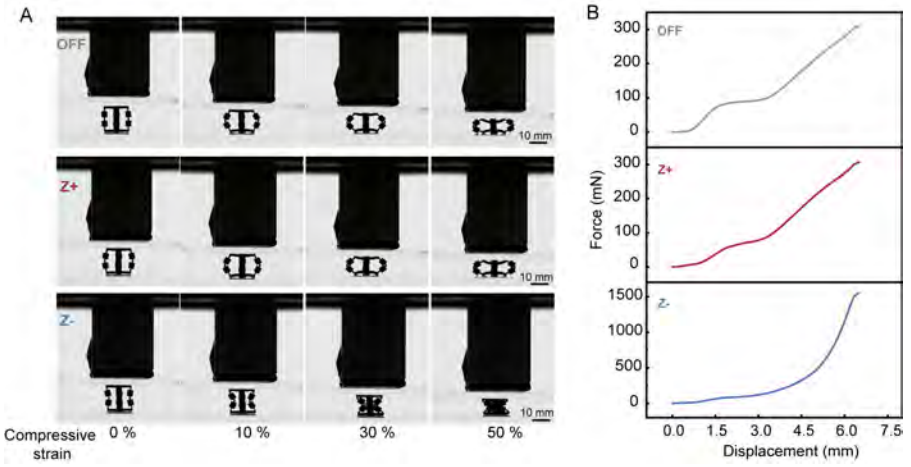


Figure 2.4: Mechanical tests of magnetic soft metamaterials (MSMs) base unit sample compressed in different magnetic field conditions. Magnetic fields are applied in vertical directions where the upward direction is defined as Z+, and the downward direction is defined as Z-. Scale bar, 10 mm.

field is OFF, the unit exhibits a positive Poisson's ratio ($\nu_{max}$ = 3.47) due to the constrained mode. Instability behavior is observed with a critical load of 66 mN. Pre-deformed curvature is observed in both Z+ and Z- fields at a flux density of 50 mT. Positive Poisson's ratio ($\nu_{max}$= 3.82) and a critical load of 58 mN are observed in the Z+ field. The Poisson's ratio can be switched to negative ($\nu_{max}$ = -4.52) by applying a Z- field with a critical load of 76 mN (Figure 2.5). Also, the unit shows a higher stiffness when the field is turned to Z-. This is because, in the negative Poisson's ratio state, the voxels contact and lock each other when moving to the center of the unit, as the deformation space is compressed. For the silicone matrix, Dragon Skin 30 was selected, and other materials such as PDMS or Ecoflex are also possible.

To better evaluate the magnetic-mechanical performance, tensile tests have been performed on the Dragon skin 30 and the magnetic composite samples which are prepared according to tensile test standards. Nominal stress-nominal strain curves are shown in Figure 2.6A. The magnetic flux density of a two-voxel beam (one segment) bending in the presence of a 50 mT magnetic field is simulated Figure 2.6B). The bending curvature and

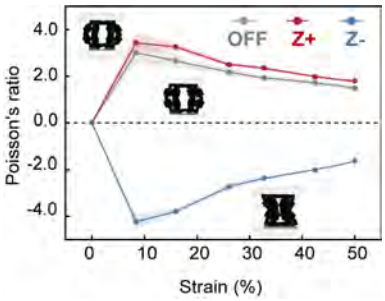


Figure 2.5: Poisson's ratio-strain curve of programmable MSM unit.

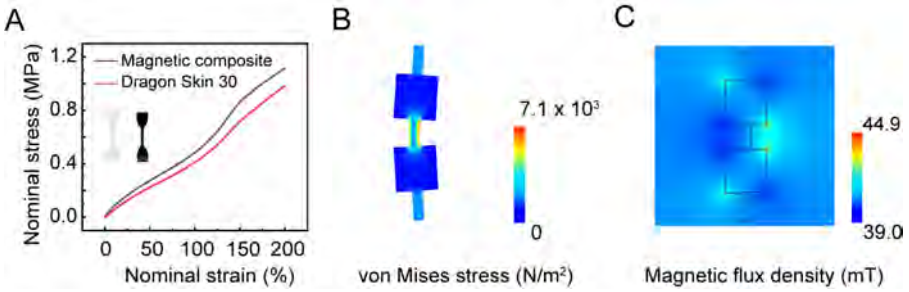


Figure 2.6: Test and simulation of mechanical properties of MSM segment. (A) Nominal stress - Nominal strain curves of Dragon skin 30 and the magnetic composite. (B) Simulation of the magnetic flux density of one segment. (C) Simulation of the segment under magnetic field-driven bending.

stress state of one segment in a vertical magnetic field are then simulated in Figure 2.6C. When fabricating a base unit, the mold is designed with nine injection inlets, allowing the 8 voxels and the connecting beams to be injected individually. However, extending this programmable mechanical property to a larger scale requires a strategy to fill and orientate multiple voxels simultaneously. To address this challenge, a systematic method to achieve desired spatial magnetic configuration is established.

### 2.2.2 Multi-step fluidic control programming and 3D magnetic orientation

Developed from traditional molding methods, the multi-step fluidic control programming involves mold fabricating, fluid injecting, and demolding

procedures. Here, the mold for the multi-unit structure is initially created using a fused deposition modeling (FDM) 3D printer, employing butanediol vinyl alcohol co-polymer (BVOH) filament for its solubility in water.

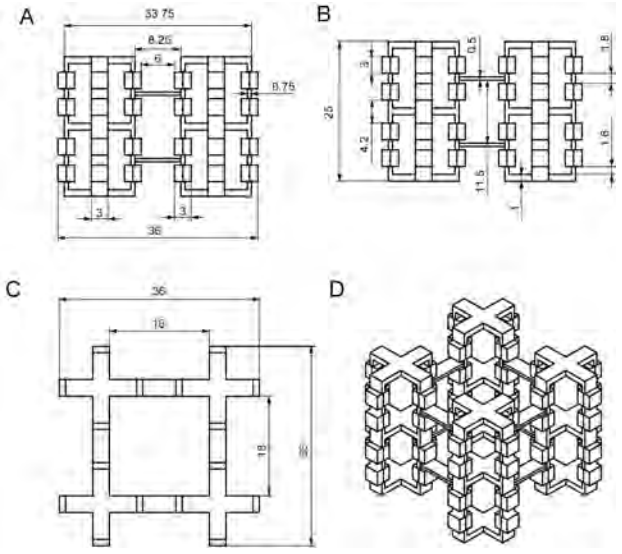


Figure 2.7: Geometrical design of the programmable metamaterial lattice. (A) Front view. (B) Side view. (C) Top view. (D) Isometric view. Unit, mm.

Once the 3D printing is completed, a mixture of magnetic particles and polysiloxane elastomer is injected into the mold with a precision pump in a series of iterative steps. After each injection iteration, the mold is positioned within an electromagnetic system, aligning the uncured composite along the predetermined axis. This approach can be extended to create MSMs with more voxels and magnetic configurations as designed in Figure 2.7. To facilitate this complex injection process in a 3D scenario, we designed a 3D injection channel with one inlet and four outlet nodes (Figure 2.8).

Here, this model is systematically rotated four times to assemble a comprehensive 3D fluidic programming channel model, as shown in Figure 2.9A. To visualize the capabilities of this fluidic control system, a transparent mold is prototyped using a stereolithography (SLA) printer. This mold is then filled with four colors of pigment to differentiate and highlight

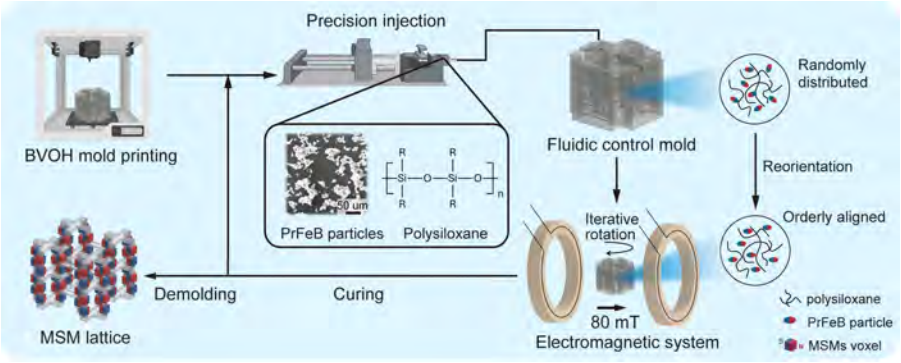


Figure 2.8: Structural fabrication and 3D fluidic control programming procedure of multi-unit MSM lattices. The magnetic particles are characterized with SEM image.

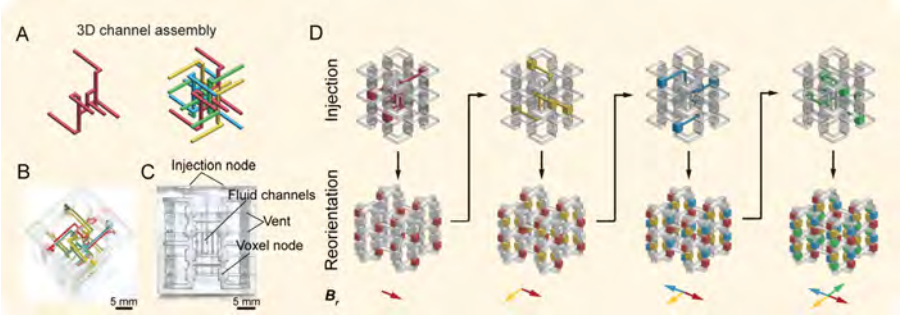


Figure 2.9: Fluidic control programming strategy for fabricating multi-unit MSM lattices. (A) Structure of fluid channels used for multi-directional magnetic programming. Each magnetization iteration is represented by one of the four colors (red, yellow, blue, and green). (B) Image of 3D printed transparent mold injected with four distinct colors. (C) Cross-section view image of 3D printed transparent mold. (D) Schematics on the 3D multi-step injection and orientation steps. The iterations are represented by four colors (red, yellow, blue, and green)

the flow paths and channel configurations, as shown in Figure 2.9B. Figure 2.9C shows a cross-sectional view of this transparent mold, revealing the intricate internal structure of the fluidic control system. To further illustrate the process of fabricating the 8-unit MSM lattice with four-directional magnetic configurations, Figure 2.9D shows the sequential injections and corresponding magnetic reorientations.

To evaluate the fluid properties of the composite, rheological tests are

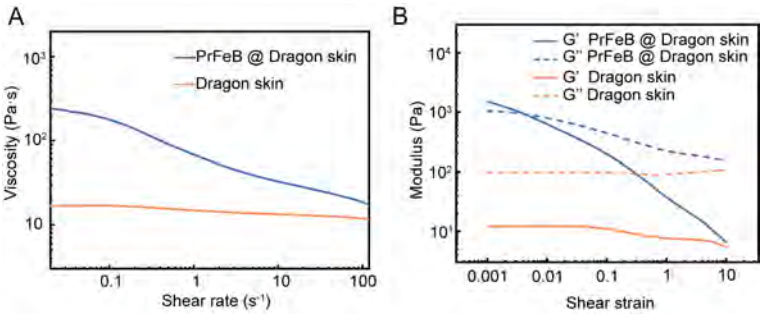


Figure 2.10: Rheological Properties of PrFeB @ Dragon Skin 30 and Base Matrix. (A) Flow curves of PrFeB @ Dragon Skin 30 and base matrix, illustrating shear-thinning behavior. (B) Modulus-shear strain curve of PrFeB @ Dragon Skin 30 and base matrix.

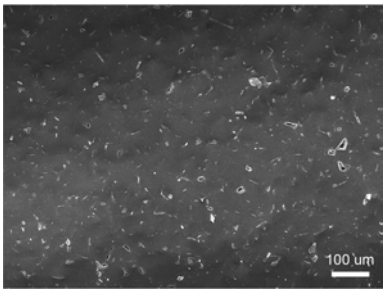


Figure 2.11: Scanning electron microscope image of the MSM composite.

performed as shown in Figure 2.10. The shear-thinning behavior of PrFeB and Dragon Skin 30 mixture facilitates smooth injection with low resistance, while its higher viscosity ensures stable particle distribution within the fluid matrix, crucial for consistent material properties and performance. The uniformity is further characterized with scanning electron microscope (SEM, Figure 2.11). Once the injection and magnetic alignment processes are completed, the mold undergoes a curing phase to solidify the composite. Then, the next iteration of injection, magnetization and curing is performed on a different section of the mold. After the full array of iterations is completed, the entire mold is submerged in a hot water bath, where it is designed to dissolve completely and can easily be demolded.

### 2.2.3 MSM lattice with switchable Poisson's ratio

The programmable mechanical properties of the lattice are characterized in an *in situ* mechanical test system as depicted in Figure 2.12. This setup includes a linear slide to apply the compressive load, force sensors, and electromagnetic coils to provide switchable magnetic fields. In this study, three different magnetic environments (OFF, Z+, and Z-) are selected to investigate the programmable mechanical behavior of the lattices. To describe the deflection mode, we model the segments as Euler-Bernoulli beams, and the elastic beams can be described with discontinuous buckling when the nonlinearity is sufficiently strong, where the value of postbuckling slope (S) indicates different buckling modes including slender beams, wide beams, and metabeams[69].

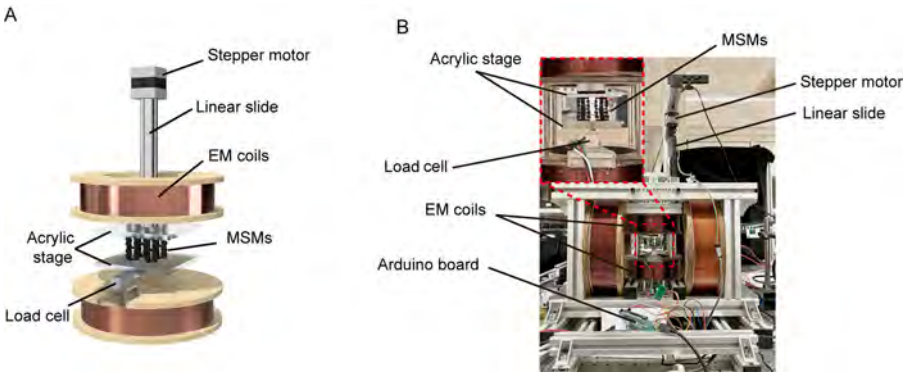


Figure 2.12: Scanning electron microscope image of the MSM composite.

In the uniaxial compression tests, three lateral deformation modes are observed. The process of the mechanical test is presented in Figure 2.13A, with the compressive strain increasing from 0% to 30%. Finite element analysis also suggests the same deformation modes in the experiments (Figure 2.12B).

The programmable mechanical properties are further evaluated in the load-displacement curves (Figure 2.14A) and strain-Poisson's ratio curves (Figure 2.14B). Upon removal of the magnetic field, the metamaterial lattice exhibits the instability behaviors corresponding to discontinuous buckling mode. This is evidenced in the load-displacement curve, wherein a negative slope is observed after the average critical load of 300 mN. And

Figure 2.13: Magnetic soft metamaterial lattice with switchable Poisson's ratio. Magnetic fields are applied in z-direction where the upward direction is defined as Z+, and the downward direction is defined as Z-. (A) Images of 8-unit metamaterial lattice samples compressed in different magnetic field conditions. The black area above the sample is the linear slide which applies the compressive load. (B) Finite element analysis of 8-unit MSM lattice samples compressed in different magnetic field conditions.

the Poisson's ratio stays near zero. The instabilities are practically eliminated when the magnetic field is activated, which can be identified from the unified deformation mode in each compression cycle and the standard deviations of the postbuckling load. Specifically, in the presence of a Z+

magnetic field, the metamaterial lattice adopts a convex curvature even before any load is applied. Consequently, upon loading, a positive Poisson's ratio ($\nu_{max}$ = 3.41) mode appears, indicating an expansion in the transverse direction relative to the applied axial strain. The critical load is 236 mN and the postbuckling slope turns positive with $S > 0$. Conversely, when subjected to a Z- magnetic field, the metamaterial lattice exhibits an inward curvature before loading. A negative Poisson's ratio mode ($\nu_{max}$ = -2.64) is observed, indicating a transverse contraction relative to the applied axial strain. The critical load is 256 mN and the postbuckling slope is positive with $S > 0$. In this mode, the slope undergoes a further increase when the compressive displacement exceeds 5.7 mm, which is caused by the contact of voxels.

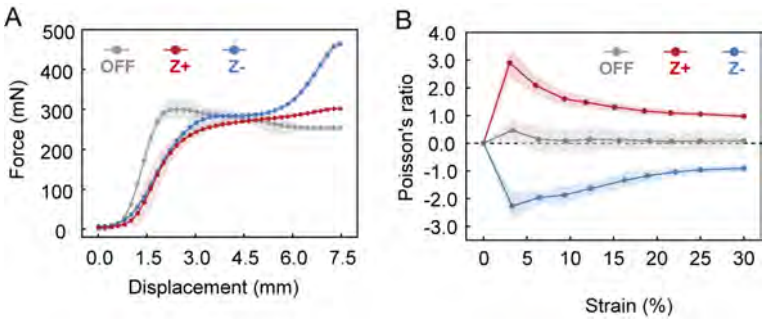


Figure 2.14: (A) Force-displacement curve of 8-unit MSM lattice samples compressed in different magnetic field conditions. Each curve is the mean value of 3 compression tests and the standard deviations are represented with shadows. (B) Poisson's ratio-strain curve of 8-unit MSM lattice samples compressed in different magnetic field conditions. Each curve is the mean value of 3 compression tests and the standard deviations are represented with shadows.

To evaluate the stability of MSMs for long-cycle compression, fatigue tests are performed under three different magnetic field modes. The results indicate that the MSM lattice exhibits stable mechanical behaviors across all tested modes (Figure 2.15A-C). Specifically, after 500 compression cycles, the MSM lattice retains 97%, 95%, and 94% of its maximum reactive force under the Z+, Z-, and no magnetic field modes, respectively.

Additionally, three different instability buckling modes are observed under identical conditions (Figure 2.16) showing the nonlinearity of the system.

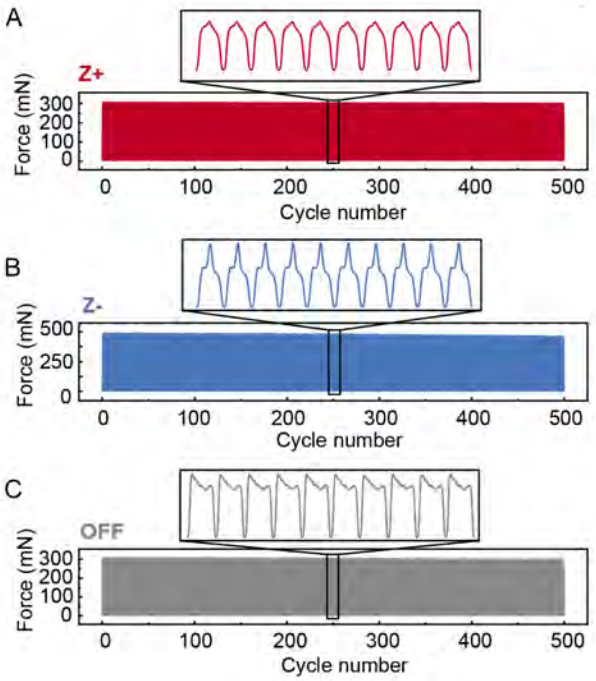


Figure 2.15: (A-C) Force-cycle number curves of MSM lattices in the fatigue test

Figure 2.16: Instability guided buckling modes of the metamaterial lattices compressed without the magnetic field.

### 2.2.4 MSM lattice with reconfigurable orthotropic behaviors

With the multi-step injection and orientation strategy, three-dimensional MSM structures with 64 voxels can be magnetized by four groups of orientations therefore sixteen theoretical permutations and eight mechani-

cal modes (after eliminating the duplication caused by symmetry) (Figure 2.17A). To demonstrate the capability of the 3D fluidic programming and reorientation for MSMs with various magnetization patterns, we fabricate MSM lattices with biaxial symmetric and anti-symmetric configurations (Figure 2.17B). Compared to the previously demonstrated metamaterial lattices, the magnetization mode is flipped between the x-z and y-z.



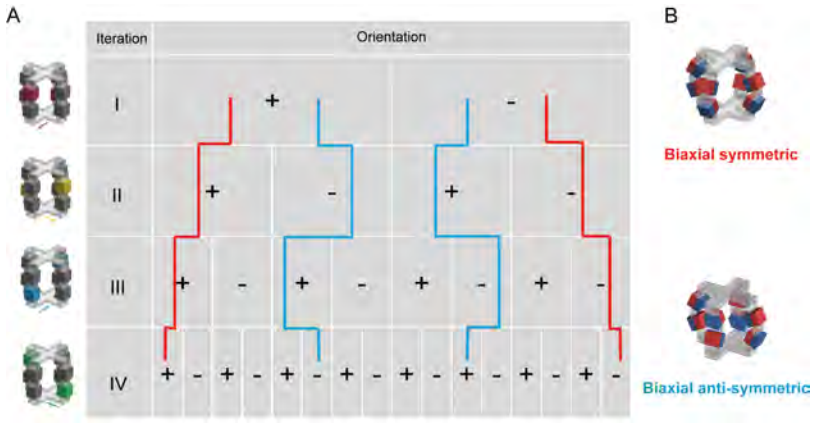


Figure 2.17: MSM lattice with reconfigurable orthotropic behaviors. Magnetic fields are applied in z-direction where along z-axis is defined as Z+ and the opposite direction along the z-axis is defined as Z-. (A) Permutations of magnetization patterns for MSMs, where "+" is the direction represented by the colored arrow. (B) Biaxial symmetric and biaxial anti-symmetric MSM base units.

Verified through both simulation and compression testing, the symmetric MSM lattice shows either outward or inward curvatures on all four sides when subjected to magnetic fields of 50 mT in Z+ and Z- scenarios (Figure 2.18A). In contrast, the biaxial anti-symmetric magnetic metamaterial lattice exhibits orthotropic deformation modes under the same compressional forces in magnetic fields of 50 mT in Z+ and Z- scenarios (Figure 2.18B). Unlike the symmetric lattices, the anti-symmetric configuration shows different bending behaviors on each side, which leads to non-uniform deformation. This behavior is clearly visible in the compressional test images, where the deformation modes differ significantly from the symmetric counterpart. However, when the magnetic field is OFF, the biaxial anti-symmetric MSM lattice exhibits a similar buckling behavior

to that of the symmetric metamaterial lattice, indicating that the primary differences arise due to the magnetization pattern under the influence of a magnetic field.

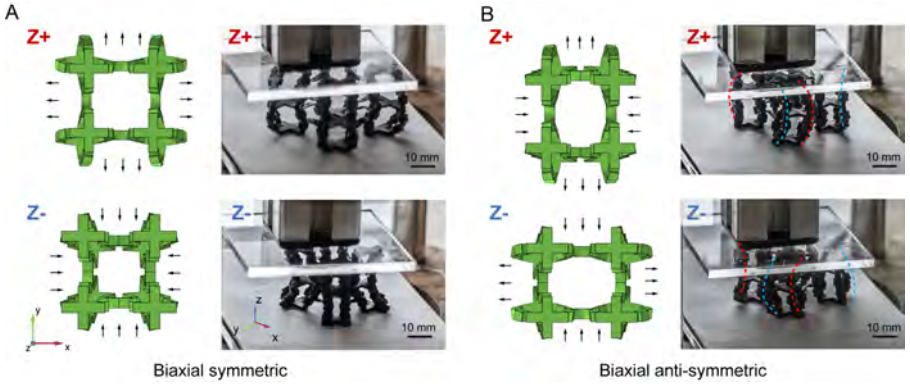


Figure 2.18: (A) Simulation and experimental images for the deformation modes of biaxially symmetric lattices compressed in the presence of Z- and Z+ magnetic fields. (B) Simulation and experimental images for the deformation modes of biaxially anti-symmetric lattices compressed in the presence of Z- and Z+ magnetic fields.

Specifically, when the magnetic field is turned on, the sample exhibits the almost the same force-displacement curves in both Z+ and Z- magnetic fields (Figure 2.19A). When the magnetic field direction is Z+, the sample shows an outward convexity in the y-z plane and an inward concavity in the x-z plane. When the magnetic field direction is Z-, the sample is concave in the y-z plane and convex in the x-z plane. Upon loading, an expansion in the y-z plane ($\nu_{max}$ = 3.29) and contraction in the x-z plane ($\nu_{max}$= -2.61) relative to the applied axial strain is observed (Figure 2.19B). Conversely, when subjected to a Z- magnetic field (Figure 2.19C), the MSM lattice exhibits a negative Poisson's ratio mode in y-z plane ($\nu_{max}$ = -2.76) and positive Poisson's ratio in x-z plane ($\nu_{max}$ = 3.44).

### 2.2.5 MSMs with programmable mechanical-based functions

The capability to generate multi-modal deformation allows us to achieve various functions with the metamaterial lattice, as shown in Figure 2.20. Our approach offers advantages for the development of soft robots that op-

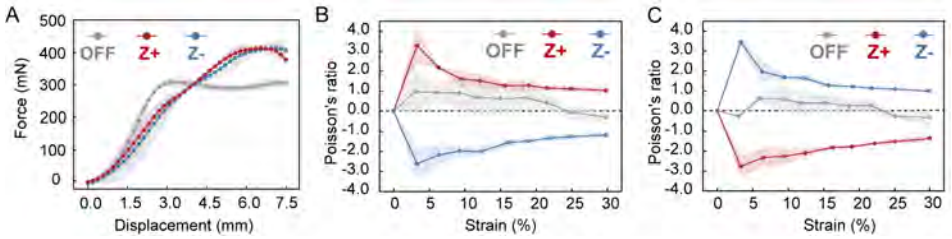


Figure 2.19: (A) Load-displacement curve of biaxial anti-symmetric magnetic metamaterial lattice. (B) Poisson's ratio-strain curve of orthotropic metamaterial lattice in the x-z plane. (C) Poisson's ratio-strain curve of orthotropic magnetic metamaterial lattice in y-z plane.

erate in confined spaces and require high compliance and precise actuation for miniaturization and safety. To demonstrate its instantaneous response and the advantages of wireless actuation using magnetic fields, we utilize one reconfigurable base unit as an in-tube soft robot. The base unit is inserted into a vertically placed glass tube with an inner diameter of 14 mm. Using a magnetic field, the base unit can be expanded or contracted in the transverse direction, thereby manipulating the frictional forces with the wall, and enabling it to be anchored or released as desired.

As shown in Figure 2.20A, a cylindrical mass is placed on the top of the base unit. By switching the magnetic field to Z-, the sample contracts, reducing friction, and facilitating downward movement under the effect of gravity. Then, by switching the magnetic field to Z+, it expands and instantaneously stops the downward movement of the load. The weight of one base unit is 2.14 $\pm$ 0.1 g and the carrying capability is evaluated with loads of 1.5 g, 2.5 g, 3.5 g, and 5.0 g, respectively (2.20B). In each case, the loads and the robot are released from the top, stopped in the middle, and then released again to fall to the bottom of the tube. Due to the instantaneous response to the magnetic field, a sudden stop can be achieved within a 0.01 s duration while the reconfigurable base unit drops through the tube.

We further demonstrate the capability of combining electronic components and circuitry with our multi-unit structure. An electrical circuit is developed with three modes of operation: switching on red LEDs, switching on green LEDs or all LEDs turned off. A metamaterial lattice sample with a magnetization pattern depicted in Figure 2.9 is placed in the middle

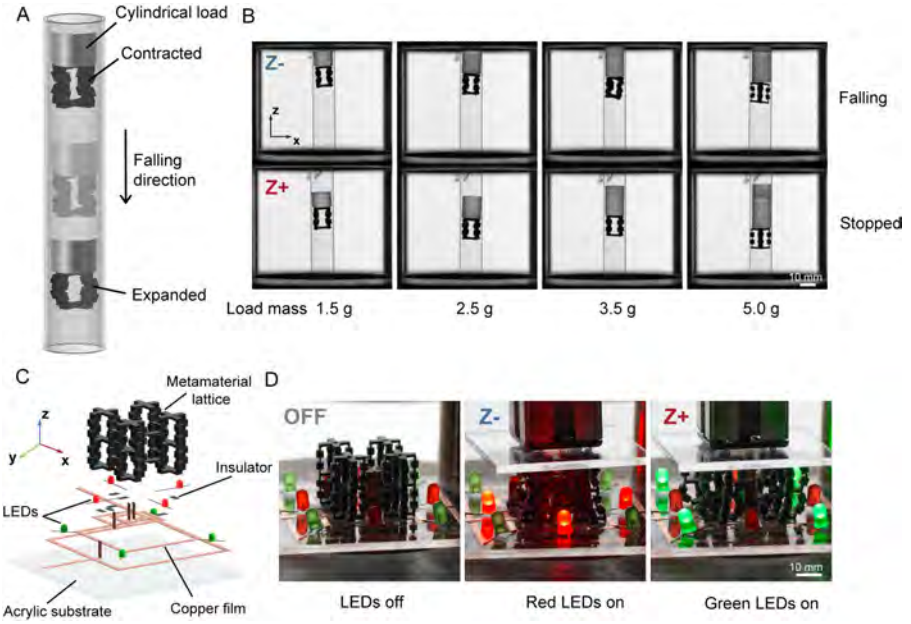


Figure 2.20: Functional demonstrations of the MSMs. Magnetic fields are applied in z-direction where the upward direction is defined as Z+, and the downward direction is defined as Z-. (A) Schematic of the programmable base unit used as a programmable load carrier. (B) Images of the base unit stopping and releasing different masses by contracting and expanding in the presence of the magnetic field. (C) Schematic design of metamaterial lattice as a reconfigurable soft electronic device. (D) Metamaterial lattice-based soft electronic devices exhibit different electronic functions depending on the direction of applied magnetic fields of 50 mT.

of the circuit, as shown in Figure 2.20C. The MSMs are then evaluated by functioning as a double-throw switch that can be activated by the magnetic field-guided buckling in the designed circuit. When the material contracts, the red LEDs are activated, and the expansion of the material triggers the green LEDs (Figure 2.20D). Similar results are also observed when pressing the MSMs above a 60 x 5 mm NdFeB disk magnet. This result showcases that the magnetic metamaterial lattice can form parts of soft electronics and offer a high degree of programmability.

## 2.3 Conclusions

In conclusion, we develop a strategy to realize multimodal deformation in 3D magnetic soft mechanical metamaterial structures through a voxelated fabrication methodology. Our approach achieves the magnetization of all voxels in a weak magnetic field through a multi-step injection strategy. The magnetic soft composite shows sensitive responses to the external magnetic field, resulting in a rapid switching between different mechanical behaviors such as positive/negative Poisson's ratio, and orthotropic deformation. The reconfigurable MSMs also exhibit the ability to manipulate frictional forces in a glass tube. A soft electronic device with programmable functions is achieved, demonstrating the capabilities of the MSMs in electromagnetic applications. This work represents a step forward in the development of magnetic soft materials and holds great potential for future applications that require responsive and reconfigurable metamaterials.

To broaden the application scope, future investigations should consider integrating additional functionalities into MSMs, such as electrical conductivity and thermal responsiveness. Such advancements could transform the practical use of MSMs across diverse fields, for example in wearable technologies or other biomedical devices. Miniaturizing the MSMs to millimeters or even micrometers with more integrated units will also be important for future magnetic soft metamaterials with advanced functions.

## 2.4 Experimental procedures

### 2.4.1 Preparation of magnetic composite

Before mixing, all the PrFeB particles (MQFPTM-16-7) were magnetized in an impulse magnetizer (IM-10-30, ASC SCIENTIFIC) at a 2 T magnetic field. The magnetic composite was prepared by blending PrFeB particles and Dragon skin 30 (Smooth-on, Inc) in a ratio of 33 wt. %. After thoroughly mixing at 2800 r.p.m. for 2 minutes, the blend was degassed inside a vacuum chamber for 5 minutes. The degassed mixture was then transferred into a 12 mL syringe and ready for injection.

### 2.4.2 Multi-step injection and weak field orientation

The multi-step injection process involved injecting uncured magnetic composites into one of the four main ports using a precision injection pump (NE-1000, ProSense B.V.) at a rate of 0.50 mL/s. After injection for each magnetization direction, the mold was transferred to the electromagnetic coil system and positioned for specific magnetization orientations. Then, an 80 mT magnetic field was applied for 5 seconds to orientate the particles. Subsequently, the mold was moved to a heating platform and maintained at a temperature of 80 °C for 15 minutes to ensure full curing of the magnetic composites. This injection procedure was repeated for all magnetization groups successively. Finally, the composite was also injected into the connecting channels and cured without orientation in the electromagnetic field.



### 2.4.3 *In situ* mechanical tests

An *in situ* mechanical test system as depicted in Figure 2.12 was established including a stepper motor (NEMA-17, Adafruit Industries), a load cell sensor (YZC-131-1kg, Guangzhou Electrical Measuring Instruments Factory), and a microcontroller (Arduino Mega 2560 Rev3). During the tests, vertical magnetic fields (Z direction) were applied. In all conditions, the stepper motor moved at the speed of 1 mm/s, cycling between compressing distances of 6.5 mm for the base units and 7.5 mm for the multi-unit metamaterial lattice. To measure the Poisson's ratio, a DSLM camera (ICLE-7C, Sony) was placed directly in front of the sample taking 120 fps video of the tests.

Fatigue tests are also performed with the in situ mechanical test setup. Samples of MSM lattice are subjected to 500 compression cycles in the setup depicted in Figure 2.12. The loading and unloading rates are maintained at 1 mm/s, with a total displacement of 7.5 mm for each cycle.

### 2.4.4 Finite element analysis

For the designs presented in Figure 2.6 and Figure 2.13, deformations in the presence of external magnetic fields were simulated using the Solid Mechanics and Magnetic Fields, No Currents (mfnc) module in COMSOL Multiphysics 5.4. The material is defined as linear elastic according to the

mechanical experiments (2.6A), with a Young's modulus = 485 kPa. The simulations applied a uniform external magnetic field = 50 mT. For multi-unit lattice structures, a magnetic torque was modeled using surface loads with equal magnitude and opposite directions on each voxel.

Where is the area load [N/m$^2$], is the magnetic moment [A/m$^2$]. is the flux density of the magnetic field applied [T], is the angle between the magnetization direction ($\boldsymbol{M}$) of the voxel and the direction of the externally applied magnetic field ($\boldsymbol{B}$). is the area that the load acts on [m$^2$], and is the distance between two opposite loads [m]. is the magnetization of the composite materials, which is measured at 8.7 kA/m with a Hall-effect based setup. is the volume of the voxel [m$^3$]

### 2.4.5 Material mechanical characterization

The mechanical characterization is conducted using a texture analyzer (CT3, AMETEK GmbH B.U. Brookfield). Standardized testing samples made of Dragon skin 30 and the magnetic composites are subjected to axis tensile tests as per ASTM standard tests. The loading speed for the tests is set to 1 mm/s, and the testing range is set to 200% of strain. Nominal stress-strain curves are provided in Figure 2.6A.

# 3

# Multi-layer screen-printing of magnetic soft robots with integrated materials and functions



***Note:*** *The following chapter is adapted from the article "Multi-layer screen-printing of magnetic soft robots with integrated materials and functions" by* ***Z. Wang****, S. Misra, and V.K.Venkiteswaran , published in "Cell Reports Physical Science", volume 6, issue no. 6, June 2025.*

Soft robots that respond to externally applied magnetic fields are emerging in various applications with integrated functional materials and patterned magnetization profiles. Current fabrication techniques, such as casting and 3D printing, typically involve prolonged processing cycles, limited throughput, restricted material choices, and substantial challenges in achieving precise, part-specific magnetic programming. Here, we establish a multi-layer screen-printing strategy for directly fabricating the main body of magnetic soft robots with patterned magnetization profiles. Leveraging the inherent advantages of screen-printing, materials such as paper and fabric, rigid substrates including glass and wood can be actuated in magnetic fields to exhibit programmed deformation. By incorporating multiple types of ink and substrate materials, magnetic soft grippers for vascular surgeries, wireless robots with embedded circuitry, and bio-inspired butterfly-like robots are demonstrated. This work improves the functionality and scalability of fabricating magnetic soft robots with expanded potential in deployment across biomedical engineering, robot research, and artistic disciplines.

## 3.1 Introduction

The emergence of magnetic soft robots (MSRs) has been driven by the development of materials that respond to magnetic fields, enabling programmable magnetization profiles and wireless actuation modes[70]–[76]. Their untethered and adaptive shape morphing ability enables them to navigate complex environments and perform precise manipulation tasks, providing considerable promise in applications such as health monitoring[77]–[79], human-machine interaction[80], [81], and minimally invasive surgery[53], [82]–[84]. Despite substantial advancements in fabricating MSRs achieved by recent research, integration of various materials and functions with arbitrary pattern and magnetization profiles still remains challenging. A typical approach involves attaching small permanent magnets to the soft robots for magnetic manipulation and localization[19], [40], [85], [86]. Alternatively, molding and casting have been the most common fabrication methods utilized for magnetic soft robotics with relatively simple geometry[20], [43], [87]. For more complex configurations, a third strategy involves curing composites embedded with magnetizable particles, which are magnetized to saturation in a temporarily deformed state, followed by the manual assembly of components[13], [42], [54], [55]. With potential applications in biomedical devices and wearable technologies requiring more consistent and precise fabrication techniques[41], the limitations of these fabrication methods, particularly in assembly and magnetization processes, have become increasingly evident.

Recognizing these challenges, subsequent advancements in magnetic programming have led to the emergence of more automated methods for fabricating smaller and more delicate structures. 3D printing techniques have been developed to create complex 3D architectures that integrate magnetically responsive materials with other functional components[**?**], [47], [60], [88], [89]. However, 3D printing like direct ink writing limits magnetization profiles to a single direction or along the printed fibers, depending on the printer's magnetic system, and photolithography imposes strict requirements on both the materials and the environmental conditions. Recently, heat-assisted reprogramming methods based on phase-change materials with relatively low melting temperature such as polyethylene glycol (PEG)[67] and polycaprolactone (PCL)[90], or heating the magnetic component beyond the Curie temperature and reorienting upon cooling[66],

have been presented for fabricating MSRs . This strategy allows the reorientation of embedded magnetic particles under an external magnetic field above the critical temperature followed by immobilizing the particles through cooling, but it still limits the selection of material systems and the integration of multiple functionalities. All aforementioned processes require advanced laboratory equipment and materials with specialized physical properties, which significantly elevates the cost for industries to update their production lines. To address the rapidly evolving demands and fulfill the potential of MSRs, it is crucial to develop a simplified and widely applicable fabrication strategy that seamlessly integrates customized magnetization profiles with multifunctional materials.



Screen-printing, a traditional technique with a history spanning over a thousand years, has been one of the most mature and widely adopted methods in various industries, ranging from garment to integrated circuits[91], [92]. Through rapid and well-controlled ink transfer, this scheme provides wide pattern flexibility, material adaptability, and high production scalability. At present, screen-printing is prevalent in fabricating soft devices, covering a broad spectrum of applications such as biosensors[93]–[95], solar cells[96]–[99], and energy storage systems[100]–[103]. For example, sensors use screen-printed soft electrodes to integrate different sensing modules and simultaneously monitor the key metrics in medical diagnostics[104], [105]. Solar cells are developed by screen-printing organic semiconductor thin films that serve as essential components in photovoltaic devices, offering high electrical conductivity and transparency to improve the light-to-electricity conversion efficiency[106]. Screen-printing also simplifies the fabrication of energy storage systems. High-performance electrodes and electrolytes are printed to assemble flexible batteries and supercapacitors[107], [108]. The screen-printing approach warrants further investigation due to the comparable rheological properties of magnetic elastomers and traditional viscoelastic inks commonly employed in screen-printing processes. However, research on screen-printing in the direct manufacture of the main body of soft robotics, especially magnetic soft robotics, is limited. We assume that the main resistance comes from the introduction of magnetic programming to printed patterns. In this study, we embrace the screen-printing and magnetic reorientation technique to fabricate and program the main body of magnetic soft robotics, enabling part-specific programming of magnetic polarization. This capability marks a critical step toward scal-

able, low-cost manufacturing without compromising functional complexity.

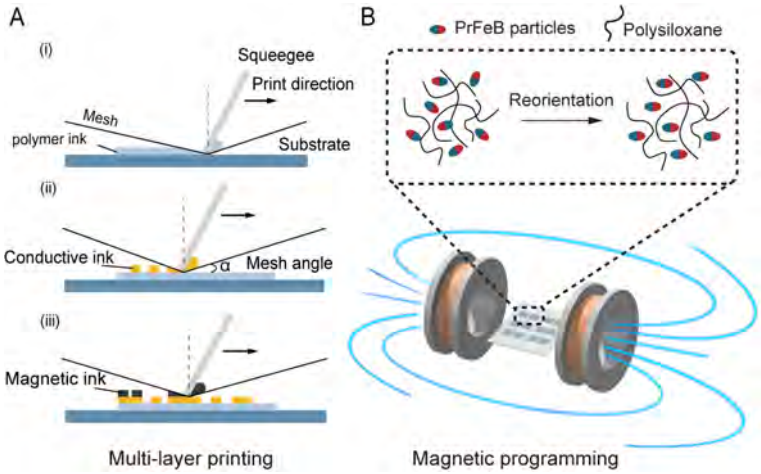


Figure 3.1: Screen-printing strategy for magnetic soft robotics: process, magnetic customization, material characterization, and applications. (A) Schematic illustration of multi-layer screen-printing process (in roman numeral order). (B) Magnetic reorientation aligns the magnetic particles in a uniform magnetic field before the polymer matrix curing.

Here, a layer-by-layer screen-printing strategy for rapid fabrication of MSRs with customizable magnetization profiles and multiple materials is established (Figure 3.1A,B). By precisely depositing magnetic ink on elastomer films and other functional substrates, and iteratively programming the orientation of magnetic particles, we create soft robots with responsive shape-morphing ability and other functions. We also present screen-printing of MSRs such as mini-grippers that can navigate in a vascular model and carry small objects wirelessly; programmable surfaces with 3D deformation; multi-layer soft electronic devices with active deformation modes; and a bio-inspired butterfly robot with fluorescent coloration that responds to ultraviolet (UV) stimuli and flaps in response to magnetic field. Our fabrication scheme provides a platform for producing soft robotic systems, with innovative features such as enhanced versatility, scalability, and functionality, offering prospects for precise, facile, and high-throughput production of MSRs.

## 3.2 Results

### 3.2.1 Multi-layer screen-printing and magnetic programming

The screen-printing process involves the precise transfer of ink from a stenciled mesh onto the target substrate through three stages: mesh flooding, squeegee action, and separation[109]. In this study, we implement a multi-layer printing technique whereby each subsequent layer is printed with the previous layer as the substrate. A three-layer printing process is shown in 3.1A as an example of integrating multiple materials.



Initially, a base layer is printed using polysiloxane ink (Figure 3.1A, i), followed by conductive (or other functional materials) (Figure 3.1A, ii) and magnetic layers (Figure 3.1A, iii), each formed by carefully controlling the squeegee angle and direction to ensure uniformity. The stenciled mesh is created by attaching laser-scanned, self-adhesive paper to a pre-stretched nylon mesh, which is then secured within a custom 3D-printed frame. Prints with different speeds and mesh sizes are analyzed to further characterize the printing process (Figure 3.2). The results indicate that using a 100-mesh screen combined with printing speeds in the range of 10-30 mm/s yields optimal outcomes, effectively minimizing ink spillage and magnetic particle segregation.

The preparation of the magnetic ink involves blending PrFeB magnetic particles with a polysiloxane elastomer matrix to facilitate magnetic responsiveness and rheological adjustments (Figure 3.3A). Figure 3.3B shows the seamless integration of three types of materials and characterized through a scanning electron microscopy (SEM) image. To optimize the printing quality and magnetic responses, we explore the rheological behavior of non-magnetic ink and magnetic ink through a series of rheology studies (Figure 3.4A). Steady shearing and oscillatory tests indicate that the mass load and initial magnetization condition of PrFeB particles play a critical role in influencing the magnetic ink's viscosity and viscoelasticity properties. Typically, an increased PrFeB particle ratio enhances both viscosity and viscoelasticity properties, while the magnetization of PrFeB particles also shows a pronounced effect on the overall rheological behavior.

The ink with magnetized particles shows a high shear-thinning behav-

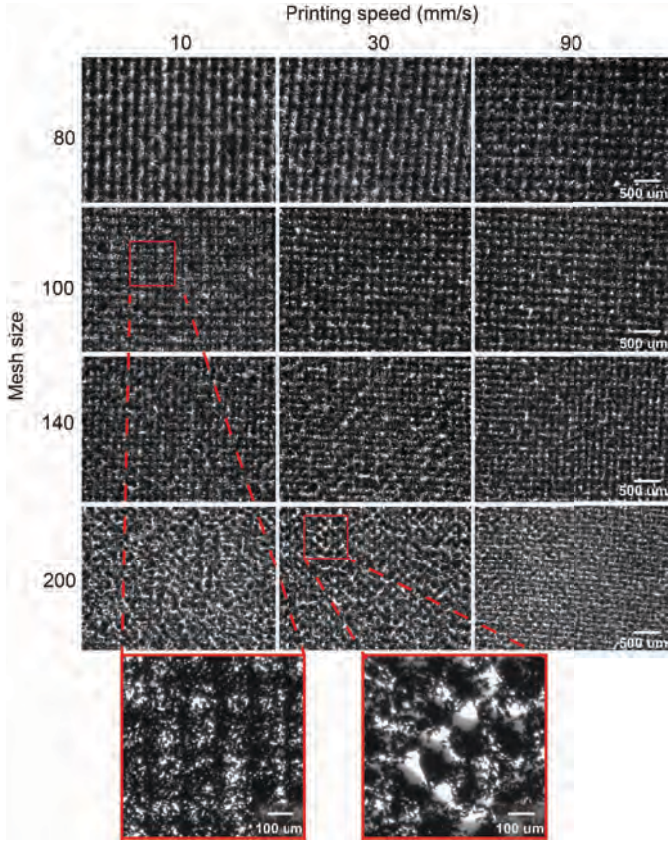


Figure 3.2: Microscope images of screen-printed magnetic soft material films. The films were prepared using mesh sizes of 80 (177 $\mu$m), 100 (149 $\mu$m), 140 (105 $\mu$m), and 200 (74 $\mu$m), with printing speeds ranging from 10 to 90 mm/s.

ior, with a reduction in viscosity as the shear rate increases (Figure 3.4A, i). The elastic component (storage modulus, *G'*), is higher than the viscous component (loss modulus, *G"*) under a relatively low shear strain, where the shear strain of the turning point increases with the mass load of PrFeB particles (Figure 3.4A, ii). This allows the ink to remain stable before and after squeezing but smoothly flow through the mesh. However, an excessively high particle ratio can compromise printing quality due to increased phase inhomogeneity. A mass ratio of 1:1 shows relatively uniform and stable features for both good printing quality and magnetic responses.

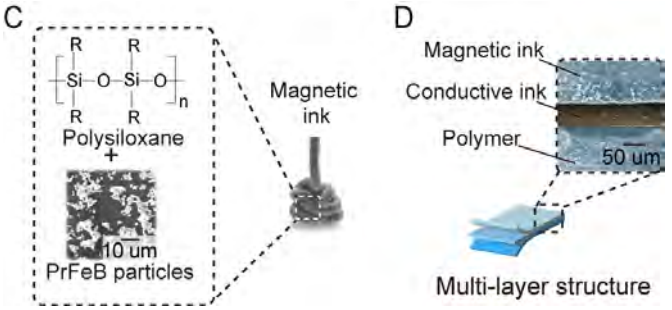


Figure 3.3: (A) Image of magnetic ink with explanatory diagram of the polymer structure and scanning electro-microscopy (SEM) image of magnetic particles. (B) Schematic and SEM images of a screen-printed multi-layer sample with the sandwich structure that includes magnetic layer, conductive layer, and polymer layer, respectively.

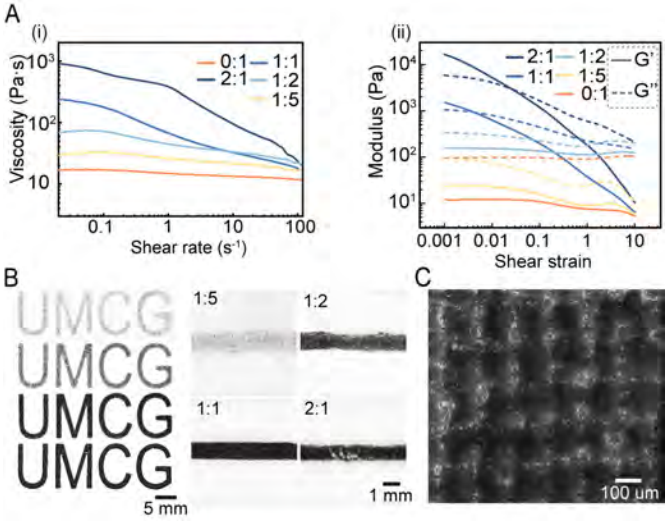


Figure 3.4: (A) Rheological properties of magnetic ink with different mass ratio of magnetic particles and filler magnetization conditions. (B) Printing quality test of magnetic ink with varying mass ratio of particles. Left: printed "UMCG" letters with increasing mass ratio (1:5 to 2:1). Right: magnified views of printed layers showing the impact of mass ratio on layer thickness and uniformity. (C) SEM image for characterizing the surface morphology and particle distribution on the concentration of 1:1 sample.

Figure 3.4B illustrates the print quality by printing the letters "UMCG", demonstrating the clarity and resolution of the printed pattern. When inks with different mass ratio of magnetic particles were used, the results showed that a low mass ratio led to blurred outlines of the printed pattern, while a high mass ratio caused particle aggregation, clogging the mesh, and resulting in surface defects. The 1:1 mass ratio exhibited the most uniform print quality, with consistent patterning and minimal defects. We use SEM to further characterize the surface of the 1:1 mass ratio sample (Figure 3.4C). The SEM image reveals a uniform distribution of magnetic particles across the printed surface, which is crucial for confirming the precision and consistency of the screen-printing process.



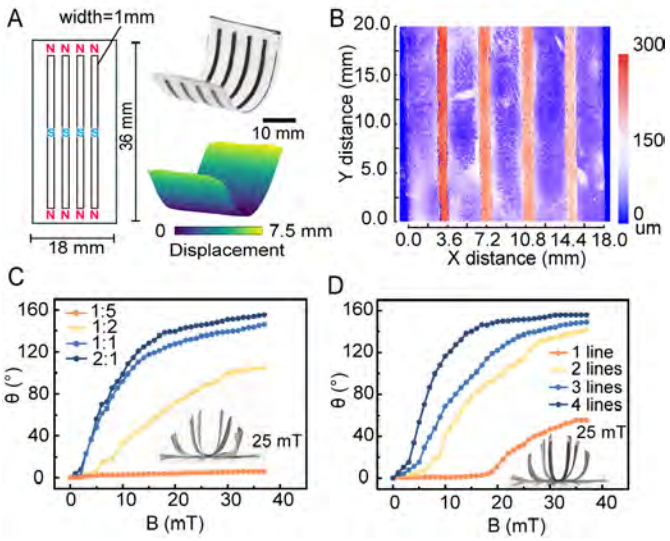


Figure 3.5: (A) Design and demonstration and finite element analysis (FEA) simulation of a two-layer prototype bending in the presence of a uniform magnetic field. (B) Surface morphology test for thickness distribution of a two-layer prototype. (C) Results of actuation test for two-layer prototypes with 1 4 lines in the magnetic layer. (D) Results of actuation test for two-layer prototypes with 1:5 2:1 mass ratio.

To evaluate the print quality and magnetic response, we specifically fabricated a two-layer prototype, which is designed to fold symmetrically in a uniform magnetic field (Figure 3.5A). The surface morphology of the pro-

totype is examined using a laser scanning morphological system, providing high-resolution topographic details (Figure 3.5B)., We then fabricate two-layer prototypes with different numbers of printed lines and subject them to a uniform magnetic field for further evaluating the responsive performance of screen-printed MSRs. As the flux density increases from 0 to 38 mT, the magnetic responsiveness of these devices is quantitatively assessed by measuring $\theta$, the supplementary angle between the two folding edges. The variations in response to the applied magnetic field are recorded and displayed in Figure 3.5C, offering a detailed comparative analysis of the bending behavior as a function of the number of printed lines. Moreover, another set of prototype samples, each with four printed lines but differing in the mass ratio of magnetic particles of the ink are also evaluated. The results in Figure 3.5D present the effects of the variations in magnetic ink formulation on magnetic responsiveness and mechanical bending properties.



These experiments establish a robust framework for evaluating and enhancing the printing quality and functional performance of screen-printed MSRs. The detailed analysis of magnetic ink, surface morphology, and magnetic response tests allows us to modify the screen-printing techniques and ink formulations. This, in turn, advances our capability to fabricate MSRs with more realistic functions such magnetic soft grippers, soft robots with onboard electronic circuits and attached LEDs, and bio-inspired butterfly robots with fluorescent coloration (Figure 3.6).

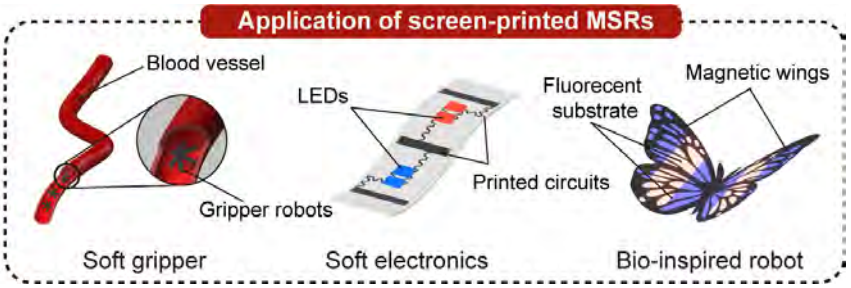


Figure 3.6: Schematic illustration for the potential applications of screen-printed magnetic soft robots (MSRs).

### 3.2.2 Screen-printed MSRs with diverse patterns and substrate materials

Currently, soft robots require specialized soft materials (e.g., elastomers, hydrogels) as the main structures. To explore the versatility of the screen-printing technique for magnetic soft robotics on a wide range of surfaces, we employ a series of materials as substrates and perform magnetic actuation on each individual specimen (Figure 3.7A). The selected substrates include natural materials such as wood and cotton fabric, which are assessed for their potential in integrating robotic behaviors with construction materials and wearable technologies; common materials including paper and glass, emphasizing the development of magnetically responsive robots aimed at sustainability and cost-efficiency; and specialized substrates such as indium tin oxide (ITO) coated films, which are particularly explored for their applications in advanced electronic devices such as perovskite solar cells. Here, we deploy a four-step printing and magnetizing procedure, fabricating two-layer samples for the folding behavior (Figure 3.7B). After each printing sequence of magnetic ink, the magnetic layer is programmed via magnetic reorientation or impulse magnetizing. Further tensile tests are conducted to characterize the adhesion of printed magnetic soft materials to various substrates. The results shows the adhesion strength is sufficient to maintain interface integrity while differences in adhesion still influence the tensile performances of the printed structures (Figure 3.8).

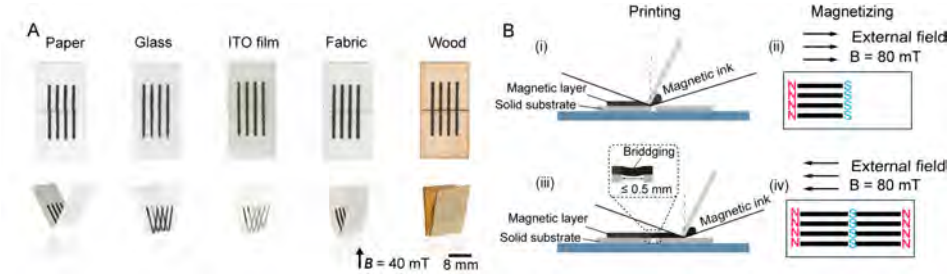


Figure 3.7: Adaptability of screen-printing magnetic soft robotics onto various substrates. (A) Screen-printed foldable samples with different substrate materials. Each sample shows a folding deformation under a uniform magnetic field of 40 mT. (B) Schematic diagram of screen-printing and reorientation steps (in roman numeral order).

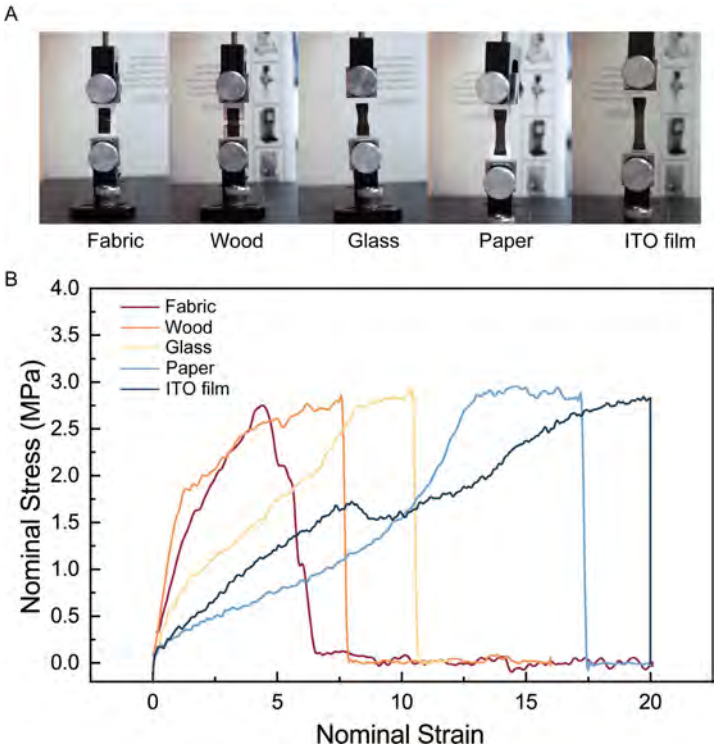


Figure 3.8: Tensile test results for screen-printed magnetic soft material films on various substrates (fabric, wood, glass, paper, and ITO film). (A) Images of samples at their maximum strain. (B) Nominal stress-strain curves illustrating differences in deformation behaviors and loading slopes caused by partial separation between the printed material and substrates, suggesting that substrate adhesion significantly influences mechanical performance.

To validate the potential of our screen-printing method on diverse surfaces, we present a conceptual demonstration highlighting the application of MSRs as foldable solar panels for spacecraft (Figure 3.9A). Here, a pair of foldable ITO films with screen-printed magnetic actuators is integrated into a satellite model, thereby exhibiting the folding and expanding mechanisms of the MSRs within a space technology context. Figure 3.9B presents a wireless pH sensing device fabricated by screen-printing a magnetic actuator between two pH test papers. This device enables wireless testing in environments where manual handling of pH samples is impractical, such as

in automated lab-on-a-chip platforms. Screen-printing also substantially reduces the technical and practical barriers to patterning MSRs.

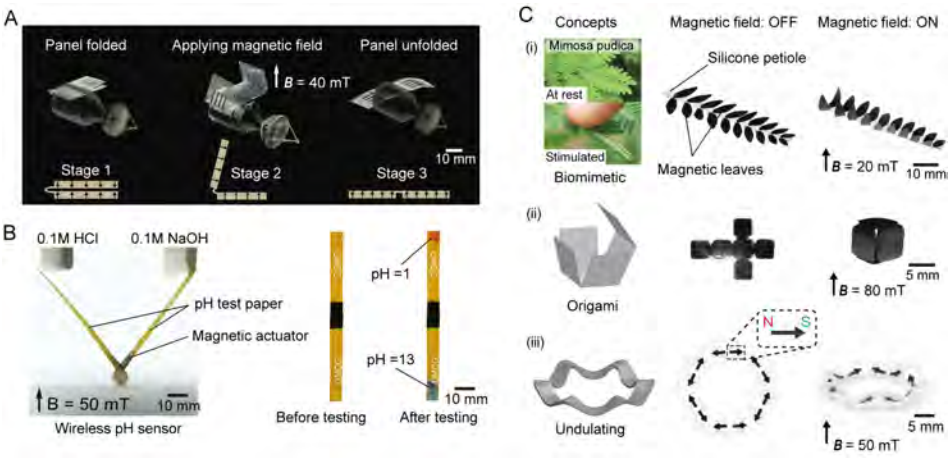


Figure 3.9: (A) Demonstration of using ITO films as substrate materials for screen-printed magnetically foldable solar panels in space engineering. (B) Demonstration of wireless pH sensor device that simultaneously tests the pH value of two samples by magnetically folding pH test papers, where a single layer of magnetic soft material is printed as the hinge. (C) Demonstration of three concepts with 3D shape-morphing structures: i) Biomimetic design of stimuli-responsive mimosa leaves, which can fold under a uniform magnetic field; ii) Origami-inspired design of a foldable sheet that deforms into a cube in the presence of a magnetic field; iii) An undulating ring structure with eight pair of arrow-shaped actuators, where each arrow is magnetized in the direction indicated by the pattern.

To demonstrate the versatility enabled by screen-printing, we design and present several magnetic soft robot concepts with three-dimensional shape-morphing structures (Figure 3.9C). These include bio-inspired stimuli-responsive mimosa that can fold the leaves under a uniform magnetic field of 20 mT, mimicking the natural closing motion of *Mimosa pudica* in response to external stimuli. Additionally, we show an origami-inspired soft robot consisting of a flexible sheet that deforms into a cube actuated via a magnetic field generated by a permanent magnet, demonstrating the potential for complex shape transformations and the creation of reconfigurable structures through magnetic actuation facilitated by screen-printing. Furthermore, we introduce an undulating ring structure with eight pairs of

arrow-shaped actuators, where each arrow is magnetized in the direction indicated by the printed pattern, highlighting the ability to program complex deformation modes into MSRs. These demonstrations indicate that our screen-printing approach can endow MSRs with a diverse range of patterns and deformation modes for future applications.

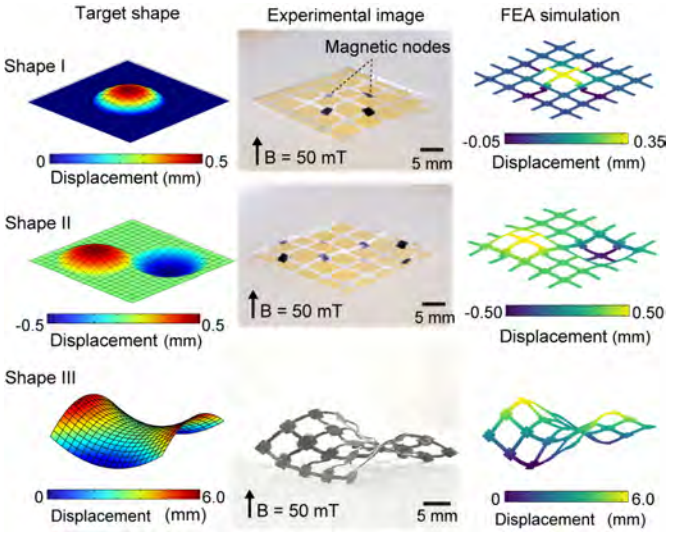


Figure 3.10: Magnetic programmable surfaces with precise shape-morphing ability.

The development of dynamically shape-morphing soft surfaces that can perform precise and real-time reshaping behavior driven by magnetic fields is pivotal in soft robotics[110]. In Figure 3.10, we demonstrate the fabrication of screen-printed magnetic soft surfaces with programmable shape-morphing capabilities. The process begins with printing a layer of non-magnetized polysiloxane grid, which serves as the substrate. Subsequent layers involve depositing magnetic ink at specifically designed nodes, which are then magnetized to achieve programmed rotational movements (Figure 3.11). By strategically arranging these magnetic nodes, we create three distinct magnetic programmable surfaces that exhibit different shape-morphing scenarios: single polar (shape I), dual polar (shape II), and saddle-shaped surfaces (shape III). Screen-printing of programmable surfaces enables autonomous systems to have adaptive shape morphing, thereby expanding the potential applications of soft robotics in fields re-

quiring dynamic surface transformations.

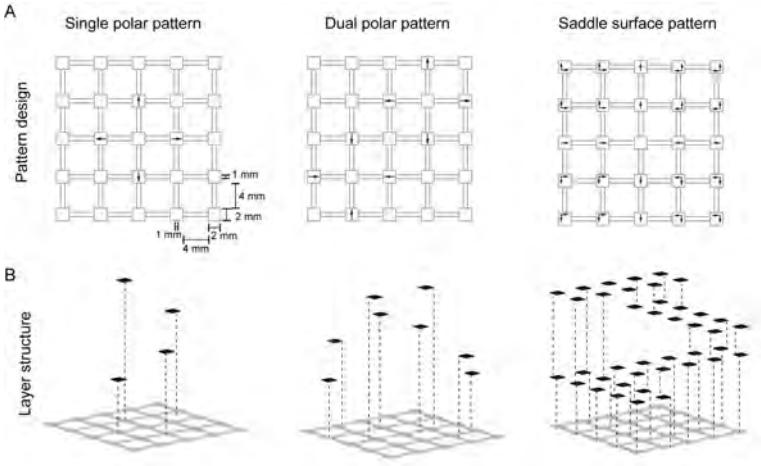


Figure 3.11: Designed geometries and magnetic profiles of screen-printed magnetic programmable surfaces. (A) Geometrical designs and corresponding magnetic configurations for different programmable surface patterns, including single polar, dual polar, and saddle surface patterns. (B) Multi-layer printing and magnetization strategy used to fabricate the structures.

### 3.2.3 Screen-printing of magnetic soft gripper robots

Soft gripper robots have garnered widespread interest due to their unique combination of flexibility, adaptability, and precision. These robots are particularly advantageous in biomedical applications, where their soft, compliant nature allows for delicate interactions with biological tissues[111]. The integration of magnetic materials facilitates remote actuation, enabling maneuvers without invasive intervention. Current advancements have primarily achieved progress in materials and controls, where scalable methods for fabricating gripper robots have received comparatively less attention[112].

In this study, we employed the screen-printing technique to realize fast prototyping and functional integration potential of magnetic soft gripper robots (MSGRs) for biomedical applications. Figure 3.12A and Figure 3.12B shows the geometry and magnetization profile of the grippers, where the six beams are radially magnetized. The gripper robots have two deformation modes: folding and expansion, as illustrated and simulated

in Figure 3.12C. To fabricate the MSGRs, magnetic ink is printed on an acrylic substrate through a stenciled mold, which allows for fabricating one hundred grippers within a 40 mm by 40 mm area by a single squeegeeing (Figure 3.12D).

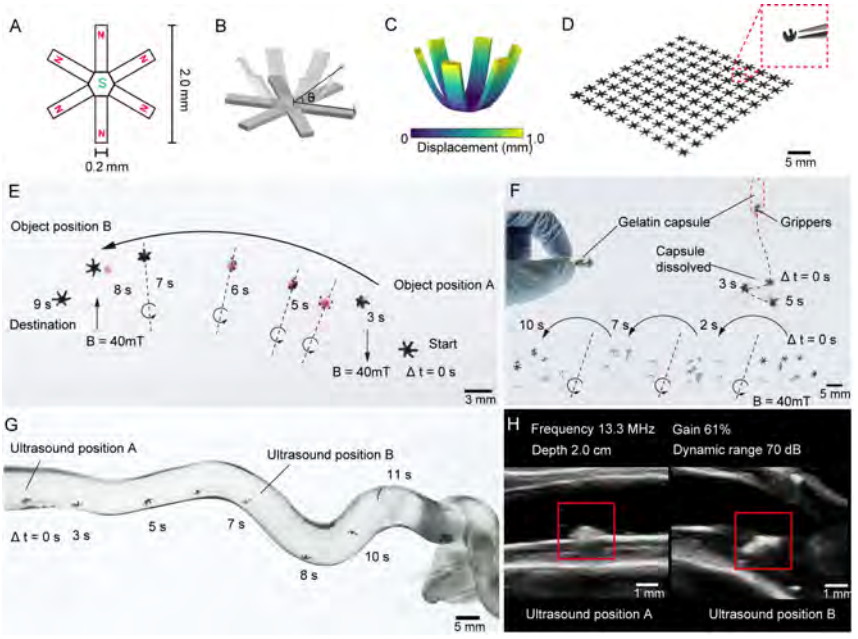


Figure 3.12: Screen-printed magnetic soft gripper robots. (A) Geometric design and magnetic configuration of the gripper robots. (B) Schematic illustration of magnetic soft gripper being actuated in the presence of a magnetic field. (C) Finite element analysis (FEA) simulation for the magnetic gripper robot placed in a uniform magnetic field of 60 mT. (D) Image of 100 grippers fabricated with a single squeegee. The inset shows a gripper actuated by a uniform magnetic field of 60 mT. (E) Rolling-based locomotion of a gripper robot for sphere-shaped cargo transport under a rotating magnetic field. (F) Demonstration of a capsule-based robot delivery strategy, with 25 gripper robots sealed in a gelatin capsule. After the capsule dissolves in water, the gripper robots are actuated to escape and perform group locomotion under a rotating magnetic field generated by a permanent magnet. (G) Demonstration of the gripper robot navigating in a trigeminal artery model using rolling-based locomotion under a rotating magnetic field generated by a permanent magnet. (H) Ultrasound tracking image of the gripper robots while navigating in the trigeminal artery model.

The grippers are deployed as drug delivery robots in a scenario that replicates motion inside the fluid environment of the human body (Figure 3.12E). The programmed magnetization profile of the MSGRs also allows for rolling-based locomotion when placed in a rotating magnetic field. Meanwhile, the gripper's folding deformation can firmly grasp and release the object with up to 200% of its body weight. Additionally, the small size and wireless actuation of MSGRs allow them to be packaged in a dissolvable capsule, from which twenty gripper robots were released and manipulated to break free (Figure 3.12F). The escaped gripper robots simultaneously respond to the actuation magnetic field that allows for controllable group behavior. We further explored the potential application of screen-printed MSGRs in minimally invasive surgery. As illustrated in Figure 3.12G, the MSGR is actuated to navigate in a trigeminal artery model. We set up ultrasound imaging to validate the real-time tracking potential of the MSGRs, where the ultrasound imaging results show a clear outline and movements of the gripper robots at a depth of 2.0 cm(Figure 3.12H). These results demonstrate the advantages afforded by screen printing of MSGRs, highlighting the high throughput and reliability of fabrication at small sizes.

### 3.2.4 Multi-modal MSRs embedded with on-board circuitry

Soft electronic devices are increasingly valued in biomedical sciences due to their mechanical compliance with tissue and organs, providing more conformal contact and higher efficient transmission of electrical, optical, and mechanical signals. Recently, magnetic soft materials have enabled the creation of magnetically reconfigurable soft or flexible electronic devices with embedded electronic components, achieved through molding or 3D printing[49], [52]. These devices can perform different electronic functions through shape morphing under applied magnetic fields, featuring dynamic adaptability in electronic performance.

Current fabrication methods require producing a complete magnetic soft robot before assembling the circuits, limiting the fabrication efficiency and inter-layer integration. To overcome the limits, we have employed the screen printing strategy to enable the simultaneous printing of both circuits and actuation modules, offering advantages in versatility, efficiency,

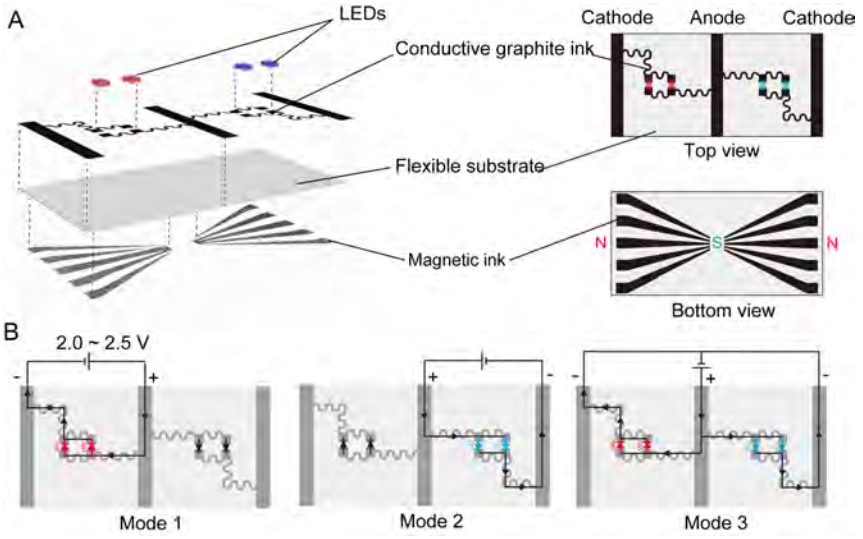


Figure 3.13: Schematic designs and working principles of the screen-printed soft electronic device. (A) Exploded, top, and bottom view of the soft electronic device, in which soft electronic circuitry and magnetic actuators are embedded based on screen-printing. (B) Schematic diagram of the embedded soft electronic circuits, which are designed to turn on only in the designated mode of transformation owing to the selective contact with the electrode on the substrate.

and the seamless integration of multi-modal functionalities. The layered architecture resulting from this process is illustrated in Figure 3.13A, which presents a soft electronic device wherein soft electronic circuitry and magnetic actuators are embedded using screen-printing. A flexible paper-based substrate serves as the structural layer, selected for its superior compatibility with both magnetic and conductive inks. As illustrated in Figure 3.13B, the embedded soft electronic circuits are intricately patterned using conductive graphite ink. This configuration incorporates two LED modules to exhibit three distinct illumination modes, which are achievable through connections to circuit terminals. The circuits are designed to activate only in the corresponding mode of deformation, owing to the selective contact with the electrode on the substrate. Subsequently, magnetic ink is printed on the reverse side of the substrate and subjected to magnetization. Figure 3.14 exhibit the screen-printed soft electronic device to illustrate the activation modes under magnetic fields of identical magnitude (80 mT) ap-

plied in different directions. Specifically, under a horizontal left magnetic field, folding of the left-sided panel activates the red LEDs, and folding of the right-sided panel activates the blue LED while placed in a magnetic field in opposite direction. A vertical upward field induces upward bending with all LEDs illuminated. The seamless integration of heterogeneous materials and components highlights the potential of screen-printed MSRs to advance future soft electronics with multi-layer structures.



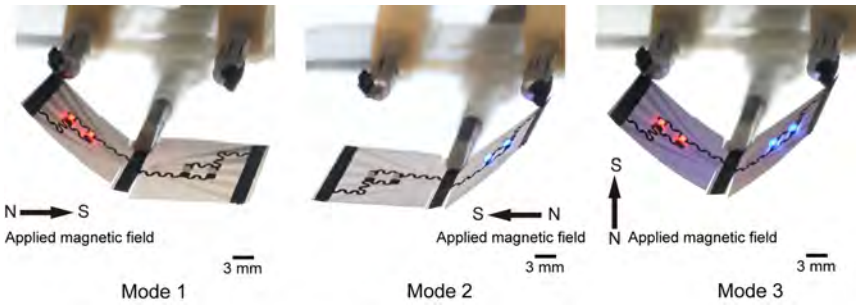


Figure 3.14: Images of the screen-printed soft electronic device activated by magnetic fields in different directions with the same magnitude of 80 mT.

### 3.2.5 Bio-inspired magnetic soft robot with fluorescent coloration

Inspired by natural organisms, robots replicate specific structural and functional features of living creatures, enabling innovative solutions tailored to complex challenges. For instance, their ability to emulate natural locomotion and adaptive behaviors offers practical advantages in tasks such as targeted drug delivery, dynamic environmental monitoring, and interactive educational tools[42], [113]. The designs inspired by a variety of creatures, including those observed in snakes, inchworms, birds, jellyfish, spermatozoa, and turtles, have emerged as a prominent research area in soft robotics. Inspired by butterflies' appearance (Figure 3.15A), along and their efficient flapping motion, we have designed MSRs with a butterfly pattern and flapping behavior. The flapping of the wings is achieved by screen-printing and reorientating magnetic layers on top of polysiloxane substrates.

Biofluorescence is a phenomenon where living organisms absorb electro-

magnetic radiation at a specific wavelength and emit it at a lower energy level and a longer wavelength, playing an important role in camouflage, threat display, and attraction[114], [115]. The integration of fluorescent materials in bio-inspired robots endows more realism, enabling visual feedback and enhancing the aesthetic appeal of soft robots. We create fluorescent ink for screen-printing by mixing polysiloxane with strontium aluminate glow powder, which can be excited by ultraviolet (UV) light and emits visible afterglow (Figure 3.15B). The butterfly robot is constructed through a strategic layering of fluorescent ink and magnetic ink (Figure 3.15C). The magnetic layer is polarized with alternating poles (S-N-S configuration), which enables wing flapping of the butterfly when exposed to an actuating magnetic field. Specifically, we establish the structure through a four-layer printing procedure to integrate the fluorescent layer with magnetic actuators while each layer is illustrated in the exploded schematic of Figure 3.15C. We further demonstrate the magnetic butterfly robot's response under both natural and fluorescent color conditions.



In Figure 3.15D, the robot is shown in its natural color, both at rest and during actuation under a uniform magnetic field of 50 mT. In Figure 3.16A, the robot displays its fluorescent color, with a distinct afterglow observed following UV excitation (wavelength, $\sim$410 nm), highlighting its luminescent properties. These functionalities operate in parallel rather than interactively, their simultaneous yet independent operation is an important achievement, highlighting the compatibility and non-interference between magnetically and optically responsive systems. Fluorescent coloration, activated externally by UV exposure, provides a stand-alone visual functionality ideal for bioimaging or environmental sensing. Meanwhile, independent magnetic actuation enables precise shape morphing (Figure 3.16B). This decoupled design approach ensures modularity, allowing each functional system to be individually optimized and adapted for a wide range of applications. This combined concept of screen-printed MSR exemplifies the potential for integrating aesthetics and functionality into soft robotic systems, broadening application prospects in biomedical imaging, and educational robots.

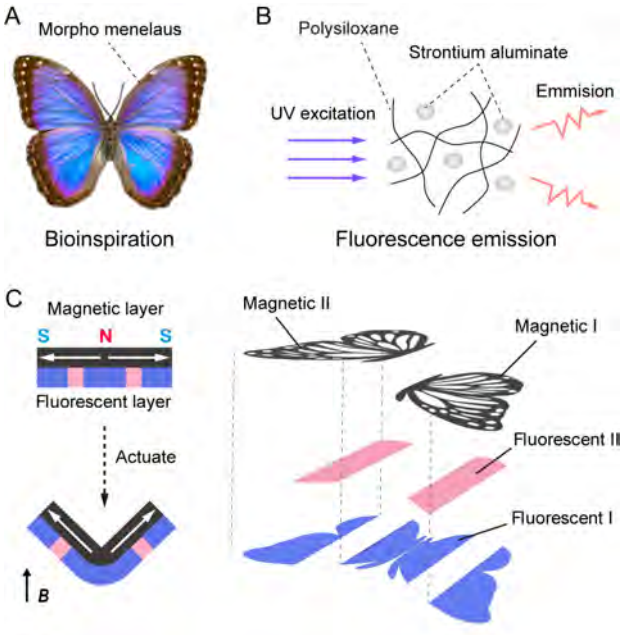


Figure 3.15: Bio-inspired butterfly robot with fluorescent coloration. (A) Image of the butterfly (Morpho Menelaus) for bioinspiration. (B) Fluorescence afterglow emission mechanism of fluorescent ink. (C) Schematic illustration of the layer structure and actuation mode of screen-printed butterfly robot.

## 3.3 Discussion

In this study, we have introduced a screen-printing-based multi-layer fabrication scheme for magnetic soft robotics. This method harnesses the unique advantages of screen-printing, including broad applicability across various materials and patterns, as well as layering which seamlessly integrates distinct functional layers. We have demonstrated a precise deposition process and improved the printability of magnetic ink with a high filler ratio (50 wt.%) and stable rheological properties. The comprehensive material applicability of the screen-printing method has been verified by successfully printing on diverse substrates and actuating in magnetic fields. We also applied the multi-step magnetization procedure to customize the magnetic responses. The screen-printing technique is demonstrated through various examples, including bio-inspired mimosa leaves, origami cubes, undulat-

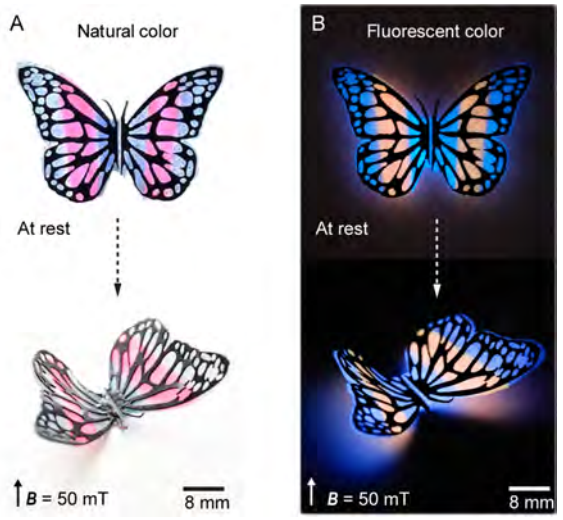


Figure 3.16: (A) Screen-printed butterfly robot at rest and being actuated when placed in natural light. (B) Screen-printed butterfly robot at rest and being actuated after being excited by ultraviolet (UV) light (wavelength ∼410 nm).



ing rings, and reconfigurable surfaces, all capable of programmable 3D shape morphing. Building upon these demonstrations, three advanced applications are showcased: tether-free gripper robots designed for biomedical purposes, fully printed three-layer soft robots integrated with onboard circuits for actuatable soft electronics, and a bio-inspired butterfly robot featuring fluorescent coloration. Collectively, these examples underscore screen-printing's versatility and potential for creating functional magnetic soft robots (MSRs) with diverse capabilities.Despite these strengths, inherent limitations exist in fabricating fully 3D freeform architectures with screen-printing. Compared to extrusion-based 3D printing methods such as direct ink writing (DIW) and fused filament fabrication (FDM), screen-printing typically restricts the thickness of the designs to a few tenths of a millimeter and limits the bridging distances achievable. Nonetheless, screen-printing excels in applications demanding exceptional planar resolution, rapid prototyping, and scalable production of 2D and 2.5D structures. These unique capabilities position screen-printing as a promising method for mass production and functional integration, particularly suited to automation industries, biomedical devices, and educational settings.

While the screen-printing strategy is demonstrated to be a noteworthy advance for the fabrication of MSRs with silicone mixtures, we propose further exploration of water-based material systems, including hydrogels and other dispersions, to elevate the integration of the screen-printed MSRs in high-demand applications such as minimally invasive surgery and tissue engineering. Such efforts could involve investigating alternative water-based ink matrices that exhibit optimized rheological properties, stable boundary attachment, and robust mechanical performance. Furthermore, due to magnetic reorientation strategy inherently supports batch programming, enabling simultaneous magnetization of multiple robot components sharing identical polarization directions in a single step, future automation could involve incorporating conveyor belt-based magnetic programming stations or programmable magnet arrays, streamlining mass production and enabling rapid, high-throughput manufacturing of magnetic soft robots. Developing an automatic configuration algorithm that converts the demanded deformation modes to simple printing and magnetic reorientation sequences is also important in the future automation. These explorations would significantly broaden the adaptability and functionality of soft robotics. We envision that the screen-printing of MSRs could provide a foundation for untethered soft robots and flexible electronics, enabling their deployment in diverse biomedical and industrial applications while advancing scalable and cost-effective manufacturing methods.

## 3.4 Materials and methods

### 3.4.1 Ink Preparation

#### 3.4.1.1 Magnetic Ink Preparation

To prepare the magnetic ink, we utilized a composite system consisting of magnetic particles and elastomers. Magnetic particles (PrFeB, MQFPTM-16-7) were selected due to their high magnetic remanence. Before mixing, all the PrFeB particles were magnetized beyond saturation using an impulse magnetizer (IM-10-30, ASC SCIENTIFIC, USA). The elastomer matrix, Dragon Skin 30 (Smooth-On, USA), was prepared by mixing silicone resin and curing agent at a 1:1 weight ratio. The PrFeB particles were gradually added to the matrix at a 1:1 weight ratio, and the entire formulation was

blended by an overhead stirrer (NANOSTAR, IKA, Germany) at $\tilde{2}000$ r.p.m. for 2 minutes to ensure homogeneity. The final mixture was degassed for 5 minutes in a vacuum chamber to eliminate air bubbles.

#### 3.4.1.2 Conductive ink preparation

The conductive ink is prepared by mixing Electric Paint (Bare Conductive, UK) with glycerin (Glycerol, Sigma-Aldrich, USA) in a volume ratio of 100:1. The final mixture was degassed for 5 minutes in a vacuum chamber to eliminate air bubbles.



#### 3.4.1.3 Fluorescent ink preparation

Strontium aluminate based glowing powder (purchased from Alibaba, China) was blended with Dragon Skin 30 (Smooth-On, USA) in a volume ratio of 1:1. The final mixture was degassed for 5 minutes in a vacuum chamber to eliminate air bubbles.

### 3.4.2 Screen-Printing Procedures

The magnetic soft robots were fabricated using a layer-by-layer screen-printing technique developed previously[10]. A piece of 120 mesh nylon net with a laser-cut screen was tense and mounted onto a 3D-printed frame (Figure 3.17). Each layer of magnetic ink was deposited by sweeping a polyurethane squeegee at an angle of around 70° and a manually controlled pressure. The substrates, including elastomer films, paper, glass, and wood, were secured onto the printing stage. After printing each layer, the ink was cured at 80°C for 10 minutes on a heating platform. For multi-layered devices, additional layers were printed following the same procedure.

### 3.4.3 Magnetic programming

We employed two magnetic programming methods in this research to streamline the fabrication process depending on the requirements of specific samples. The majority of samples are programmed by magnetic reorientation, as demonstrated in our previous research[116], where particles are aligned in a relatively weak magnetic field. Each alignment sequence required approximately 5 seconds within a pair of electromagnetic coils at a magnetic

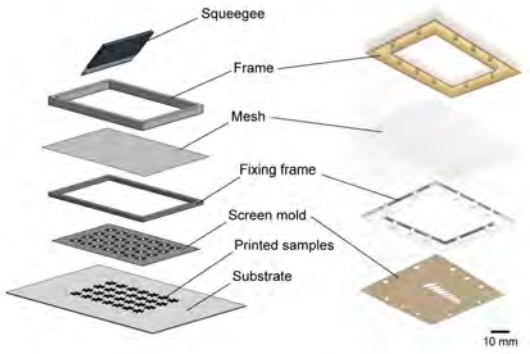


Figure 3.17: Exploded view diagram and corresponding components of the multi-layer screen-printing system, illustrating the structural arrangement from the squeegee to the substrate.

induction intensity of 80 mT. After alignment, each programmed region was cured at 100 °C for an additional 30 seconds.

For more complex structures, such as the origami cube (Figure 3.9C) and gripper robots (Figure 3.12), we applied magnetization by an impulse magnetizer (IM-10-30, ASC SCIENTIFIC). The samples were first fixed to deform in an acrylic mold and magnetized in the impulse magnetizer for less than 1 second under a strong magnetic field of 2.5 T. This method was chosen because these designs require stronger magnetic responses and multiple directional alignments, which would necessitate repeated printing cycles if using magnetic reorientation, thus potentially compromising positional accuracy.

### 3.4.4 Rheological Test

The rheological properties of the magnetic ink were measured using a rotational rheometer (Anton Paar MCR 302). The ink was loaded onto the parallel plate fixture with a 25 mm diameter at a 1 mm gap. A shear rate sweep was performed from $0.01\,s^{-1}$ to $1000\,s^{-1}$ at room temperature to determine the ink's viscosity and shear-thinning behavior, crucial for the screen-printing process. Additionally, oscillatory tests were conducted to measure the storage modulus (G') and loss modulus (G") at a constant frequency of 1 Hz, providing insights into the viscoelasticity of the ink.

### 3.4.5 Surface Morphology Test

The surface morphology test in Figure 3.5A was analyzed using a two-axis morphology meter (Scantron Industrial Proscan 2000, UK).The sample was scanned by a laser sensor by line in the Y direction with 0.01 mm accuracy. The data was processed by R version 4.3.1 to generate the contour plot.

### 3.4.6 SEM Characterization

Scanning electron microscopy (SEM, Thermo Fisher Apreo S, USA) was used to examine the morphologies and mesoscopic structures of the printed film. The sample was spread flat and securely affixed to the test bench before SEM characterization and analyzed at an accelerating voltage of 10 kV. This characterization allowed us to observe the printing quality and dispersion of the magnetic particles in the elastomer matrix.



### 3.4.7 Finite element analysis

For the designs presented in Figure 3.5A, Figure 3.10 and Figure 3.12C, deformations in the presence of external magnetic fields were simulated using the Solid Mechanics and Magnetic Fields, No Currents (mfnc) module in COMSOL Multiphysics 5.4.

### 3.4.8 Material mechanical characterization

The tensile tests are conducted using a texture analyzer (CT3, AMETEK GmbH B.U. Brookfield). Standardized testing samples made of Dragon skin 30 and the magnetic composites are subjected to axis tensile tests as per ASTM standard tests. The loading speed for the tests is set to 1 mm/s, and the testing range is set to 200% strain.

# 4

# Biohybrid Magnetic Soft Robots for Targeted Microbial Colonization in Ulcerative Colitis Treatment



***Note:*** *The following chapter is adapted from the article "Biohybrid Magnetic Soft Robots for Targeted Microbial Colonization in Ulcerative Colitis Treatment" by* ***Z. Wang****, L. Ding, S. Misra, D. Zhang, and V. K. Venkiteswaran, submitted to "Advanced Materials"*

Ulcerative colitis (UC) is commonly associated with microbial dysbiosis, yet probiotic therapies often fail to achieve durable, site-specific colonization because retention in the gastrointestinal tract is transient. Here, we develop magnetic carrier robots (MCRs) with a biohybrid structure that merges untethered magnetic actuation with a probiotic-encapsulating hydrogel. The MCRs are produced by scalable multi-layer screen-printing, in which a neodymium-iron-boron (NdFeB)/polydimethylsiloxane (PDMS) magnetic elastomer layer is integrated with an alginate hydrogel layer that preserves bacterial viability and supports localized release. Wireless navigation and positioning are demonstrated along programmed trajectories and in a colon phantom using an external robotic arm–assisted magnetic actuation system. In live mice with 3% dextran sulfate sodium (DSS)-induced colitis, magnet-localized MCR treatment accelerates clinical recovery, significantly increases gut microbiota community diversity, and significantly mitigates colon shortening (colon length, $n = 5$ per group, $p < 0.01$). This work advances biohybrid magnetic soft robotics from actuation demonstra-

tions to therapeutic function, providing a scalable basis for future localized microbial treatment in UC.

## 4.1 Introduction

Ulcerative colitis (UC) is a lifelong inflammatory bowel disease (IBD) that affects the rectum and colon, with common symptoms including rectal bleeding in more than 90% of patients[117], [118]. Though the pathogenesis of ulcerative colitis remains incompletely understood, growing evidence indicates that ulcerative colitis is associated with impaired intestinal mucosal barrier function and intestinal microecology dysbiosis[119]–[123]. Current treatments and maintenance for ulcerative colitis mainly rely on 5-aminosalicylic acid (5-ASA), immunosuppressants (thiopurines), steroids, and antibiotics. These medications can lead to a range of systemic side effects with prolonged use, including nephrotoxicity, hepatotoxicity, and gut dysbiosis[124], [125]. Microbiome-based therapies such as fecal microbiota transplantation (FMT) have shown clinical promise in IBD[126]–[128], including improving symptoms and achieving remission in a subset of patients, but outcomes remain difficult to control. Treatment response varies widely, as strain engraftment and downstream community shifts depend strongly on both donor composition and recipient factors and are not reliably predictable. In addition, safety concerns such as pathogen transmission necessitate stringent donor screening and standardized manufacturing and handling procedures.

The development of engineered probiotics in combination with targeted delivery can help address these limitations by improving consistency, safety, and localization of therapeutic effects. Probiotics can promote microbiota balance and support mucosal barrier function, and probiotic-based approaches have been explored for a range of conditions including inflammatory disorders, rheumatic disease, cancer-associated complications, hypertension, and diabetes[129]–[132]. In particular, commensal bacteria from the families *Enterobacteriaceae*, *Lactobacillaceae*, and *Bifidobacteriaceae* have been evaluated as therapeutic or adjunctive agents in IBD and shown to modulate cytokine production (e.g., IL-10), IgA responses, and $T_{\text{reg}}$-cell-mediated immune regulation[133]–[140].As a commonly used clinical route of administration, orally administered probiotic or live biotherapeutic formulations often lose viability during gastric transit and bile

exposure. Rapid transit, immune clearance, and competition with resident microbiota further limit colonization and therapeutic durability, which can necessitate frequent dosing or protective formulations.[141].

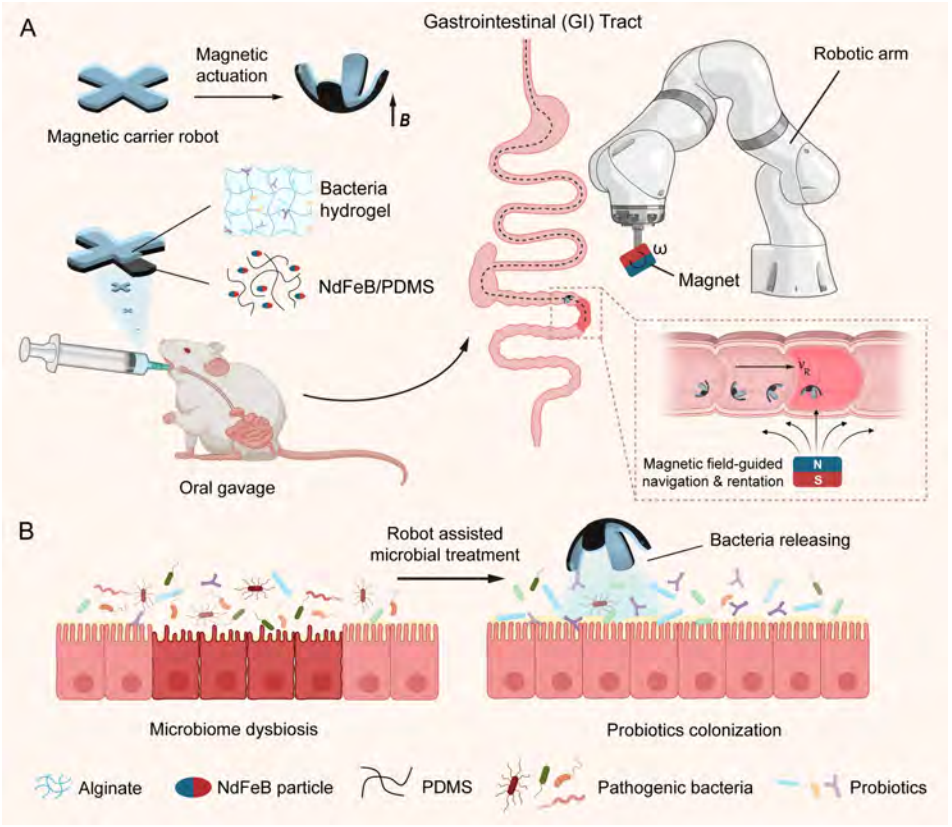


Figure 4.1: Schematic of magnetic carrier robots (MCRs) for localized probiotic delivery in the gastrointestinal tract. (A) Design and operating concept of MCRs. Each MCR comprises a magnetic elastomer layer of neodymium-iron-boron (NdFeB) particles embedded in polydimethylsiloxane (PDMS) and a probiotic-loaded alginate hydrogel layer. After oral gavage, a spinning permanent magnet on a robotic arm is programmed to generate a rotational magnetic field ($\boldsymbol{B}$) that guides the MCRs for navigation and targeted retention at specific sites. (B) Therapeutic mechanism schematic. MCR-assisted microbial therapy delivers concentrated probiotics directly to the diseased epithelium, enhancing local colonization and helping restore microbiome balance compared with dysbiosis in untreated IBD.

To improve intestinal retention and localization of delivered probiotics, a wide range of delivery strategies has been explored, including utilizing of stimuli-responsive hydrogels, gas-generating systems, and biohybrid "living" constructs. Hydrogel matrices can prolong intestinal retention and protect payloads during transit, exemplified by an inulin-based hydrogel system with long retention for colitis therapy and related complications[142]. Materials that directly augment bacterial function further enhance durability after dosing, including ROS-scavenging adhesive probiotic "backpacks" and adhesive "living glue" coatings that promote gut colonization and therapeutic efficacy in colitis models[143], [144]. Multicellular self-organized probiotic assemblies provide an additional route to improve acid and bile tolerance and markedly increase intestinal colonization[145]. However, precise control over the spatiotemporal trajectory of probiotics remains limited in current therapeutic interventions. Without the ability to actively steer and program the delivery path, probiotics are prone to off-target exposure and dilution before reaching the infected target. Therefore, developing a platform with programmable locomotive control is essential to transition from stochastic delivery to a deterministic, site-specific therapeutic strategy.

Magnetic actuation provides a path toward deterministic delivery, since magnetically driven capsules and magnetic soft robots can be navigated and anchored in the GI tract and can support on-demand functions such as tissue attachment and triggered release[19], [55], [146]–[148]. Motivated by this idea, we propose an on-site delivery strategy based on magnetic carrier robots (MCRs) with a biohybrid structure that enables wireless, real-time control of localization (Figure 4.1A). A bi-layer architecture is designed for the MCRs. The outer layer is a polydimethylsiloxane (PDMS) polymer embedded with neodymium–iron–boron (NdFeB) particles to enable wireless magnetic actuation and compliant contact, and the inner layer is a probiotic-loaded hydrogel that protects bacteria from pH stress and supports localized release after prolonged retention at the target site. For precise positioning of the MCRs in GI tract, a wireless actuation platform based on a robotic arm is developed. By controlling the magnet's position and rotation, the external field generates torque and traction on the NdFeB/PDMS layer, enabling guided rolling locomotion, steering through tortuous lumens, and on-demand positioning at predefined sites. A focused local magnetic field further promotes magnetic trapping and prolonged re-

tention at the target region for site-selective microbial delivery. Positioning accuracy and retention were evaluated in multiple colon-mimicking test tracks and a colon phantom, demonstrating flexible, controllable locomotion and stable on-demand localization. Therapeutic efficacy is assessed in a dextran sulfate sodium (DSS)-induced colitis model in live mice following magnet-localized administration.

In live mice, *in vivo* therapeutic validation is achieved by magnet-localized oral delivery of MCRs, which accumulate at inflamed colonic regions under external magnetic control and deliver a high local probiotic dose to support engraftment and colonization (Figure 4.1B). Colitis severity is reduced, as evidenced by improved disease activity index and body-weight recovery, preservation of colon length, ameliorated histopathology (H&E staining), and microbiome modulation quantified by 16S rRNA sequencing. This work establishes a programmable delivery strategy for living probiotics enabled by magnetically controlled soft robots, emphasizing precise motion control and prolonged intestinal retention, and provides a generalizable framework for future gastrointestinal robotics and targeted microbiome-based therapies.

## 4.2 Results and Discussion

### 4.2.1 Fabrication and Characterization of MCRs

MCRs are fabricated using a two step screen-printing process developed in previous study that sequentially patterns a magnetic elastomer layer and a bacteria-loaded alginate hydrogel (Figure 4.2). First, using a screen-printing setup illustrated in previous chapter, magnetized NdFeB particles ($\sim 50\,\mu$m) are dispersed in liquid PDMS to obtain a homogeneous magnetic ink. This ink is flooded across a stenciled nylon mesh and driven through the open areas onto the substrate by a squeegee pass, forming the magnetic layer. The printed films are cured for 10 min at 80°C and then magnetically programmed as illustrated in Figure 4.2.



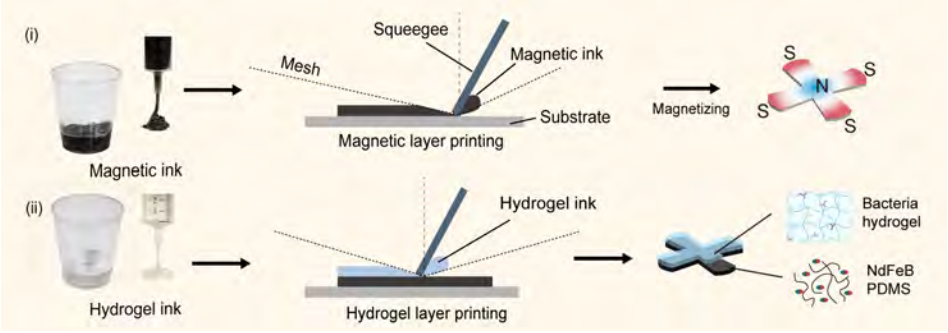


Figure 4.2: Schematic of the two-step screen-printing process in which a NdFeB/PDMS magnetic ink is first patterned through a mesh onto the substrate, cured, and magnetized, followed by printing of the bacteria-loaded alginate hydrogel ink on top of the magnetic layer.

Because the cured NdFeB/PDMS surface is hydrophobic (water contact angle 93.8°), the robots are subjected to oxygen plasma treatment, which reduces the contact angle to 37.4° and thereby improves the wetting and adhesion of the aqueous hydrogel ink (Figure 4.3A). For the hydrogel layer, a freeze-dried cocktail of probiotic strains is resuspended in 10 wt% sodium alginate to obtain a viscous, shear-thinning bacterial ink suitable for screen printing. The hydrogel ink is loaded onto a second mesh carrying the desired stencil and, after a flooding step, is printed directly onto the plasma-treated magnetic layer using a controlled squeegee stroke. The

deposited ink spreads and self-levels to form a continuous coating with a thickness of approximately 100 $\mu$m, as confirmed by cross-sectional imaging (Figure 4.3B). Immediately after printing, the patterned hydrogel is mist-sprayed with 0.1 M $CaCl_2$, which rapidly cross-links the alginate network and immobilizes the bacteria within a mechanically stable layer on top of the magnetic substrate.

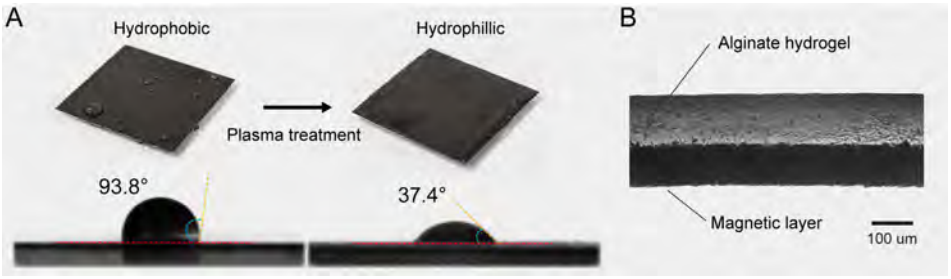


Figure 4.3: (A) Photographs and contact-angle measurements of the NdFeB/PDMS surface before and after oxygen plasma treatment, showing a transition from hydrophobic (93.8°) to hydrophilic (37.4°), and (B) optical cross-sectional image of the resulting alginate-magnetic bi-layer structure.

After fabrication, the morphology and composition of MCRs are first examined via an optical micrograph (Figure 4.4A). A representative cross-shaped robot with a lateral size of 300 $\mu$m, demonstrating that the screen-printing process produces well-defined microscale patterns. Scanning electro microscopy (SEM) image with elemental further reveals a continuous NdFeB/PDMS elastomer layer in which the magnetic particles are finely dispersed within the polymer matrix, with no visible aggregation at the microscale (Figure 4.4B). Elemental mapping by energy-dispersive X-ray spectroscopy further confirms this composite structure. The Si map displays a uniform signal that corresponds to the PDMS phase, whereas Nd appeared as densely and evenly distributed spots, indicating homogeneous dispersion of NdFeB particles within the PDMS matrix (Figure 4.4C,D).

The magnetic properties of the composite elastomers are characterized for different NdFeB to PDMS mass ratios (1:2, 1:1, and 2:1). The hysteresis loops show typical ferromagnetic behavior with finite coercivity and remanent magnetization for all three mixing ratios(Figure 4.5A). Increasing the particle loading results in a monotonic rise in saturation magnetization and remanent magnetization, with the 2:1 composite exhibiting the high-

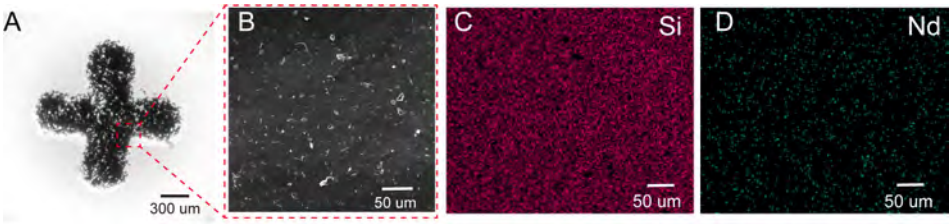


Figure 4.4: (A) Optical micrograph of a cross-shaped MCR (scale bar: 300 $\mu$m). (B) Scanning electron microscopy (SEM) image of the magnetic layer, and corresponding EDS elemental maps of (C) Si and (D) Nd, confirming homogeneous dispersion of NdFeB particles in the PDMS matrix.



est magnetic moment over the entire applied field range. The 1:1 and 1:2 inks display lower magnetization, consistent with dilution of the magnetic particles by the elastomer. These results represent that the magnetic responses of the MCRs can be tuned by adjusting the NdFeB content, while preserving sufficient coercivity for stable programmed magnetization.

The XRD pattern of the PDMS/NdFeB composite shows the characteristic diffraction peaks of NdFeB (Figure 4.5B), which match well with the standard $Nd_2Fe_{14}B$ phase (PDF#00-036-1296). The main peaks observed in the experimental pattern correspond to the tetragonal $Nd_2Fe_{14}B$ crystalline structure, indicating that NdFeB powder is the dominant crystalline filler in the PDMS matrix.

The mechanical properties of the magnetic layer were evaluated by uniaxial tensile testing and compared with those of the alginate hydrogel. The stress–strain curves indicate that the load-bearing capability of the NdFeB/PDMS composites increases with particle content within the tested range (Figure 4.5C). At 10% strain, the composites sustained stresses of 141.4 kPa (1:2), 182.9 kPa (1:1), and 236.4 kPa (2:1), whereas the alginate hydrogel reached only 6.53 kPa at the same strain. This gap persisted at higher deformation. At 25% strain, the stresses further increased to 257.1 kPa (1:2), 314.3 kPa (1:1), and 438.2 kPa (2:1), while alginate reached only 15.24 kPa. These results confirm that the magnetic layer provides the primary stiffness to support programmed magnetization and actuation, while the overlying alginate hydrogel contributes a compliant, cell-friendly environment for encapsulated probiotics. The durability of the MCRs were further evaluated after long-term exposure to simulated

gastric fluid (SGF) without pepsin under different pH conditions. During the test, no obvious structural damage or degradation was observed, indicating strong acid–base tolerance. This stability highlights the suitability of MCRs for operation in the gastrointestinal tract, where pH varies substantially across different regions and physiological states (Figure 4.6).

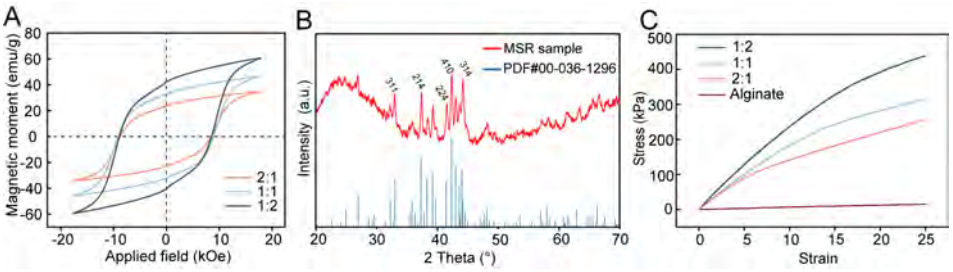


Figure 4.5: (A) Magnetic hysteresis loops of NdFeB/PDMS composites with different NdFeB:PDMS mass ratios (1:2, 1:1, and 2:1), demonstrating tunable remanent magnetization and saturation magnetization. (B) X-ray diffraction pattern of the magnetic composite, with peaks indexed to the crystalline $Nd_2Fe_{14}B$ phase. Standard PDF card #00-036-1296 is plotted for reference. (C) Uniaxial tensile stress-strain curves for NdFeB/PDMS composites with different particle loadings and for pure alginate hydrogel, highlighting the higher stiffness of the magnetic elastomer relative to the soft hydrogel layer.

### 4.2.2 Programmable Locomotion of MCRs

The wireless motion control of the MCRs is characterized by multiple test tracks that mimic key geometric and frictional features of the colon. The wireless actuation platform based on a robotic arm provides a rotating magnetic field at a prescribed frequency that generates torque and traction on the magnetized MCRs. MCR trajectories are recorded by an overhead camera and analyzed with an automated tracking pipeline. On a straight track, the MCR translated along the channel with nearly linear distance–time behavior(Figure 4.7A-C).Experiments were performed under two surface conditions: a dry PDMS surface ("no mucus") and the same surface coated with a thin mucus layer prepared from simulated gastrointestinal fluid ("with mucus"), each tested at external magnet rotation frequencies of 100, 200, 400, and 600 r/min. In both cases, the travel

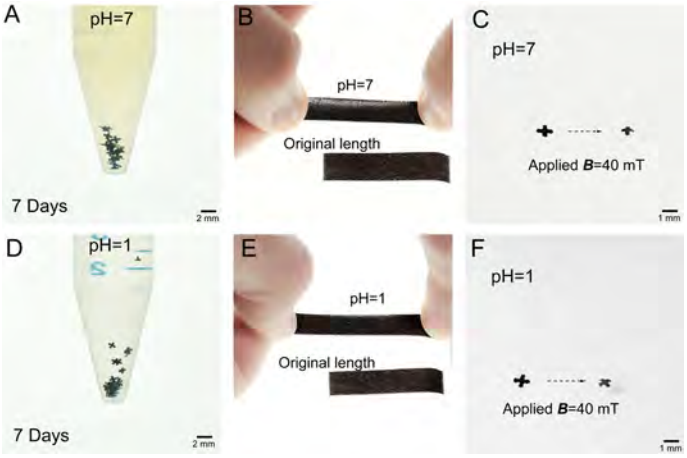


Figure 4.6: Durability of the MCRs after long-term exposure to simulated gastric fluid (SGF, without pepsin) under different pH conditions.(A–C) MCRs treated in SGF at pH = 7 for 7 days. (D–F) MCRs treated in SGF at pH = 1 for 7 days. (A,D) Images showing no obvious structural damage or degradation after treatment. (B,E) The treated MCR materials preserved their mechanical properties and elasticity, with no significant change compared with the original state. (C,F) Magnetic actuation of the treated MCRs under an applied magnetic field of $\boldsymbol{B}$ = 40 mT, confirming retained magnetic responsiveness.

distance increased linearly with time, and higher rotation frequencies produced increased velocities. To evaluate the locomotive performance in more complex geometries, we fabricated a molded silicone track with periodic transverse ridges that mimics human colonic folds (Figure 4.7D).

The cross-shaped MCR is able to move along the corrugated path in both dry and mucus-covered conditions, as shown by the overlaid trajectories in Figure 4.7E. As shown in Figure 4.7F, the rolling MCR under 100–600 r/min actuation exhibits a path-dependent near-linear distance–time behavior, with propulsion speed increasing monotonically with increasing actuation frequency. Compared with the dry condition, the mucus-coated surface showed higher average speed at the tested frequencies, suggesting that the mucus modulates traction between MCRs and the colon wall.

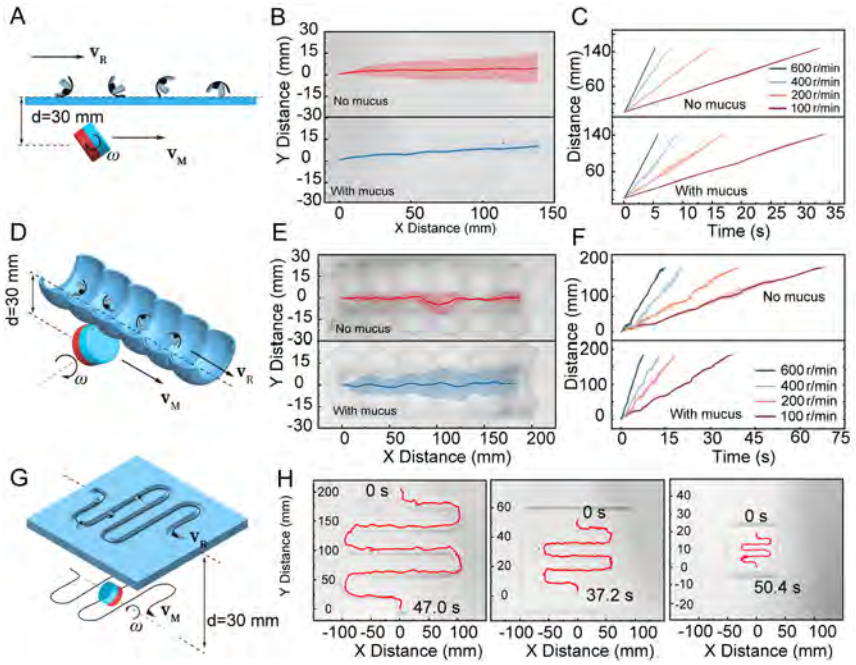


Figure 4.7: Wireless locomotion and navigation of magnetic carrier robots (MCRs) on test tracks. In the schematics, d = 30 mm denotes the center-to-track distance between the disk magnet and the lowest surface of the test tracks. $\omega$ is the rotational angular velocity of the magnet. $\mathbf{v}_R$ indicates the instantaneous velocity direction of the MCR, and $\mathbf{v}_M$ indicates the instantaneous translational velocity direction of the magnet. (A) Schematic of locomotion of an MCR on a straight track driven by a rotating permanent magnet mounted on a translating robotic arm. (B) Representative snapshot overlaid with the averaged trajectory of an MCR moving along a straight track without mucus and with a mucus layer prepared from simulated gastrointestinal fluid. (C) Travel distance versus actuation frequency on the straight track. (D) Schematic of locomotion in a molded silicone channel with transverse ridges mimicking colonic folds. (E) Representative snapshot overlaid with the averaged trajectory of an MCR moving along a 3D-printed colon-structured track without mucus and with a mucus layer prepared from simulated gastrointestinal fluid. (F) Distance–time plots on the corrugated track at different frequencies, again showing frequency-dependent motion attenuated by mucus. (G) Schematic of navigation in a planar serpentine track guided by coordinated rotation and translation of the external magnet. (H) Representative snapshots overlaid with reconstructed trajectories of an MCR navigating a 3D-printed serpentine track, scale bars, 2 mm.

The controlled navigation in a 3D-printed serpentine planar track representing a simplified colonic pathway is tested (Figure 4.7G). By coordinating the rotation and translation of the external magnet along a predefined path, the MCR could be driven from the entrance to the outlet while negotiating multiple bends. The reconstructed trajectories and corresponding elapsed times (Figure 4.7H) demonstrate that the robots reliably follow the designed path under fully wireless magnetic control, highlighting the feasibility of programmed navigation through narrow, tortuous intestinal-like geometries.

In order to evaluate locomotion in an anatomically relevant environment and simulate rectal administration, MCR navigation was further tested in a colon phantom for endoscopy training that reproduces the gross geometry, curvature, and lumen diameter of the human colon (Figure 4.8A). MCRs were introduced through the distal entrance of the phantom and driven toward proximal regions along the prescribed route using an external permanent magnet mounted on a robotic arm, which was rotated and translated outside the phantom following the same actuation scheme used in benchtop tracks. A standard endoscope was advanced through the colonic lumen to visualize the robot in real time, and representative snapshots were collected at four characteristic locations (Sections A–D). In each section, the robot position and trajectory were overlaid within the endoscopic field of view, showing progressive motion over elapsed intervals of 28.0 s (Section A), 20.1 s (Section B), 16.0 s (Section C), and 36.1 s (Section D) from the initial frame at 0 s (Figure 4.8B-E). These results demonstrate that MCRs remain trackable under endoscopic imaging and can be magnetically guided along the folded colonic lumen, around bends, and through locally narrowed regions, supporting the feasibility of integrating wireless magnetic actuation with clinically relevant rectal delivery workflows.

Notably, MCRs can be deployed through either oral gavage or rectal enema depending on the target anatomy and intestinal accessibility. Magnetic positioning is therefore adapted to the administration route. For large lumens such as the human colon, rectal placement provides a practical route to position the robots directly within the distal colon, where an external permanent magnet mounted on a robotic arm can assist actuation and guidance. In small animals with narrow colonic dimensions (e.g.,

mice), device insertion is generally limited to oral gavage for gastrointestinal entry. In this setting, robotic-arm translation offers limited positioning precision because the arm's motion error can be comparable to, or larger than, the organ scale. Accordingly, a permanent magnet is affixed at a predefined external location to enhance local magnetic trapping and prolong intestinal retention at the target site.

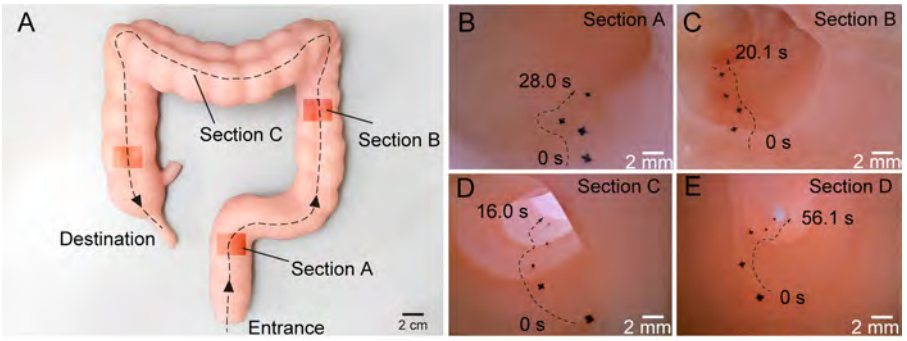


Figure 4.8: Wireless locomotion and navigation of magnetic carrier robots (MCRs) in a colon phantom. (A) Schematic of a colon phantom for endoscopy testing, indicating entrance, destination, and four sections (A–D). (B-E) Endoscopic images from sections A–D with overlaid trajectories and time stamps, illustrating wireless guidance of MCRs around bends and through confined regions under clinically relevant visualization, scale bars, 2 mm.

### 4.2.3 Bacteria Releasing of Magnetic Carrier Robots

In addition to demonstrating programmable locomotion and clinically relevant navigation of MCRs, the therapeutic function requires that the MCRs release viable probiotics in a controlled manner after deployment. Therefore, bacterial viability during ink formulation, gelation, and subsequent release is evaluated by live/dead fluorescence staining (Figure 4.9). In the Bacteria + PBS group, a dense population of rod-shaped cells exhibits bright SYTO 9 fluorescence with only sporadic PI-positive events, indicating a highly viable starting suspension. Dispersion of bacteria in the 10 wt% alginate printing formulation (Bacterial alginate ink) maintains this profile: green signal intensity and cell morphology are similar to the control, and only a slight increase in red fluorescence is observed, suggesting

that exposure to the viscous alginate matrix and mixing imposes minimal additional membrane damage.

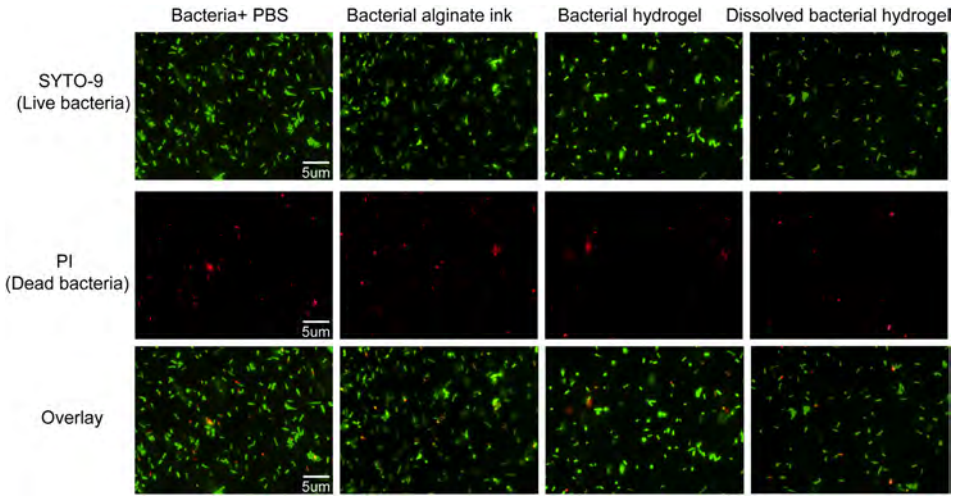


Figure 4.9: Viability of probiotics during ink formulation, hydrogel crosslinking, and dissolution. Representative fluorescence micrographs of probiotic bacteria stained with SYTO-9 (live, green) and propidium iodide (dead, red) under four conditions: bacteria in PBS (Bacteria + PBS), bacteria dispersed in alginate printing ink (Bacterial alginate ink), bacteria encapsulated in crosslinked alginate hydrogel (Bacterial alginate gel), and bacteria released after dissolution of the hydrogel (Dissolved bacterial alginate gel). Overlay images show that bacterial populations remain predominantly SYTO-9-positive throughout the printing and release process, indicating high viability is preserved in the alginate-based delivery matrix.

After ionic crosslinking to form the Bacterial alginate gel, the majority of encapsulated cells remain strongly SYTO 9-positive with very few PI-positive bacteria, demonstrating that the gelation process and confinement within the hydrogel network do not substantially compromise viability. Upon dissolution of the cross-linked gel to emulate bacterial release (Dissolved bacterial alginate gel), the population remains predominantly green, although a modest increase in red and yellow (dual-stained) cells is evident relative to the intact gel. Overall, qualitative live/dead staining across all four conditions indicates that the alginate-based ink formulation, gelation, and dissolution processes maintain high bacterial viability, supporting the suitability of this hydrogel system for probiotic loading and

controlled release in the MCRs platform.

### 4.2.4 *In Vivo* Therapeutic Effects of MCRs Delivered Probiotics Against DSS-Induced Ulcerative Colitis

To evaluate the therapeutic efficacy of probiotic-loaded magnetic carrier robots, ulcerative colitis was induced in live mice by administering 3% (w/v) dextran sodium sulfate (DSS) in the drinking water for 7 consecutive days (Figure 4.10). All mice were randomly assigned to five groups: Control, DSS, MCR, BH, and MCR-BH. The Control group received normal drinking water without DSS. The DSS group received DSS to establish colitis without further intervention. The MCR group received DSS followed by oral gavage of blank robots, with an external magnet placed on the abdomen to promote distal-colon localization and retention for 2 days.



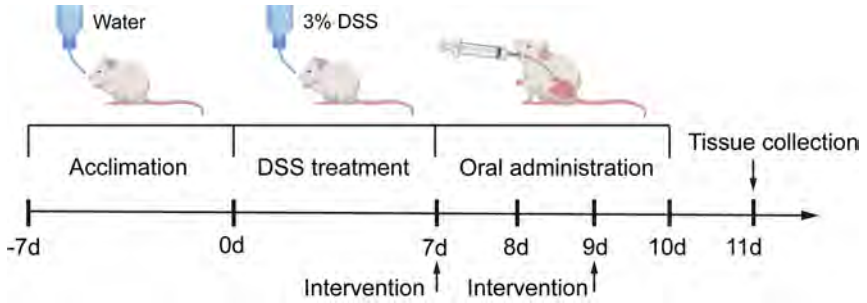


Figure 4.10: Experimental timeline: 7 d acclimation, 3% DSS in drinking water from day 0-7, oral gavage of blank MCRs, probiotic hydrogel (BH), or probiotic-loaded MCRs (MCR-BH) on days 7 and 9, and tissue collection on day 11.

The BH group received DSS followed by oral gavage of 0.1 g probiotic-loaded alginate hydrogel (equivalent to $10^8$ CFU). The MCR-BH group received DSS followed by oral gavage of multilayer, screen-printed MCRs carrying probiotic-loaded alginate hydrogel, and an abdominal magnet was similarly applied to enhance local trapping and retention for 2 days. MCRs were delivered by oral gavage because precise *in situ* positioning is constrained by the small colonic diameter space in mice.

The MCR capturing and retention experiment was characterized by X-ray (Figure 4.11A). Therapeutic efficacy was first assessed by tracking

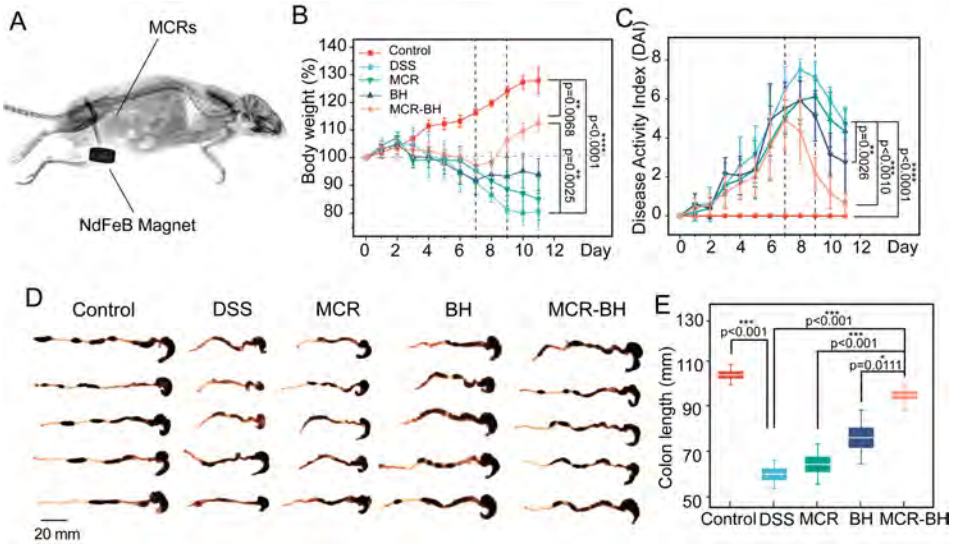


Figure 4.11: (A) Schematic of *in vivo* magnetic localization, with an external NdFeB magnet positioned over the distal colon. (B) Changes in body weight (percent of baseline) for Control, DSS, MCR, BH, and MCR-BH groups. (C) Disease activity index (DAI) versus time for the same groups. (D) Representative macroscopic images of colons harvested on day 11. (E) Quantification of colon length (box-and-whisker plots) showing DSS-induced shortening and its attenuation by BH and, most prominently, by MCR-BH.

body-weight changes across groups throughout the experimental period, as body weight serves as a sensitive indicator of disease onset and progression in DSS-induced colitis. As shown in Figure 4.11B, the healthy control group exhibited a steady increase in body weight throughout the study, reaching 126% of the initial weight by day 11. During DSS induction (day 0-7), body-weight loss was comparable across all DSS-exposed groups, and minor deviations among trajectories were attributed to inter-animal variability rather than treatment effects. After treatment administration on days 7 and 9, the DSS group continued to decline and reached 80% of the initial weight by day 10, free BH showed only partial recovery to 93-95%, and MCR provided minimal benefit with body weight around 85%, whereas MCR-BH manifested a clear rebound and recovered to 110% by day 11.

Disease activity index (DAI) trajectories reflected clinical onset, peak severity, and recovery of DSS colitis (Figure 4.11C). During DSS induction (day 0–7), the average DAI increased similarly across all DSS-exposed groups from 0 to a peak at day 8, with minor deviations attributable to individual variability rather than treatment effects. After treatment on days 7 and 9, group differences were evident at the peak disease stage and at the endpoint. On day 8, DAI was 7.6 in DSS, 6.0 in MCR and free BH, and 4.4 in MCR-BH. By day 11, DAI remained 4.8 in DSS and 4.4 in MCR but decreased to 2.8 with free BH and to 0.6 with MCR-BH. The overall decline in DAI after the peak is consistent with symptom relief following DSS withdrawal, whereas the between-group differences reflect additional therapeutic effects. In particular, MCR-BH accelerated clinical recovery beyond DSS cessation alone, while MCR showed only minimal improvement relative to DSS. Macroscopic assessment of colon morphology further supported these trends (Figure 4.11D,E). DSS exposure produced marked colon shortening and wall thickening relative to healthy controls. MCR did not improve this phenotype, whereas free BH provided partial restoration. In contrast, colons from the MCR-BH group appeared longer and less edematous, resembling control tissue. Colon-length quantification yielded 105.9 ± 3.6 mm for Control, 62.0 ± 5.8 mm for DSS, 66.4 ± 7.6 mm for MCR, 78.2 ± 10.0 mm for free BH, and 97.0 ± 4.2 mm for MCR-BH.

Histological analysis provided microscopic evidence of mucosal protection (Figure 4.12). Control slides displayed an intact epithelium, well-organized crypts, and minimal inflammatory infiltration, whereas DSS challenge caused epithelial erosion, crypt loss, ulceration, and dense inflammatory cell infiltration. MCR showed similar lesions, and free BH produced partial improvement with focal crypt regeneration but persistent inflammation. Colons from the MCR-BH group preserved epithelial continuity, exhibited more regular crypt architecture, and showed reduced inflammatory infiltrates, approaching near-normal tissue organization. Taken together, the improvements in body weight, DAI, colon morphology, and histological integrity indicate that bacteria-loaded MCRs mitigated DSS-induced colitis more effectively than free probiotics or material controls. This conclusion is based on an acute DSS mouse model, and durability and dose calibration should be evaluated in chronic and more clinically relevant settings.

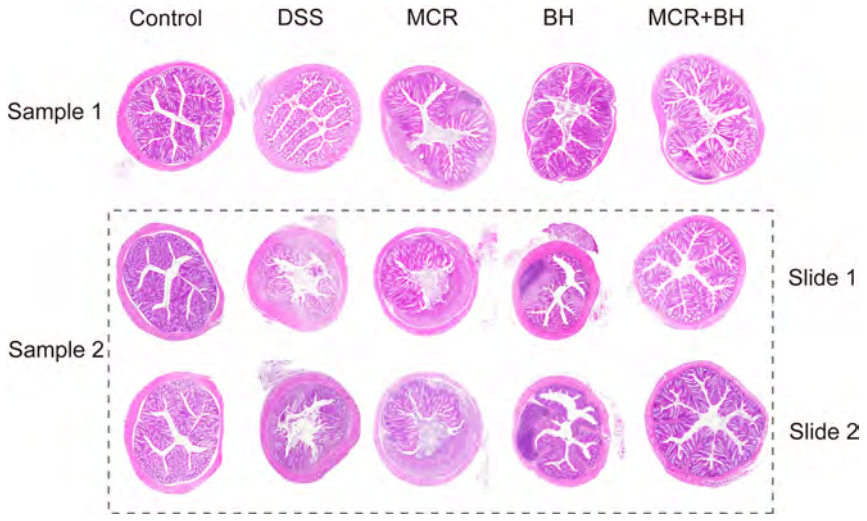


Figure 4.12: Representative H&E-stained distal colon sections, illustrating severe epithelial damage and inflammatory infiltration in DSS and MCR groups, partial improvement with BH, and substantial restoration of mucosal architecture in the MCR-BH group.

### 4.2.5 Gut Microbiota Restoration Mechanism of MCRs on UC

To examine whether probiotic-loaded magnetic carrier robots (MCR-BH) corrected DSS-induced dysbiosis, 16S rRNA gene sequencing was performed on colonic contents (Figure 4.13). Family-level profiles (Figure 4.13A) show that DSS shifted the community away from the healthy pattern, and MCR remained similar to DSS, indicating limited microbiota modulation by the carrier matrix alone. Free BH induced only modest remodeling at the family level and largely overlapped with the DSS-like pattern, while MCR-BH more consistently shifted the distribution toward a control-like composition. A Venn diagram of shared and unique feature sequences (Figure 4.13B) further summarized overlap across groups. DSS and MCR shared a large set of feature sequences, consistent with a common dysbiotic community structure, whereas MCR-BH showed greater overlap with the healthy control group and a reduced intersection with DSS-associated features, supporting a shift toward a healthier community composition.

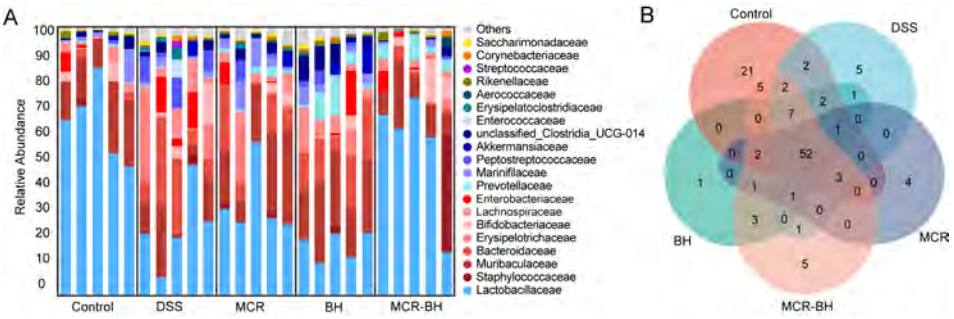


Figure 4.13: (A) Family-level relative abundance profiles of fecal microbiota in Control, DSS, MCR, free bacteria hydrogel (BH), and bacteria-loaded MCRs (MCR-BH) groups. (B) Venn diagram showing shared and unique feature sequences among the five groups.



Alpha-diversity analyses indicated that DSS significantly reduced richness and evenness relative to Control, as reflected by operational taxonomic units (OTUs) and Shannon index (Figure 4.14A,B). MCR and free BH were not significantly different from DSS in observed OTUs and Shannon index, suggesting limited recovery of overall diversity. In contrast, MCR-BH significantly increased observed OTUs relative to DSS and relative to free BH, and also significantly increased Shannon index relative to DSS, MCR, and free BH. Chao1 richness was significantly reduced in DSS compared with Control (Figure 4.14C), and Chao1 increased significantly in MCR, free BH, and MCR-BH relative to DSS; however, only MCR-BH showed a consistent, significant recovery across richness and evenness metrics. Beta-diversity analysis (Figure 4.14D) revealed that DSS and MCR clustering closely, indicating that MCR alone did not substantially alter the DSS-associated community structure.

In contrast, MCR-BH shifts the microbiota composition toward the Control cluster, suggesting an overall mitigation of DSS-driven dysbiosis. Consistent with broader community-level restoration, family-level analysis showed a significant DSS-associated reduction in *Lactobacillaceae* which is significantly restored by MCR-BH. Importantly, this increase is also significant versus free BH, whereas free BH does not produce a significant improvement over DSS based on the annotated statistics (Figure 4.15A). *Bifidobacteriaceae* exhibits modest between-group differences in relative abundance, but these variations are not statistically significant.

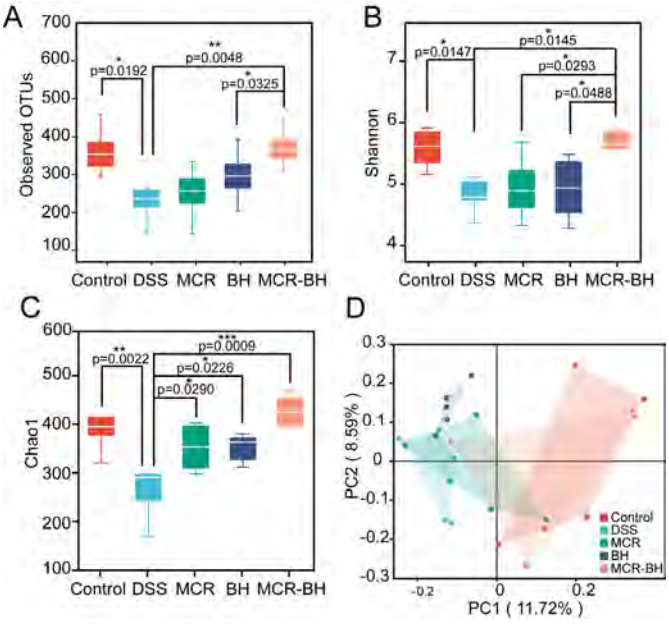


Figure 4.14: (A-C) Alpha-diversity indices, including operational taxonomic units (OTUs) (A), Shannon index (B), and Chao1 richness estimator (C), demonstrating DSS-induced loss of diversity and its partial rescue by BH and more pronounced restoration by MCR-BH. (D) Principal coordinates analysis (PCoA) based on Bray-Curtis distances, illustrating distinct clustering of DSS and MCR, intermediate positioning of BH, and a shift of MCR-BH toward the Control microbiota.

This result suggests that DSS induction and *Bifidobacteriaceae* administration did not directly alter the overall abundance of this family in the gut (Figure 4.15B). However, changes at co-abundance groups (CAGs) level remain possible and warrant further investigation in future studies. *Bacteroidaceae* is significantly elevated in DSS group compared with Control, while MCR-BH significantly reduced its abundance relative to both DSS and free BH (Figure 4.15C).

An increased *Bacteroidaceae* level is commonly associated with colitis-associated dysbiosis and can reflect an over representation of inflammation-adapted taxa that may exacerbate mucosal inflammation and barrier disruption. The hierarchical clustering heatmap of the top 40 bacterial families (Figure 4.16) indicates an overall disruption of community structure after DSS induction. Samples in DSS and MCR groups show more hetero-

geneous and irregular abundance patterns across these dominant families, suggesting potential microbiota dysbiosis. In contrast, the MCR-BH group shows a community profile that is more similar to the healthy control group at the family level, consistent with a partial restoration of community structure.

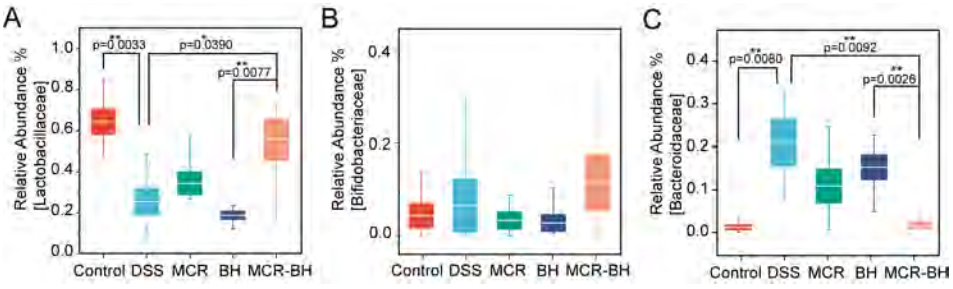


Figure 4.15: Relative abundance of selected health-associated and dysbiosis-associated bacterial families: (A) *Lactobacillaceae*, (B) *Bifidobacteriaceae*, and (C) inflammation-related taxa: *Bacteroidaceae*), highlighting enrichment of beneficial families and suppression of harmful ones in the MCR-BH group.

Taken together, DSS induction drives a pronounced loss of community richness and evenness and reshapes the family-level structure toward dysbiosis configuration. Across the analysis, the MCR alone shows limited microbiota modulation because MCR tracks the DSS state in both beta-diversity and dominant-family distributions. Free BH induces only modest remodeling and does not consistently separate from the DSS-associated profile. In contrast, MCR-BH produces a coherent, multi-level restoration signal. It increases alpha diversity across richness and evenness metrics, shifts overall composition toward the control cluster in beta-diversity space, and partially re-organizes the dominant-family heatmap toward the Control group pattern. These results support that magnet-localized delivery strengthens the functional impact of probiotics beyond free hydrogel administration by enhancing target-site exposure and retention, thereby enabling a more robust shift toward a healthier microbial community.

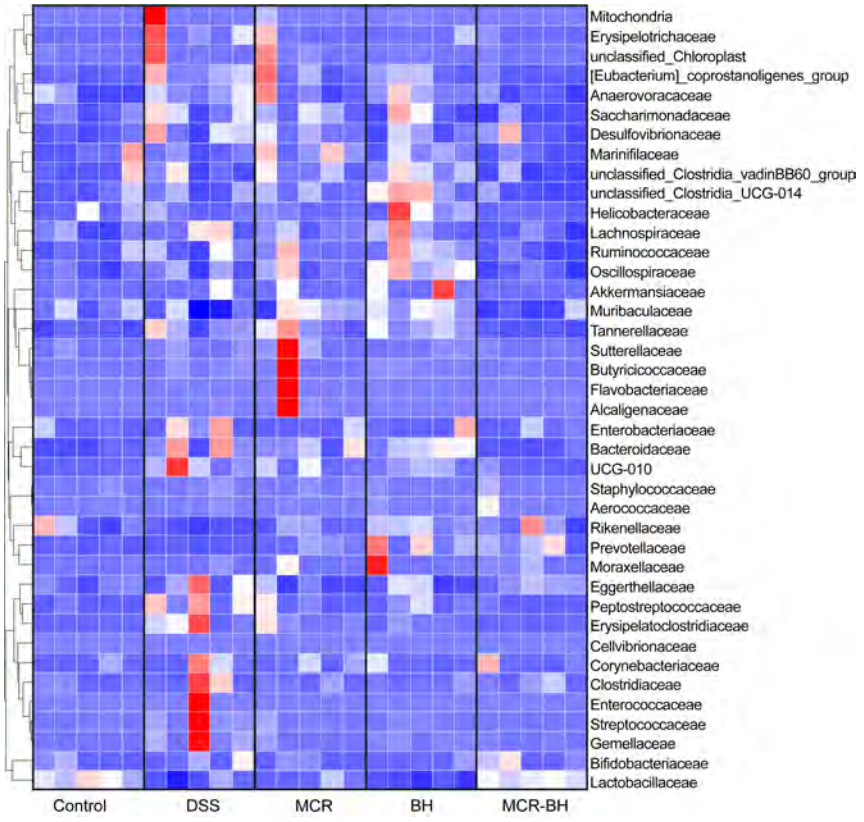


Figure 4.16: Heatmap with hierarchical clustering of dominant bacterial families across all samples, showing that the overall community structure in MCR-BH mice closely resembles that of healthy controls and is distinct from DSS and MCR groups.

## 4.3 Conclusion

In this study, we developed a programmable magnetic carrier robot platform for targeted probiotic delivery in the treatment of ulcerative colitis. This platform aims to address two key limitations of conventional probiotic administration: insufficient site specificity and limited intestinal retention. The MCRs are fabricated via a two-step screen-printing process that integrates a programmed NdFeB/PDMS elastomer for wireless magnetic actuation. A bacteria-loaded hydrogel layer is integrated to serve as both a protective matrix and a localized-release carrier.

Functionally, the MCRs demonstrate wireless navigation and site-specific retention under real-time visualization in colon-mimicking tracks and a colon phantom, supporting their potential in clinical operation. Moreover, the platform offers practical deployment routes across anatomical scales: rectal placement is suited for large lumens such as the human colon, while in small-animal models, where robotic-arm positioning accuracy can be constrained by organ-scale dimensions, externally affixed permanent magnets provide a simple and effective means to enhance local magnetic trapping and extend retention. In further *in vivo* validation, a DSS-induced acute colitis mouse model is established, in which magnet-localized delivery of probiotic-loaded MCRs yields superior therapeutic outcomes compared with free probiotic hydrogel and material controls, demonstrating site-specific intervention and intestinal retention. Importantly, 16S rRNA analysis further demonstrated that localized delivery more effectively restored gut microbial balance than non-localized probiotic administration, with improved microbial diversity and beneficial changes in observed bacterial taxa.



In summary, these results position the magnetic carrier robots as a controllable strategy for active and site-specific microbial colonization, and motivate broader translation of soft robotic systems for precision intervention in gastrointestinal disease. In the present study, (i) performance is validated mainly in an acute DSS colitis model with short-term follow-up, so durability and long-term safety in chronic, clinically relevant settings remain to be established; (ii) dose calibration is at a proof-of-concept stage, with therapeutic selection and per-robot loading/release requiring further standardization; and (iii) *in vivo* operation relies largely on open-loop magnetic actuation, while the feedback mechanism and closed-loop targeting remain to be developed. As noted by the current design, future work should evaluate durability, dose calibration, and long-term safety in chronic and more clinically relevant models and further explore translation-oriented delivery routes (e.g., rectal deployment in large lumens) and closed-loop targeting strategies.

## 4.4 Materials and Methods

### 4.4.1 Ink Preparation

Magnetic ink Preparation: To prepare the magnetic ink, we utilized a composite system consisting of magnetic particles and elastomers. Magnetic particles (NdFeB, MQFPTM-16-7) were selected due to their high magnetic remanence. Before mixing, all the PrFeB particles were magnetized beyond saturation using an impulse magnetizer (IM-10-30, ASC SCIENTIFIC, USA). The elastomer matrix, PDMS (), was prepared by mixing silicone resin and curing agent at a 1:1 weight ratio. The NdFeB particles were gradually added to the matrix at a 1:1 weight ratio, and the entire formulation was blended by an overhead stirrer (NANOSTAR, IKA, Germany) at $\tilde{2}000$ r.p.m. for 2 minutes to ensure homogeneity. The final mixture was degassed for 5 minutes in a vacuum chamber to eliminate air bubbles.



Alginate hydrogel Preparation: Sodium alginate was dissolved in sterile PBS (pH 7.4) to obtain a 2.0 wt% solution and stirred until fully hydrated overnight. The alginate solution was then degassed to remove trapped air and stored at 4 °C for subsequent use. A $CaCl_2$ crosslinking solution was prepared in advance (in PBS).

For the bacteria-loaded hydrogel (BH), probiotic lyophilized powder was directly added into the prepared alginate solution and mixed thoroughly to obtain a homogeneous bacteria–alginate precursor. The resulting mixture was immediately printed onto the pre-fabricated MCR substrates to form the BH layer. Crosslinking was initiated by spraying a thin layer of $CaCl_2$ solution onto the hydrogel surface, allowing rapid fixation of the printed pattern via ionic gelation. After gelation, samples were gently rinsed with sterile PBS to remove excess $Ca^{2+}$ and were kept in sterile PBS at 4 °C before use.

### 4.4.2 Screen-Printing Procedures

The magnetic soft robots were fabricated using a layer-by-layer screen-printing technique. A piece of 120 mesh nylon net with a laser-cut screen was tense and mounted onto a 3D-printed frame (Figure S1). Each layer of magnetic ink was deposited by sweeping a polyurethane squeegee at an angle of around 70° and a manually controlled pressure. The substrates,

including elastomer films, paper, glass, and wood, were secured onto the printing stage. After printing each layer, the ink was cured at 80°C for 10 minutes on a heating platform. For multi-layered devices, additional layers were printed following the same procedure.

### 4.4.3 Rheological Test

The rheological properties of the magnetic ink were measured using a rotational rheometer (Anton Paar MCR 302). The ink was loaded onto the parallel plate fixture with a 25 mm diameter at a 1 mm gap. A shear rate sweep was performed from $0.01s^{-1}$ to $0.01s^{-1}$ at room temperature to determine the ink's viscosity profile and shear-thinning behavior, crucial for the screen-printing process. Additionally, oscillatory tests were conducted to measure the storage modulus (G') and loss modulus (G") at a constant frequency of 1 Hz, providing insights into the viscoelasticity properties of the ink.



### 4.4.4 SEM Characterization

Scanning electron microscopy (SEM, Thermo Fisher Apreo S, USA) was used to examine the morphologies and mesoscopic structures of the printed film. The sample was spread flat and securely affixed to the test bench before SEM characterization and analyzed at an accelerating voltage of 10 kV. This characterization allowed us to observe the printing quality and dispersion of the magnetic particles in the elastomer matrix.

### 4.4.5 Material mechanical characterization

The tensile tests are conducted using a texture analyzer (CT3, AMETEK GmbH B.U. Brookfield). Standardized testing samples made of PDMS/NdFeB composites and alginate hydrogels are subjected to axis tensile tests as per ASTM standard tests. The loading speed for the tests is set to 1 mm/s, and the testing range is set to 25% strain.

### 4.4.6 Animal Experiment

Ethics statement: All animal experiments conformed to the guidelines for the care and use of laboratory animals and were approved by the Committee of Laboratory Animal Experimentation at Southwest University of

Science and Technology (Mianyang, China).Neither the laboratory mice nor the study conflicted with the ethical guidelines, religious beliefs, or legal requirements of China.

Model creating: 25 male Kunming mice (6-8 weeks) were acclimated for 7 days before experiments. To establish a DSS-induced acute colitis model, mice were provided with drinking water containing 3 wt% DSS starting on day 0. From day 0 onward, body weight and clinical signs were recorded daily, and a disease activity index (DAI) was calculated. To avoid excessive disease severity and mortality, DSS administration in individual mice was discontinued immediately once the DAI reached $\geq 4$, and colitis induction at this threshold was considered successful. If a mouse did not reach DAI $\geq 4$ by day 7 after DSS initiation, it was classified as a modeling failure and excluded from subsequent treatment and analysis. Only successfully modeled mice were used for further interventions.



*In vivo* experimental verification: Successfully modeled animals were then allocated into four groups: DSS only, MCR, free bacteria hydrogel (BH), and bacteria-loaded MCRs (MCR-BH). Treatments were administered by oral gavage on days 7 and 9 after the start of DSS administration. During MCR administration, a NdFeB permanent magnet was placed on the abdomen to localize the robots in the distal colon, as confirmed by X-ray scanning and CT (Figure **??**b and Figure S12). Throughout the treatment period, body weight and clinical scores were continuously monitored. On day 11, all mice were sacrificed; the colon was harvested, and distal colon tissues were collected and fixed for histological analysis, including hematoxylin and eosin (H&E) staining (Figure S13).

### 4.4.7 Histological Assessment

On day 11 of the experiment, the mice were sacrificed for collecting colon samples. After washing with PBS, 1 cm of the distal section of colons was fixed in 4% paraformaldehyde fixation and then embedded in paraffin. After cutting into round slices, the thin tissue sections were stained with H&E.

### 4.4.8 Gut microbiota 16s sequencing assay

After different treatments, fecal pellets were collected from mice, snap-frozen in liquid nitrogen, and sent to Novogene, Inc. for gut microbiota

profiling by 16S rRNA gene sequencing. The 16S V3–V4 region was amplified using barcoded primers CCTAYGGGRBGCASCAG (forward) and GGACTACNNGGGTATCTAAT (reverse). PCR was carried out with 15 $\mu$L Phusion High-Fidelity PCR Master Mix, 0.2 $\mu$M of each primer, and $\leq$ 10 ng template DNA, under the following cycling conditions: 98 °C for 1 min; 30 cycles of 98 °C for 10 s, 50 °C for 30 s, and 72 °C for 30 s; and a final extension at 72 °C for 5 min. PCR products were purified using magnetic bead purification, pooled at equi-density ratios, and sequencing libraries were generated with index addition. Libraries were quantified by Qubit and real-time PCR, assessed by bioanalyzer for size distribution, and sequenced on a NovaSeq 6000 or DNBSEQ-G99 platform according to the required data output.

16S rRNA gene sequencing analysis was conducted using the Novogene bioinformatics pipeline. Paired-end reads were assigned to samples by unique barcodes and trimmed to remove barcode and primer sequences. Reads were merged using FLASH (v1.2.11) to generate raw tags, followed by quality filtering using fastp (v0.23.1) to obtain clean tags. Chimera detection was performed against the SILVA reference database, and chimeric sequences were removed using vsearch (v2.16.0) to generate effective tags. Effective tags were denoised in QIIME2 using DADA2 (default; deblur optional) to infer ASVs, and taxonomic annotation was performed in QIIME2 using the SILVA database. ASV absolute abundances were normalized to the sequencing depth of the sample with the fewest reads, and downstream alpha diversity and beta diversity analyses were performed based on the normalized dataset.

# 5

# Conclusions

This thesis investigates magnetic soft robots for localized therapy by advancing programmable magnetization, scalable fabrication, and robust multi-material integration. It introduces a three-dimensional magnetization programming strategy with a scalable fabrication and integration process, enabling controllable deformation, navigation, and positioning for localized therapeutic delivery. The conclusions are presented in three parts, progressing from magnetization programming to scalable fabrication and *in vivo* therapeutic validation. First, a fluidic control programming technique is developed to achieve precise three-dimensional magnetization in magnetic soft metamaterials. By decoupling magnetization assignment from structural fabrication, complex architectures can be fabricated with spatially defined magnetic orientations. Second, a multi-layer screen-printing platform is established to integrate magnetic composites with functional materials across a broad range of substrate types. By overlapping patterned magnetic soft materials with additional functional layers, this approach expands the accessible device formats and lowers practical constraints on fabrication and integration. Third, a bio-hybrid magnetic soft robot for microbial therapy in ulcerative colitis is developed based on the magnetization and fabrication capabilities established in the preceding chapters. The screen-printed magnetic carrier robots demonstrate controlled navigation, positioning, and targeted microbial delivery in the intestinal environment. The specific conclusions of this thesis and the outlook for future research are discussed in the following sections.

## 5.1 Three-dimensional magnetization programming based on fluidic control

Three-dimensional magnetization programming is established here as a scalable capability that is decoupled from structural fabrication. The key outcome is spatially addressable magnetic encoding within monolithic voxelated architectures, which enables prescribed deformation behaviors without relying on assembly-based approaches. The technique is implemented in voxelated lattice architectures through a sequential process of selective fluid injection, field-assisted particle alignment, and stepwise curing. In this workflow, prescribed voxel groups are filled and magnetized in defined orientations, and the sequence is repeated to embed multiple magnetization directions within a single continuous lattice while preserving structural integrity. By programming magnetization locally rather than globally, the method enables spatially heterogeneous magnetic encoding without the need for post-assembly alignment or constraints imposed by printing paths. This overcomes limitations of approaches that rely on two-dimensional patterning, pre-magnetized component assembly, or uniform field exposure.

This programmable magnetic architecture enables reconfigurable mechanical responses, including state switching under the same structural geometry. In particular, magnetic-field-guided elastic buckling is employed as a controlled instability mechanism to amplify deformation and switch between distinct structural states. By reversing the field direction, the lattice transitions rapidly between positive and negative Poisson's ratio modes, demonstrating multi-mode and reversible mechanical behavior. These results establish a framework for designing reliable and programmable deformation in magnetic soft metamaterials and provide the mechanical foundation for subsequent advances in scalable fabrication and multi-material integration.

## 5.2 Scalable fabrication and multi-material integration based on multi-layer screen-printing

Building on spatially programmable magnetization, multi-layer screen printing provides a manufacturable route for combining magnetic actuation with

functional materials and diverse substrates. Patterned magnetic regions and additional functional layers can be integrated within a single fabrication sequence while preserving programmable deformation after integration. The platform is implemented through a controlled sequence of layer-by-layer screen-printing and curing steps. Patterned magnetic regions are deposited at locations where actuation is required, and additional layers are subsequently printed to introduce functions such as conductive traces, circuit elements, or optical additives. Magnetization is incorporated into the fabrication workflow so that programmed deformation is retained after integration, without relying on post-fabrication assembly of separately prepared components.

The versatility of this strategy is demonstrated through a series of functional devices across multiple contexts. Foldable magnetic actuators are printed on paper, fabric, glass, and ITO films, each exhibiting reliable folding under a uniform magnetic field. A wireless pH-sensing device is realized, enabling simultaneous testing of two samples through wireless actuation. Three-dimensional shape-morphing structures are also demonstrated, including biomimetic mimosa leaves, origami-inspired cubic transformations, and undulating ring actuators with directionally programmed elements. In addition, magnetic soft gripper robots and flexible electronic devices with integrated actuation and circuitry demonstrate that mechanical deformation and device-level functions can be produced within a unified printing and programming process.



## 5.3 Bio-hybrid magnetic soft robots for *in vivo* intestinal disease therapy

The previous section establishes a practical foundation for the bio-hybrid therapeutic systems. These magnetization and fabrication capabilities are then translated into a bio-hybrid magnetic carrier designed for localized microbial therapy in the gastrointestinal tract. By coupling a programmed magnetic actuation layer with a probiotic-loaded hydrogel layer, the system enables controlled navigation, positioning, and site-specific delivery under intestinal operating constraints.

The study addresses practical constraints associated with bio-hybrid integration in gastrointestinal applications, including interfacial reliabil-

ity between hydrophobic elastomers and hydrophilic hydrogels, mechanical compatibility across layers, stability in aqueous and chemically dynamic conditions, and controllable retention within gastrointestinal geometries. The magnetic carrier is systematically evaluated for field-driven locomotion and controlled positioning across multiple surface morphologies, including colon-mimicking tracks with varied geometries and a colon phantom under visual guidance. *In vivo* experiments in a DSS-induced colitis mouse model demonstrate that magnet-localized probiotic delivery significantly enhances microbial balance restoration and therapeutic recovery compared with non-localized administration.

## 5.4 Outlook

Future progress toward magnetic soft robots for localized therapy will be determined by how effectively magnetization programming and multi-material integration can be translated into clinically usable systems. Beyond demonstrating wireless deformation, localized therapy requires predictable behavior from programmed magnetization, stable integration of functional payload materials, and deployment under clinical constraints such as imaging, sterilization, and therapeutic efficacy. Building on the contributions of this thesis, three priorities are identified.

### 5.4.1 From magnetization programming to therapy-oriented closed-loop control

Magnetization programming provides a powerful handle for shaping deformation, locomotion, and anchoring, but localized therapy demands that these behaviors can be specified and achieved reliably at a target site. A next step is to move from forward prediction to inverse design pipelines that map therapy-relevant objectives, including trajectory, positioning accuracy, anchoring state, and local contact force, to feasible magnetization distributions and fabrication instructions. Voxel-based programming offers a structured representation to connect magneto-mechanical models with practical programmability.

Closed-loop control will be essential once devices operate in patient-like anatomy where uncertainty arises from lumen geometry, mucus variability, and peristaltic disturbances. For localized therapy, the control problem is

not only to move, but to maintain position and deliver payload at a prescribed site for a prescribed duration. Imaging and tracking are therefore part of the control design. Future systems should be developed with explicit compatibility with endoscopic visualization and clinically available tracking, and should define measurable control targets such as positioning error under imaging, anchoring reliability under flow, and repeatability of site-specific delivery.

### 5.4.2 Multi-material integration under sterilization, biocompatibility, and payload performance constraints

For localized therapy, multi-material integration is not an optional feature but the core enabler for combining actuation with payload protection and release. Future work should prioritize interface robustness between magnetic elastomers and therapeutic layers such as hydrogels, and should quantify how mechanical mismatch, swelling, and cyclic deformation affect long-term integrity and function. In gastrointestinal settings, stability must be demonstrated under wet, chemically variable, and mechanically abrasive conditions, with clear failure-mode analysis that includes delamination, fragmentation risk, and changes in frictional behavior that alter control performance.

Sterilization and biocompatibility must be incorporated because they can directly alter magnetic response, polymer mechanics, and hydrogel payload viability. Future studies should benchmark realistic sterilization routes and storage conditions, and evaluate their effects on magnetization stability, actuation repeatability, and payload efficacy. For microbial therapies in particular, the key question is whether integration strategies preserve viability and enable localized colonization, rather than only transporting a payload through the GI tract.

### 5.4.3 Clinical workflow integration and optimization with existing therapeutic procedures

Successful translation of magnetic soft robots for localized therapy requires coordinated integration with established clinical workflows. Rather than treating the robotic system as an auxiliary device, deployment strategies, imaging guidance, and intervention procedures must be co-designed to ensure compatibility and safety. The introduction of wireless magnetic actua-

tion modifies how navigation, localization, and intervention are performed, and therefore requires reassessment of imaging modalities and access approaches.

For gastrointestinal applications, integration with colonoscopy platforms requires compatibility between the magnetic actuation platform (external coil arrays or permanent magnets) and the available space and magnetic interactions with surrounding instruments. Imaging strategies may include endoscopic visualization, fluoroscopy, ultrasound guidance, or magnetic resonance imaging, each imposing distinct constraints on allowable magnetic field strength, device materials, and the placement of coils or magnets. For example, ultrasound guidance requires sufficient visibility of the device in ultrasound images and coil or magnet placement that does not obstruct the probe or reduce image quality.

Clinical translation requires a clearly defined procedural chain, including device preparation, insertion, magnetic localization, retention, payload release, and retrieval. Particular attention should be given to potential magnetic coupling with metallic tools, implanted devices, or operating-room equipment, as well as to ergonomic integration of actuation hardware into clinical spaces. Establishing procedure-specific compatibility criteria and safety thresholds will be essential for translating magnetic soft robots into routine localized diagnostic and therapeutic practice.

# Bibliography

[1] L. Wang and F. Iida, "Deformation in Soft-Matter Robotics: A Categorization and Quantitative Characterization," *IEEE Robotics and Automation Magazine*, vol. 22, no. 3, pp. 125–139, 9 2015.

[2] C. Laschi, B. Mazzolai, and M. Cianchetti, "Soft robotics: Technologies and systems pushing the boundaries of robot abilities," *Science Robotics*, vol. 1, no. 1, 12 2016.

[3] L. C. van Laake, J. de Vries, S. M. Kani, and J. T. Overvelde, "A fluidic relaxation oscillator for reprogrammable sequential actuation in soft robots," *Matter*, vol. 5, pp. 2898–2917, 9 2022.

[4] M. Wehner, R. L. Truby, D. J. Fitzgerald, B. Mosadegh, G. M. Whitesides, J. A. Lewis, and R. J. Wood, "An integrated design and fabrication strategy for entirely soft, autonomous robots," *Nature 2016 536:7617*, vol. 536, pp. 451–455, 8 2016.

[5] J. D. Carrico, K. J. Kim, and K. K. Leang, "3d-printed ionic polymer-metal composite soft crawling robot," *Proceedings - IEEE International Conference on Robotics and Automation*, pp. 4313–4320, 7 2017.

[6] A. Gao, N. Liu, M. Shen, M. E. Abdelaziz, B. Temelkuran, and G. Z. Yang, "Laser-profiled continuum robot with integrated tension sensing for simultaneous shape and tip force estimation," *Soft Robotics*, vol. 7, pp. 421–443, 8 2020.

[7] M. Kaynak, P. Dirix, and M. S. Sakar, "Addressable acoustic actuation of 3d printed soft robotic microsystems," *Advanced Science*, vol. 7, pp. 2001120, 10 2020.

[8] O. M. Wani, H. Zeng, and A. Priimagi, "A light-driven artificial flytrap," *Nature Communications 2017 8:1*, vol. 8, pp. 15 546–, 5 2017.

[9] M. Amjadi and M. Sitti, "High-performance multiresponsive paper actuators," *ACS Nano*, vol. 10, pp. 10 202–10 210, 11 2016.

[10] Z. Wang, S. Misra, and V. K. Venkiteswaran, "Multi-layer screen-printing of magnetic soft robots with integrated materials and functions," *Cell Reports Physical Science*, vol. 0, no. 0, pp. 102614, 6 2025.

[11] V. K. Venkiteswaran, D. K. Tan, and S. Misra, "Tandem actuation of legged locomotion and grasping manipulation in soft robots using magnetic fields," *Extreme Mechanics Letters*, vol. 41, pp. 101023, 2020.

[12] Y. Dong, L. Wang, N. Xia, Z. Yang, C. Zhang, C. Pan, D. Jin, J. Zhang, C. Majidi, and L. Zhang, "Untethered small-scale magnetic soft robot with programmable magnetization and integrated multifunctional modules," *Science Advances*, vol. 8, no. 25, pp. 8932, 6 2022.

[13] J. Zhang, Z. Ren, W. Hu, R. H. Soon, I. C. Yasa, Z. Liu, and M. Sitti, "Voxelated three-dimensional miniature magnetic soft machines via multimaterial heterogeneous assembly," *Science Robotics*, vol. 6, no. 53, pp. 112, 4 2021.

[14] G. Bertotti, "Hysteresis in magnetism: For physicists, materials scientists, and engineers," pp. 558, 1998.

[15] W. Gao, D. Kagan, O. S. Pak, C. Clawson, S. Campuzano, E. Chuluun-Erdene, E. Shipton, E. E. Fullerton, L. Zhang, E. Lauga, and J. Wang, "Cargo-towing fuel-free magnetic nanoswimmers for targeted drug delivery," *Small*, vol. 8, pp. 460–467, 2 2012.

[16] A. Zhu, J. Zhao, and L. Yang, "Multimodal magnetic miniature robot for adaptive navigation in amphibious environments," *npj Robotics 2025 3:1*, vol. 3, pp. 42–, 12 2025.

[17] J. Tang, C. Yao, Z. Gu, S. Jung, D. Luo, and D. Yang, "Super-soft and super-elastic dna robot with magnetically driven navigational locomotion for cell delivery in confined space," *Angewandte Chemie - International Edition*, vol. 59, pp. 2490–2495, 2 2020.

[18] E. Gultepe, S. Yamanaka, K. E. Laflin, S. Kadam, Y. Shim, A. V. Olaru, B. Limketkai, M. A. Khashab, A. N. Kalloo, D. H. Gracias, and F. M. Selaru, "Biologic tissue sampling with untethered microgrippers," *Gastroenterology*, vol. 144, pp. 691–693, 4 2013.

[19] C. Heunis, Z. Wang, G. de Vente, S. Misra, and V. Venkiteswaran, "A Magnetic Bio-Inspired Soft Carrier as a Temperature-Controlled Gastrointestinal Drug Delivery System," *Macromolecular Bioscience*, vol. 23, no. 7, 2023.

[20] C. Wang, V. R. Puranam, S. Misra, and V. K. Venkiteswaran, "A snake-inspired multi-segmented magnetic soft robot towards medical applications," *IEEE Robotics and Automation Letters*, vol. 7, pp. 5795–5802, 4 2022.

[21] H. Zhang, J. Wu, D. Fang, and Y. Zhang, "Hierarchical mechanical metamaterials built with scalable tristable elements for ternary logic operation and amplitude modulation," *Science Advances*, vol. 7, no. 9, pp. eabf1966, 2021.

[22] S. Macrae Montgomery, S. Wu, X. Kuang, C. D. Armstrong, C. Zemelka, Q. Ze, R. Zhang, R. Zhao, and H. Jerry Qi, "Magneto-Mechanical Metamaterials with Widely Tunable Mechanical Properties and Acoustic Bandgaps," *Advanced Functional Materials*, vol. 31, no. 3, pp. 2005319, 1 2021.

[23] M. Kadic, G. W. Milton, M. van Hecke, and M. Wegener, "3D metamaterials," *Nature Reviews Physics*, vol. 1, no. 3, pp. 198–210, 3 2019.

[24] R. Lakes, "Foam Structures with a Negative Poisson's Ratio," *Science*, vol. 235, no. 4792, pp. 1038–1040, 1987.

[25] S. Babaee, J. Shim, J. C. Weaver, E. R. Chen, N. Patel, and K. Bertoldi, "3D Soft Metamaterials with Negative Poisson's Ratio," *Advanced Materials*, vol. 25, no. 36, pp. 5044–5049, 2013.

[26] K. Bertoldi, P. M. Reis, S. Willshaw, and T. Mullin, "Negative Poisson's Ratio Behavior Induced by an Elastic Instability," *Advanced Materials*, vol. 22, no. 3, pp. 361–366, 2010.

[27] X. Shi, Y. Zhu, X. Fan, H. A. Wu, P. Wu, X. Ji, Y. Chen, and J. Liang, "An auxetic cellular structure as a universal design for enhanced piezoresistive sensitivity," *Matter*, vol. 5, no. 5, pp. 1547–1562, 5 2022.

[28] T. A. M. Hewage, K. L. Alderson, A. Alderson, and F. Scarpa, "Double-Negative Mechanical Metamaterials Displaying Simultaneous Negative Stiffness and Negative Poisson's Ratio Properties," *Advanced Materials*, vol. 28, no. 46, pp. 10 323–10 332, 2016.

[29] D. M. Correa, T. Klatt, S. Cortes, M. Haberman, D. Kovar, and C. Seepersad, "Negative stiffness honeycombs for recoverable shock isolation," *Rapid Prototyping Journal*, vol. 21, no. 2, pp. 193–200, 3 2015.

[30] L. Wu, B. Li, and J. Zhou, "Isotropic Negative Thermal Expansion Metamaterials," *ACS Applied Materials and Interfaces*, vol. 8, no. 27, pp. 17 721–17 727, 7 2016.

[31] J. Qu, M. Kadic, A. Naber, and M. Wegener, "Micro-Structured Two-Component 3D Metamaterials with Negative Thermal-Expansion Coefficient from Positive Constituents," *Scientific Reports 2017 7:1*, vol. 7, no. 1, pp. 1–8, 1 2017.

[32] X. Xu, Q. Zhang, M. Hao, Y. Hu, Z. Lin, L. Peng, T. Wang, X. Ren, C. Wang, Z. Zhao, C. Wan, H. Fei, L. Wang, J. Zhu, H. Sun, W. Chen, T. Du, B. Deng, G. J. Cheng, I. Shakir, C. Dames, T. S. Fisher, X. Zhang, H. Li, Y. Huang, and X. Duan, "Double-negative-index ceramic aerogels for thermal superinsulation," *Science*, vol. 363, no. 6428, pp. 723–727, 2 2019.

[33] T. Frenzel, M. Kadic, and M. Wegener, "Three-dimensional mechanical metamaterials with a twist," *Science*, vol. 358, no. 6366, pp. 1072–1074, 2017.

[34] X. Xin, L. Liu, Y. Liu, and J. Leng, "4D Printing Auxetic Metamaterials with Tunable, Programmable, and Reconfigurable Mechanical Properties," *Advanced Functional Materials*, vol. 30, no. 43, pp. 2004226, 10 2020.

[35] Z. Ren, L. Ji, R. Tao, M. Chen, Z. Wan, Z. Zhao, and D. Fang, "SMP-based multi-stable mechanical metamaterials: From bandgap tuning to wave logic gates," *Extreme Mechanics Letters*, vol. 42, pp. 101077, 1 2021.

[36] C. Yang, M. Boorugu, A. Dopp, J. Ren, R. Martin, D. Han, W. Choi, and H. Lee, "4D printing reconfigurable, deployable and mechanically tunable metamaterials," *Materials Horizons*, vol. 6, no. 6, pp. 1244–1250, 7 2019.

[37] A. Tariq, Z. U. Arif, M. Y. Khalid, M. Hossain, P. I. Rasool, R. Umer, and S. Ramakrishna, "Recent Advances in the Additive Manufacturing of Stimuli-Responsive Soft Polymers," *Advanced Engineering Materials*, vol. 25, no. 21, pp. 2301074, 11 2023.

[38] Z. U. Arif, M. Y. Khalid, A. Tariq, M. Hossain, and R. Umer, "3D printing of stimuli-responsive hydrogel materials: Literature review and emerging applications," *Giant*, vol. 17, pp. 100209, 3 2024.

[39] B. Zou, Z. Liang, D. Zhong, Z. Cui, K. Xiao, S. Shao, and J. Ju, "Magneto-thermomechanically reprogrammable mechanical metamaterials," *Advanced Materials*, 2022.

[40] H. Gu, Q. Boehler, D. Ahmed, and B. J. Nelson, "Magnetic quadrupole assemblies with arbitrary shapes and magnetizations," *Science Robotics*, vol. 4, no. 35, 10 2019.

[41] Y. Kim and X. Zhao, "Magnetic Soft Materials and Robots," *Chemical Reviews*, vol. 122, no. 5, pp. 5317–5364, 3 2022.

[42] V. K. Venkiteswaran, L. F. P. Samaniego, J. Sikorski, and S. Misra, "Bio-Inspired Terrestrial Motion of Magnetic Soft Millirobots," *IEEE Robotics and Automation Letters*, vol. 4, no. 2, pp. 1753–1759, 2019.

[43] J. A. Jackson, M. C. Messner, N. A. Dudukovic, W. L. Smith, L. Bekker, B. Moran, A. M. Golobic, A. J. Pascall, E. B. Duoss, K. J. Loh, and C. M. Spadaccini, "Field responsive mechanical metamaterials," *Sci. Adv.*, vol. 4, no. 12, pp. u6419, 12 2018.

[44] S. Wu, J. Eichenberger, J. Dai, Y. Chang, N. Ghalichechian, and R. R. Zhao, "Magnetically Actuated Reconfigurable Metamaterials

as Conformal Electromagnetic Filters," *Advanced Intelligent Systems*, vol. 4, no. 9, pp. 2200106, 9 2022.

[45] C. Ma, Y. Chang, S. Wu, and R. R. Zhao, "Deep Learning-Accelerated Designs of Tunable Magneto-Mechanical Metamaterials," *ACS Applied Materials and Interfaces*, 2022.

[46] T. Chen, M. Pauly, and P. M. Reis, "A reprogrammable mechanical metamaterial with stable memory," *Nature 2021 589:7842*, vol. 589, no. 7842, pp. 386–390, 1 2021.

[47] M. Y. Khalid, Z. U. Arif, A. Tariq, M. Hossain, K. Ahmed Khan, and R. Umer, "3D printing of magneto-active smart materials for advanced actuators and soft robotics applications," *European Polymer Journal*, vol. 205, pp. 112718, 2 2024.

[48] S. Wu, W. Hu, Q. Ze, M. Sitti, and R. Zhao, "Multifunctional magnetic soft composites: a review," *Multifunctional Materials*, vol. 3, no. 4, pp. 042003, 12 2020.

[49] Z. Qi, M. Zhou, Y. Li, Z. Xia, W. Huo, and X. Huang, "Reconfigurable Flexible Electronics Driven by Origami Magnetic Membranes," *Advanced Materials Technologies*, vol. 6, no. 4, pp. 2001124, 4 2021.

[50] C. Ma, S. Wu, Q. Ze, X. Kuang, R. Zhang, H. J. Qi, and R. Zhao, "Magnetic Multimaterial Printing for Multimodal Shape Transformation with Tunable Properties and Shiftable Mechanical Behaviors," *ACS Applied Materials and Interfaces*, vol. 13, no. 11, pp. 12 639–12 648, 3 2021.

[51] H.-W. Huang, M. S. Sakar, A. J. Petruska, S. Pané, and B. J. Nelson, "Soft micromachines with programmable motility and morphology," *Nature Communications*, vol. 7, no. 1, pp. 12263, 2016.

[52] Y. Kim, H. Yuk, R. Zhao, S. A. Chester, and X. Zhao, "Printing ferromagnetic domains for untethered fast-transforming soft materials," *Nature*, vol. 558, no. 7709, pp. 274–279, 6 2018.

[53] Y. Kim, G. A. Parada, S. Liu, and X. Zhao, "Ferromagnetic soft continuum robots," *Science Robotics*, vol. 4, no. 33, pp. eaax7329, 2019.

[54] W. Hu, G. Z. Lum, M. Mastrangeli, and M. Sitti, "Small-scale soft-bodied robot with multimodal locomotion," *Nature*, vol. 554, no. 7690, pp. 81–85, 2018.

[55] C. Wang, A. Mzyk, R. Schirhagl, S. Misra, and V. K. Venkiteswaran, "Biocompatible Film-Coating of Magnetic Soft Robots for Mucoadhesive Locomotion," *Advanced Materials Technologies*, vol. 8, no. 12, pp. 2201813, 6 2023.

[56] Z. Y. Wei, Z. V. Guo, L. Dudte, H. Y. Liang, and L. Mahadevan, "Geometric Mechanics of Periodic Pleated Origami," *Physical Review Letters*, vol. 110, no. 21, pp. 215501, 2013.

[57] C. Lv, D. Krishnaraju, G. Konjevod, H. Yu, and H. Jiang, "Origami based Mechanical Metamaterials," *Scientific Reports*, vol. 4, no. 1, pp. 5979, 2014.

[58] J. T. B. Overvelde, T. A. de Jong, Y. Shevchenko, S. A. Becerra, G. M. Whitesides, J. C. Weaver, C. Hoberman, and K. Bertoldi, "A three-dimensional actuated origami-inspired transformable metamaterial with multiple degrees of freedom," *Nature Communications*, vol. 7, no. 1, pp. 10929, 2016.

[59] J. U. Surjadi, Y. Zhou, S. Huang, L. Wang, M. Li, S. Fan, X. Li, J. Zhou, R. H. Lam, Z. Wang, and Y. Lu, "Lightweight, ultra-tough, 3D-architected hybrid carbon microlattices," *Matter*, 11 2022.

[60] H. Lee, Y. Jang, J. K. Choe, S. Lee, H. Song, J. P. Lee, N. Lone, and J. Kim, "3D-printed programmable tensegrity for soft robotics," *Science Robotics*, vol. 5, no. 45, 2020.

[61] X. Gong, K. Tan, Q. Deng, and S. Shen, "Athermal Shape Memory Effect in Magnetoactive Elastomers," *Cite This: ACS Appl. Mater. Interfaces*, vol. 12, pp. 16 930–16 936, 2020.

[62] P. Testa, R. W. Style, J. Cui, C. Donnelly, E. Borisova, P. M. Derlet, E. R. Dufresne, and L. J. Heyderman, "Magnetically Addressable

Shape-Memory and Stiffening in a Composite Elastomer," *Advanced Materials*, vol. 31, no. 29, pp. 1900561, 7 2019.

[63] J. Kim, S. E. Chung, S. E. Choi, H. Lee, J. Kim, and S. Kwon, "Programming magnetic anisotropy in polymeric microactuators," *Nature Materials 2011 10:10*, vol. 10, no. 10, pp. 747–752, 8 2011.

[64] Y. Zhang, C. Pan, P. Liu, L. Peng, Z. Liu, Y. Li, Q. Wang, T. Wu, Z. Li, C. Majidi, and L. Jiang, "Coaxially printed magnetic mechanical electrical hybrid structures with actuation and sensing functionalities," *Nature Communications 2023 14:1*, vol. 14, no. 1, pp. 1–15, 7 2023.

[65] M. Y. Khalid, Z. U. Arif, R. Noroozi, M. Hossain, S. Ramakrishna, and R. Umer, "3D/4D printing of cellulose nanocrystals-based biomaterials: Additives for sustainable applications," *International Journal of Biological Macromolecules*, vol. 251, pp. 126287, 11 2023.

[66] Y. Alapan, A. C. Karacakol, S. N. Guzelhan, I. Isik, and M. Sitti, "Reprogrammable shape morphing of magnetic soft machines," *Science Advances*, vol. 6, no. 38, pp. eabc6414, 2020.

[67] H. Song, H. Lee, J. Lee, J. K. Choe, S. Lee, J. Y. Yi, S. Park, J. W. Yoo, M. S. Kwon, and J. Kim, "Reprogrammable Ferromagnetic Domains for Reconfigurable Soft Magnetic Actuators," *Nano Letters*, vol. 20, no. 7, pp. 5185–5192, 7 2020.

[68] W.-F. Chen and T. Atsuta, "Theory of beam-columns. Volume 1, In-plane behavior and design," pp. 513, 2008.

[69] C. Coulais, J. T. B. Overvelde, L. A. Lubbers, K. Bertoldi, and M. Van Hecke, "Discontinuous Buckling of Wide Beams and Metabeams," 2015.

[70] J. Rahmer, C. Stehning, and B. Gleich, "Spatially selective remote magnetic actuation of identical helical micromachines," *Science Robotics*, vol. 2, no. 3, 2 2017.

[71] T. Xu, J. Zhang, M. Salehizadeh, O. Onaizah, and E. Diller, "Millimeter-scale flexible robots with programmable three-

dimensional magnetization and motions," *Science Robotics*, vol. 4, no. 29, 4 2019.

[72] S. W. Kwok, S. A. Morin, B. Mosadegh, J. H. So, R. F. Shepherd, R. V. Martinez, B. Smith, F. C. Simeone, A. A. Stokes, and G. M. Whitesides, "Magnetic Assembly of Soft Robots with Hard Components," *Advanced Functional Materials*, vol. 24, no. 15, pp. 2180–2187, 4 2014.

[73] Z. Wang, W. Li, A. Klingner, Y. Pei, S. Misra, and I. S. Khalil, "Magnetic control of soft microrobots near step-out frequency: Characterization and analysis," *Computational and Structural Biotechnology Journal*, vol. 25, pp. 165–176, 12 2024.

[74] J. Cui, T.-Y. Huang, Z. Luo, P. Testa, H. Gu, X.-Z. Chen, B. J. Nelson, and L. J. Heyderman, "Nanomagnetic encoding of shape-morphing micromachines," *Nature*, vol. 575, 2019.

[75] M. Han, X. Guo, X. Chen, C. Liang, H. Zhao, Q. Zhang, W. Bai, F. Zhang, H. Wei, C. Wu, Q. Cui, S. Yao, B. Sun, Y. Yang, Q. Yang, Y. Ma, Z. Xue, J. W. Kwak, T. Jin, Q. Tu, E. Song, Z. Tian, Y. Mei, D. Fang, H. Zhang, Y. Huang, Y. Zhang, and J. A. Rogers, "Submillimeter-scale multimaterial terrestrial robots," *Science Robotics*, vol. 7, no. 66, 8 2022.

[76] C. Xu, C. F. Faul, M. Taghavi, and J. Rossiter, "Electric Field-Driven Dielectrophoretic Elastomer Actuators," *Advanced Functional Materials*, vol. 33, no. 13, pp. 2208943, 3 2023.

[77] H. Yang, S. Li, Y. Wu, X. Bao, Z. Xiang, Y. Xie, L. Pan, J. Chen, Y. Liu, and R. W. Li, "Advances in Flexible Magnetosensitive Materials and Devices for Wearable Electronics," 2024.

[78] Y. Li, Z. Chen, G. Zheng, W. Zhong, L. Jiang, Y. Yang, L. Jiang, Y. Chen, and C. P. Wong, "A magnetized microneedle-array based flexible triboelectric-electromagnetic hybrid generator for human motion monitoring," *Nano Energy*, vol. 69, pp. 104415, 3 2020.

[79] G. Yan, A. A. Solovev, G. Huang, J. Cui, and Y. Mei, "Soft microswimmers: Material capabilities and biomedical applications,"

*Current Opinion in Colloid & Interface Science*, vol. 61, pp. 101609, 10 2022.

[80] R. Yin, D. Wang, S. Zhao, Z. Lou, and G. Shen, "Wearable Sensors-Enabled Human–Machine Interaction Systems: From Design to Application," 3 2021.

[81] H. Zhang, D. Zhang, Z. Wang, G. Xi, R. Mao, Y. Ma, D. Wang, M. Tang, Z. Xu, and H. Luan, "Ultrastretchable, Self-Healing Conductive Hydrogel-Based Triboelectric Nanogenerators for Human-Computer Interaction," *ACS Applied Materials and Interfaces*, vol. 15, no. 4, pp. 5128–5138, 2 2023.

[82] M. Richter, M. Kaya, J. Sikorski, L. Abelmann, V. Kalpathy Venkiteswaran, and S. Misra, "Magnetic Soft Helical Manipulators with Local Dipole Interactions for Flexibility and Forces," *Soft Robotics*, vol. 10, no. 3, pp. 647–659, 6 2023.

[83] J. Liu, S. Yu, B. Xu, Z. Tian, H. Zhang, K. Liu, X. Shi, Z. Zhao, C. Liu, X. Lin, G. Huang, A. A. Solovev, J. Cui, T. Li, and Y. Mei, "Magnetically propelled soft microrobot navigating through constricted microchannels," *Applied Materials Today*, vol. 25, pp. 101237, 12 2021.

[84] H. Torlakcik, S. Sevim, P. Alves, M. Mattmann, J. Llacer-Wintle, M. Pinto, R. Moreira, A. D. Flouris, F. C. Landers, X. Z. Chen, J. Puigmartí-Luis, Q. Boehler, T. S. Mayor, M. Kim, B. J. Nelson, and S. Pané, "Magnetically Guided Microcatheter for Targeted Injection of Magnetic Particle Swarms," *Advanced Science*, vol. 11, no. 38, pp. 2404061, 10 2024.

[85] C. Li, S. Misra, and I. S. Khalil, "Navigation of Untethered Small-Scale Helical Devices Using Magnetic System under Ultrasound Guidance," *IEEE Transactions on Medical Robotics and Bionics*, vol. 5, no. 4, pp. 1093–1104, 11 2023.

[86] S. Miyashita, S. Guitron, S. Li, and D. Rus, "Robotic metamorphosis by origami exoskeletons," *Science Robotics*, vol. 2, no. 10, 9 2017.

[87] G. Z. Lum, Z. Ye, X. Dong, H. Marvi, O. Erin, W. Hu, and M. Sitti, "Shape-programmable magnetic soft matter," *Proceedings of the National Academy of Sciences of the United States of America*, vol. 113, no. 41, pp. E6007–E6015, 10 2016.

[88] R. Sanchis-Gual, H. Ye, T. Ueno, F. C. Landers, L. Hertle, S. Deng, A. Veciana, Y. Xia, C. Franco, H. Choi, J. Puigmartí-Luis, B. J. Nelson, X. Z. Chen, and S. Pané, "3D Printed Template-Assisted Casting of Biocompatible Polyvinyl Alcohol-Based Soft Microswimmers with Tunable Stability," *Advanced Functional Materials*, vol. 33, no. 39, pp. 2212952, 9 2023.

[89] S. Zhang, Y. Xu, Z. Li, Y. Li, Z. Lu, X. Chen, P. Chen, M. Chen, P. Zhang, C. Cai, Q. Wang, and B. Su, "Ultra-Fast Shape-Deformation and Highly-Sensitive Detection of 4D Printed Electromagnetic Architectures," *Advanced Functional Materials*, vol. 34, no. 38, pp. 2402563, 9 2024.

[90] H. Deng, K. Sattari, Y. Xie, P. Liao, Z. Yan, and J. Lin, "Laser reprogramming magnetic anisotropy in soft composites for reconfigurable 3D shaping," *Nature Communications 2020 11:1*, vol. 11, no. 1, pp. 1–10, 12 2020.

[91] C. Chen, C. Ran, Q. Yao, J. Wang, C. Guo, L. Gu, H. Han, X. Wang, L. Chao, Y. Xia, and Y. Chen, "Screen-Printing Technology for Scale Manufacturing of Perovskite Solar Cells," *Advanced Science*, vol. 10, no. 28, pp. 2303992, 10 2023.

[92] N. Kapur, S. J. Abbott, E. D. Dolden, and P. H. Gaskell, "Predicting the Behavior of Screen Printing," *IEEE Transactions on Components, Packaging and Manufacturing Technology*, vol. 3, no. 3, 2013.

[93] Z. Taleat, A. Khoshroo, and M. Mazloum-Ardakani, "Screen-printed electrodes for biosensing: A review (2008-2013)," *Microchimica Acta*, vol. 181, no. 9-10, pp. 865–891, 4 2014.

[94] S. Taufiq, M. Waqar, M. N. Sharif, and S. R. Abbas, "Towards portable rapid TB biosensor: Detecting Mycobacterium tuberculosis in raw sputum samples using functionalized screen printed electrodes," *Bioelectrochemistry*, vol. 150, pp. 108353, 4 2023.

[95] S. Bonaldo, E. Cretaio, E. Pasqualotto, M. Scaramuzza, L. Franchin, S. Poggi, and A. Paccagnella, "Screen-Printed Electrochemical Biosensor for the Detection of Bacteriophage of Lactococcus Lactis for Dairy Production," *IEEE Sensors Journal*, vol. 23, no. 6, pp. 5552–5560, 3 2023.

[96] Y. Hu, Z. Zhang, A. Mei, Y. Jiang, X. Hou, Q. Wang, K. Du, Y. Rong, Y. Zhou, G. Xu, and H. Han, "Improved Performance of Printable Perovskite Solar Cells with Bifunctional Conjugated Organic Molecule," *Advanced Materials*, vol. 30, no. 11, pp. 1705786, 3 2018.

[97] J. Ryu, K. Lee, J. Yun, H. Yu, J. Lee, and J. Jang, "Paintable Carbon-Based Perovskite Solar Cells with Engineered Perovskite/Carbon Interface Using Carbon Nanotubes Dripping Method," *Small*, vol. 13, no. 38, pp. 1701225, 10 2017.

[98] W. J. Hyun, E. B. Secor, M. C. Hersam, C. D. Frisbie, and L. F. Francis, "High-Resolution Patterning of Graphene by Screen Printing with a Silicon Stencil for Highly Flexible Printed Electronics," *Advanced Materials*, vol. 27, no. 1, pp. 109–115, 1 2015.

[99] J. Liang, K. Tong, and Q. Pei, "A Water-Based Silver-Nanowire Screen-Print Ink for the Fabrication of Stretchable Conductors and Wearable Thin-Film Transistors," *Advanced Materials*, vol. 28, no. 28, pp. 5986–5996, 7 2016.

[100] H. Ren, X. Zhang, Q. Liu, W. Tang, J. Liang, and W. Wu, "Fully-Printed Flexible Aqueous Rechargeable Sodium-Ion Batteries," *Small*, vol. 20, no. 28, pp. 2312207, 7 2024.

[101] P. Molaiyan, J. Valikangas, R. Sliz, D. D. Ramteke, T. Hu, A. Paolella, T. Fabritius, and U. Lassi, "Screen-Printed Composite LiFePO4-LLZO Cathodes Towards Solid-State Li-ion Batteries," *ChemElectroChem*, vol. 11, no. 9, pp. e202400051, 5 2024.

[102] T. Y. Kim, C. Y. Im, J. H. Choi, D. Gu, S. Yoon, U.-H. Kim, and S. J. Kim, "Fabrication of a Porous Copper/Graphite/Zirconium Oxide Hybrid Anode via Screen Printing for Lithium-Ion Batteries," *Advanced Functional Materials*, pp. 2411648, 2024.

[103] A. Gören, J. Mendes, H. M. Rodrigues, R. E. Sousa, J. Oliveira, L. Hilliou, C. M. Costa, M. M. Silva, and S. Lanceros-Méndez, "High performance screen-printed electrodes prepared by a green solvent approach for lithium-ion batteries," *Journal of Power Sources*, vol. 334, pp. 65–77, 12 2016.

[104] J. Liu, X. Jiang, R. Zhang, Y. Zhang, L. Wu, W. Lu, J. Li, Y. Li, and H. Zhang, "MXene-Enabled Electrochemical Microfluidic Biosensor: Applications toward Multicomponent Continuous Monitoring in Whole Blood," *Advanced Functional Materials*, vol. 29, no. 6, pp. 1807326, 2 2019.

[105] X. Jin, G. Li, T. Xu, L. Su, D. Yan, and X. Zhang, "Fully integrated flexible biosensor for wearable continuous glucose monitoring," *Biosensors and Bioelectronics*, vol. 196, pp. 113760, 1 2022.

[106] F. C. Krebs, "Fabrication and processing of polymer solar cells: A review of printing and coating techniques," *Solar Energy Materials and Solar Cells*, vol. 93, no. 4, pp. 394–412, 4 2009.

[107] L. Yu, Z. Fan, Y. Shao, Z. Tian, J. Sun, and Z. Liu, "Versatile N-Doped MXene Ink for Printed Electrochemical Energy Storage Application," *Advanced Energy Materials*, vol. 9, no. 34, pp. 1901839, 9 2019.

[108] S. Abdolhosseinzadeh, R. Schneider, A. Verma, J. Heier, F. Nüesch, and C. Zhang, "Turning Trash into Treasure: Additive Free MXene Sediment Inks for Screen-Printed Micro-Supercapacitors," *Advanced Materials*, vol. 32, no. 17, pp. 2000716, 4 2020.

[109] N. Zavanelli and W.-H. Yeo, "Advances in Screen Printing of Conductive Nanomaterials for Stretchable Electronics," 2021.

[110] Y. Bai, H. Wang, Y. Xue, Y. Pan, J. T. Kim, X. Ni, T. L. Liu, Y. Yang, M. Han, Y. Huang, J. A. Rogers, and X. Ni, "A dynamically reprogrammable surface with self-evolving shape morphing," *Nature 2022 609:7928*, vol. 609, no. 7928, pp. 701–708, 9 2022.

[111] S. Zou, S. Picella, J. de Vries, V. G. Kortman, A. Sakes, and J. T. Overvelde, "A retrofit sensing strategy for soft fluidic robots," *Nature Communications 2024 15:1*, vol. 15, no. 1, pp. 1–12, 1 2024.

[112] J. Shintake, V. Cacucciolo, D. Floreano, and H. Shea, "Soft Robotic Grippers," *Advanced Materials*, vol. 30, no. 29, pp. 1707035, 7 2018.

[113] L. Zhou, L. Ren, Y. Chen, S. Niu, Z. Han, and L. Ren, "Bio-Inspired Soft Grippers Based on Impactive Gripping," *Advanced Science*, vol. 8, no. 9, pp. 2002017, 5 2021.

[114] I. B. Andika, S. Wei, C. Cao, L. Salaipeth, H. Kondo, and L. Sun, "Phytopathogenic fungus hosts a plant virus: A naturally occurring cross-kingdom viral infection," *Proceedings of the National Academy of Sciences of the United States of America*, vol. 114, no. 46, pp. 12 267–12 272, 11 2017.

[115] M.-L. Jeng and M.-L. Jeng, "Biofluorescence in Terrestrial Animals, with Emphasis on Fireflies: A Review and Field Observation," *Bioluminescence - Analytical Applications and Basic Biology*, 8 2019.

[116] Z. Wang, S. Misra, and V. K. Venkiteswaran, "Fluidic control programming for 3D magnetic soft metamaterials with reconfigurable mechanical behaviors," *Cell Reports Physical Science*, vol. 5, no. 8, 8 2024.

[117] S. S. Rao, C. D. Holdsworth, and N. W. Read, "Symptoms and stool patterns in patients with ulcerative colitis," *Gut*, vol. 29, no. 3, pp. 342–345, 3 1988.

[118] C. Le Berre, S. Honap, and L. Peyrin-Biroulet, "Ulcerative colitis," *The Lancet*, vol. 402, no. 10401, pp. 571–584, 8 2023.

[119] A. Lavelle and H. Sokol, "Gut microbiota-derived metabolites as key actors in inflammatory bowel disease," *Nature Reviews Gastroenterology & Hepatology 2020 17:4*, vol. 17, no. 4, pp. 223–237, 2 2020.

[120] J. R. Turner, "Intestinal mucosal barrier function in health and disease," *Nature Reviews Immunology 2009 9:11*, vol. 9, no. 11, pp. 799–809, 11 2009.

[121] J. Fang, H. Wang, Y. Zhou, H. Zhang, H. Zhou, and X. Zhang, "Slimy partners: the mucus barrier and gut microbiome in ulcerative colitis," *Experimental & Molecular Medicine 2021 53:5*, vol. 53, no. 5, pp. 772–787, 5 2021.

[122] J. Ni, G. D. Wu, L. Albenberg, and V. T. Tomov, "Gut microbiota and IBD: Causation or correlation?" *Nature Reviews Gastroenterology and Hepatology*, vol. 14, no. 10, pp. 573–584, 10 2017.

[123] C. Manichanh, N. Borruel, F. Casellas, and F. Guarner, "The gut microbiota in IBD," *Nature Reviews Gastroenterology & Hepatology 2012 9:10*, vol. 9, no. 10, pp. 599–608, 8 2012.

[124] G. G. Kaplan, "The global burden of IBD: From 2015 to 2025," *Nature Reviews Gastroenterology and Hepatology*, vol. 12, no. 12, pp. 720–727, 12 2015.

[125] J. Burisch, M. Zhao, S. Odes, P. De Cruz, S. Vermeire, C. N. Bernstein, G. G. Kaplan, D. Duricova, D. Greenberg, H. O. Melberg, M. Watanabe, H. S. Ahn, L. Targownik, V. E. Pittet, V. Annese, K. T. Park, K. H. Katsanos, M. L. Høivik, Z. Krznaric, M. Chaparro, E. V. Loftus, P. L. Lakatos, J. P. Gisbert, W. Bemelman, B. Moum, R. B. Gearry, M. D. Kappelman, A. Hart, M. J. Pierik, J. M. Andrews, S. C. Ng, R. D'Inca, and P. Munkholm, "The cost of inflammatory bowel disease in high-income settings: a Lancet Gastroenterology & Hepatology Commission," *The Lancet Gastroenterology and Hepatology*, vol. 8, no. 5, pp. 458–492, 5 2023.

[126] G. Ianiro, M. Punčochář, N. Karcher, S. Porcari, F. Armanini, F. Asnicar, F. Beghini, A. Blanco-Míguez, F. Cumbo, P. Manghi, F. Pinto, L. Masucci, G. Quaranta, S. De Giorgi, G. D. Sciumè, S. Bibbò, F. Del Chierico, L. Putignani, M. Sanguinetti, A. Gasbarrini, M. Valles-Colomer, G. Cammarota, and N. Segata, "Variability of strain engraftment and predictability of microbiome composition after fecal microbiota transplantation across different diseases," *Nature Medicine 2022 28:9*, vol. 28, no. 9, pp. 1913–1923, 9 2022.

[127] T. S. Schmidt, S. S. Li, O. M. Maistrenko, W. Akanni, L. P. Coelho, S. Dolai, A. Fullam, A. M. Glazek, R. Hercog, H. Herrema, F. Jung, S. Kandels, A. Orakov, R. Thielemann, M. von Stetten, T. Van Rossum, V. Benes, T. J. Borody, W. M. de Vos, C. Y. Ponsioen, M. Nieuwdorp, and P. Bork, "Drivers and determinants of strain dynamics following fecal microbiota transplantation," *Nature Medicine 2022 28:9*, vol. 28, no. 9, pp. 1902–1912, 9 2022.

[128] A. Boicean, V. Birlutiu, C. Ichim, P. Anderco, and S. Birsan, "Fecal Microbiota Transplantation in Inflammatory Bowel Disease," *Biomedicines*, vol. 11, no. 4, pp. 1016, 4 2023.

[129] M. R. Charbonneau, V. M. Isabella, N. Li, and C. B. Kurtz, "Developing a new class of engineered live bacterial therapeutics to treat human diseases," *Nature Communications 2020 11:1*, vol. 11, no. 1, pp. 1738–, 4 2020.

[130] C. B. Kurtz, Y. A. Millet, M. K. Puurunen, M. Perreault, M. R. Charbonneau, V. M. Isabella, J. W. Kotula, E. Antipov, Y. Dagon, W. S. Denney, D. A. Wagner, K. A. West, A. J. Degar, A. M. Brennan, and P. F. Miller, "An engineered E. Coli Nissle improves hyperammonemia and survival in mice and shows dose-dependent exposure in healthy humans," *Science Translational Medicine*, vol. 11, no. 475, 1 2019.

[131] J. P. Haran and B. A. McCormick, "Aging, Frailty, and the Microbiome—How Dysbiosis Influences Human Aging and Disease," *Gastroenterology*, vol. 160, no. 2, pp. 507–523, 1 2021.

[132] Y. Fan and O. Pedersen, "Gut microbiota in human metabolic health and disease," *Nature Reviews Microbiology 2020 19:1*, vol. 19, no. 1, pp. 55–71, 9 2020.

[133] Z. Cao, X. Wang, Y. Pang, S. Cheng, and J. Liu, "Biointerfacial self-assembly generates lipid membrane coated bacteria for enhanced oral delivery and treatment," *Nature Communications 2019 10:1*, vol. 10, no. 1, pp. 5783–, 12 2019.

[134] Q. Song, C. Zheng, J. Jia, H. Zhao, Q. Feng, H. Zhang, L. Wang, Z. Zhang, and Y. Zhang, "A Probiotic Spore-Based Oral Autonomous Nanoparticles Generator for Cancer Therapy," *Advanced Materials*, vol. 31, no. 43, pp. 1903793, 10 2019.

[135] M. Schultz, "Clinical use of E. coli Nissle 1917 in inflammatory bowel disease," *Inflammatory Bowel Diseases*, vol. 14, no. 7, pp. 1012–1018, 7 2008.

[136] J. Zhou, M. Li, Q. Chen, X. Li, L. Chen, Z. Dong, W. Zhu, Y. Yang, Z. Liu, and Q. Chen, "Programmable probiotics modulate inflammation and gut microbiota for inflammatory bowel disease treatment after effective oral delivery," *Nature Communications 2022 13:1*, vol. 13, no. 1, pp. 1–14, 6 2022.

[137] L. Huang, W. Tang, L. He, M. Li, X. Lin, A. Hu, X. Huang, Z. Wu, Z. Wu, S. Chen, and Y. Hu, "Engineered probiotic Escherichia coli elicits immediate and long-term protection against influenza A virus in mice," *Nature Communications 2024 15:1*, vol. 15, no. 1, pp. 6802–, 8 2024.

[138] J. L. Round and S. K. Mazmanian, "The gut microbiota shapes intestinal immune responses during health and disease," *Nature Reviews Immunology 2009 9:5*, vol. 9, no. 5, pp. 313–323, 5 2009.

[139] N. Arpaia, C. Campbell, X. Fan, S. Dikiy, J. Van Der Veeken, P. Deroos, H. Liu, J. R. Cross, K. Pfeffer, P. J. Coffer, and A. Y. Rudensky, "Metabolites produced by commensal bacteria promote peripheral regulatory T-cell generation," *Nature 2013 504:7480*, vol. 504, no. 7480, pp. 451–455, 11 2013.

[140] R. Verma, C. Lee, E. J. Jeun, J. Yi, K. S. Kim, A. Ghosh, S. Byun, C. G. Lee, H. J. Kang, G. C. Kim, C. D. Jun, G. Jan, C. H. Suh, J. Y. Jung, J. Sprent, D. Rudra, C. De Castro, A. Molinaro, C. D. Surh, and S. H. Im, "Cell surface polysaccharides of Bifidobacterium bifidum induce the generation of Foxp3+ regulatory T cells," *Science Immunology*, vol. 3, no. 28, 10 2018.

[141] M. K. Heavey, D. Durmusoglu, N. Crook, and A. C. Anselmo, "Discovery and delivery strategies for engineered live biotherapeutic products," *Trends in Biotechnology*, vol. 40, no. 3, pp. 354–369, 3 2022.

[142] X. Cao, S. Tao, W. Wang, S. Wu, Y. Hong, X. Wang, Y. Ma, H. Qian, and Z. Zha, "Ternary inulin hydrogel with long-term intestinal retention for simultaneously reversing IBD and its fibrotic complication," *Nature Communications 2024 15:1*, vol. 15, no. 1, pp. 8428–, 9 2024.

[143] J. Liu, Y. Wang, W. J. Heelan, Y. Chen, Z. Li, and Q. Hu, "Mucoadhesive probiotic backpacks with ROS nanoscavengers enhance

the bacteriotherapy for inflammatory bowel diseases," *Science Advances*, vol. 8, no. 45, pp. 8798, 11 2022.

[144] M. Cui, T. Sun, S. Li, H. Pan, J. Liu, X. Zhang, L. Li, S. Li, C. Wei, C. Yu, C. Yang, N. Ma, B. Ma, S. Lu, J. Chang, W. Zhang, and H. Wang, "NIR light-responsive bacteria with live bio-glue coatings for precise colonization in the gut," *Cell Reports*, vol. 36, no. 11, pp. 109690, 9 2021.

[145] H. Liu, Z. Chen, Q. Lin, Y. Chen, L. Hong, J. Zhong, Z. Cai, Z. Wang, and W. Cui, "A multicellular self-organized probiotic platform for oral delivery enhances intestinal colonization," *Nature Communications 2025 16:1*, vol. 16, no. 1, pp. 7060–, 8 2025.

[146] Y. Sun, W. Zhang, J. Gu, L. Xia, Y. Cao, X. Zhu, H. Wen, S. Ouyang, R. Liu, J. Li, Z. Jiang, D. Cheng, Y. Lv, X. Han, W. Qiu, K. Cai, E. Song, Q. Cao, and L. Li, "Magnetically driven capsules with multimodal response and multifunctionality for biomedical applications," *Nature Communications 2024 15:1*, vol. 15, no. 1, pp. 1839–, 2 2024.

[147] Z. Chen, Y. Wang, H. Chen, J. Law, H. Pu, S. Xie, F. Duan, Y. Sun, N. Liu, and J. Yu, "A magnetic multi-layer soft robot for on-demand targeted adhesion," *Nature Communications 2024 15:1*, vol. 15, no. 1, pp. 644–, 1 2024.

[148] C. Wang, V. R. Puranam, S. Misra, and V. K. Venkiteswaran, "A Snake-Inspired Multi-Segmented Magnetic Soft Robot Towards Medical Applications," *IEEE Robotics and Automation Letters*, vol. 7, no. 2, pp. 5795–5802, 4 2022.

# Acknowledgements

Completing this PhD represents a milestone of profound personal significance to me. It is not only the culmination of years of research, but also the outcome of a long intellectual journey shaped by my enduring curiosity about the world. My academic journey began in civil engineering. As I developed a deeper understanding of structures and mechanics, I became increasingly interested in how materials behave and how structures are constructed across different scales. This curiosity led me to materials science, where I studied nanomaterials and energy devices fabricated from them. Gradually, I came to realize that these materials could also be applied in biomedical contexts, which ultimately inspired me to pursue a PhD in biomedical engineering. Looking back, I am first and foremost grateful that I have never lost my curiosity about the world. I am grateful to all those who accepted and supported my pursuit of new fields, tolerated the uncertainties and detours along the way, and offered their help whenever I needed it.

**Prof. Sarthak Misra** was the first person who made this journey possible. Sarthak, thank you for building a team with such a diverse range of interdisciplinary backgrounds and for welcoming me as one of its members. The Surgical Robotics Lab (SRL) is an inclusive, open-minded, and innovative environment. During my time in the group, I received rigorous and comprehensive scientific training that will remain fundamental to my future research. Thank you for supporting me during the moments when I felt confused, uncertain, or overwhelmed by the challenges ahead. I sincerely believe that we will continue to collaborate and support one another in the future.

Throughout my PhD, **Dr. Venkat Kalpathy Venkiteswaran** provided meticulous guidance on my research. Venkat, our weekly meetings recorded the progress of our work as well as countless moments from our lives. Thank you for bringing me back to practical considerations whenever I arrived with another "crazy" idea, for offering constructive suggestions when something seemed impossible, and for comforting and encouraging me whenever I lost my direction. My greatest regret is that the time we could spend together was far too short. I believe that our relationship has

long since grown beyond that between a PhD candidate and a supervisor. I sincerely hope you and your family all the best and hope that we will remain close and continue our collaboration in the years to come.

I would like to express my sincere gratitude to the members of my thesis assessment committee: **Prof. Bas Overvelde** from Eindhoven University of Technology, **Prof. Romana Schirhagl** from the University of Groningen, and **Dr. Ali Sadeghi** from the University of Twente. I greatly appreciate your careful evaluation of this thesis, your kind comments, and your valuable suggestions. I would also like to thank **Prof. Patrick Onck** and **Prof. Anastasiia Krushynska** from the University of Groningen, as well as **Dr. Malte Asseln** from University of Twente, for kindly agreeing to serve on my doctoral examination committee.

I am grateful to my collaborators, **Dr. Li Ding** and **Dalin Zhang**, for their invaluable assistance with the animal experiments presented in Chapter 4 of this thesis. Your expertise, effort, and support were essential to the completion of this work.

My sincere thanks go to all the members of SRL. You made me feel that I was never alone as I moved forward along this demanding path. **Chen** and **Yiling**, thank you for your kindness and support, especially during my first year, when I arrived in the Netherlands on my own. Chen, thank you for serving as my paranymph. Your persistence and dedication to research have always impressed me. I remain amazed by your ability to get to know so many people and by the fact that everyone likes you. Some of my fondest memories in Groningen are the hours we spent playing pool and going fishing together. Congratulations to you and Yiling on your marriage. I wish you both a lifetime of happiness. **Kaixuan**, thank you for your companionship throughout these years. I have always admired your rigorous and professional attitude towards your work. Because you were usually in the office in the afternoons, we often had dinner together. I always enjoyed our conversations, especially because your stories were invariably entertaining. Our trip to Italy remains one of my most unforgettable memories. Now that we are both in Shenzhen, I hope that we will have many more opportunities to collaborate and travel together. Congratulations to you and Mengyu on your marriage. **Zihan**, thank you for always being willing to listen to my endless thoughts and complaints, and for consistently offering comfort and reassurance. I spent much of my final few months in Groningen with you. I am sorry that, during one of

the most anxious and uncertain periods of my life, I placed so much of my negative energy on you. You always possess remarkable clarity of thought and a disciplined approach to work—qualities that I greatly admire. I wish you every success in your work in Suzhou and much happiness in your life. **Chuang**, thank you for taking care of me in the laboratory, for helping me operate the ultrasound equipment, and for helping me with so many instruments and materials. I miss the table-football matches after lunch with you, Chen, Kaixuan, and Zihan. To this day, we have still not determined who the true winner is. I wish you success in your work in Liaoning and happiness for you and your family. **Zhengya**, thank you for all your help in the laboratory. When I was struggling with the mechanical testing, you proactively helped me obtain a motor slide and generously allowed me to use your own equipment. Thank you also for inviting me for dinner so often. I miss the days when we could talk freely about everything and nothing. **Yiyang**, thank you for sharing so many interesting stories about your experiences in the Netherlands. **Adriana**, conversations with you were always enjoyable. I wish you a smooth, fulfilling, and successful PhD journey in Groningen. **Michiel**, thank you for helping me magnetize the magnetic particles. Your assistance saved me from making repeated journeys to Enschede over the course of two years, and I am sincerely grateful for your support. **Christoff**, thank you for your efficiency and professionalism, which made our collaboration both productive and enjoyable. I wish you every success in your career. **Yu-Hsiang**, I always enjoyed discussing ideas with you because you were consistently kind, approachable, and humble. Wish you all the best. **Sumit**, I greatly admire your cheerful and optimistic personality, which allows you to connect so naturally with everyone around you. Your positive presence brought energy and warmth to the group. I would also like to thank the other members and alumni of SRL—**Islam**, **Juan**, **Yuxin**, **Tao**, **Jeanine**, **Simon**, **Lukas**, **Antonio**, **Mert**, **Amin**, and **Theodosia**. Thank you for your support, collaboration, and friendship, and for making SRL such a welcoming, ambitious, and inspiring team.

It has also been a great privilege to be part of the Department of Biomaterials and Biomedical Technology (BBT) at the University Medical Center Groningen (UMCG). **Tianqi**, I was fortunate to have our lab next to your office. You always greeted the world with a smile, and your optimism was as infectious as sunlight. I wish you and **Haoyang** every success in Shen-

zhen, and I hope that we will be able to meet often in the future. **Han**, it was a great pleasure and privilege to sit beside you for years. I wish you every success in your career and your life. **Ruichen**, thank you for your generous help with my experiments. I wish you all the best in everything that lies ahead. **Dize**, I still regret that I did not manage to travel to Switzerland with you. I greatly admire your professionalism and your serious attitude towards research. Congratulations on your marriage, and I wish you every success in your work and life in Chongqing. **Yuzhu**, thank you for your help and advice when I felt uncertain about my career. Your support allowed me to approach important decisions with greater clarity and confidence. **Helder**, thank you for your outstanding leadership and for everything you have done to develop the department into a friendly, inclusive, diverse, and advanced research community. I am particularly grateful for your kind assistance when I was applying for postdoctoral positions. Your support at that important stage of my career meant a great deal to me. **Ed**, thank you for your technical support. You were always friendly and willing to help, and your work ensured that both our laboratories and offices operated smoothly. **Joop**, thank you for your assistance with surface-characterization measurements and mechanical-testing equipment. Your expertise and patience helped me overcome many practical difficulties. **Willem**, thank you for providing the equipment training that allowed me to conduct my experiments safely and independently. **Marja**, **Willy**, **Betsy**, **Jelly**, and **Wytse**, thank you for your help with purchasing, administration, and financial matters. Your work behind the scenes made our research possible and our daily lives considerably easier. I would also like to thank my colleagues and alumni in the department—**Yuewen**, **Yanjing**, **Fenghua**, **Yuanyuan**, **Yong**, **Sidi**, **Guimei**, **Siyu**, **Jiachen**, and **Kaiqi**. Thank you for the conversations, meals, shared experiences, and support that became such an important part of my memories at UMCG.

My thanks also go to my friends at **Snookervereniging Groningen**. Playing snooker at the club was one of the most memorable parts of my life in Groningen. The games, conversations, and friendships offered a welcome balance to the demands of doctoral research.

Finally, none of this would have been possible without my family. Thank you for the love, trust, and unwavering support you have given me over so many years. To my parents, thank you for giving me the freedom and security to pursue the career and interests that I truly love. You

always inspire me to be curious to the world and always encourage me to find my own path. Everything I have achieved rests upon the opportunities, encouragement, and unconditional support you provided. To my grandparents, thank you for your love. Your care and encouragement have continually given me the strength to move forward. To my parents-in-law, thank you for your trust and for your constant support of me and Jie. Your understanding and generosity have been a source of great reassurance throughout these years. To **Bin**, my brother-in-law, I hope that I can pass on to you some of the love and encouragement that I have received from our family. May you always have the courage to follow your own dreams and to create a life that is truly your own.

Dear **Jie**, my beloved wife, being with you is the most romantic decision I have ever made. Thank you for caring for me in every possible way and for standing beside me through every stage of this journey. Everything we have experienced together has already surpassed all the happiness I once imagined life could hold. Whatever joys and challenges await us in the future, I want to experience them all with you.

# About the author

Zhuoyue Wang was born on $15^{th}$ November 1995 in Gansu province, China. He received his Bachelor of Engineering in Civil Engineering from Lanzhou University, China, in 2018. During his undergraduate studies, he investigated negative friction in pile foundations triggered by collapsible loess funded by Tsung-Dao Lee. He then pursued a Master of Engineering in Structural Engineering at Lanzhou University (2018–2021). His master's research focused on 3D-printed graphene-based energy devices for solar energy conversion, supercapacitors, soft electronics, and anodes for sodium batteries.

In 2021, he began his PhD in Biomedical Engineering at the University Medical Center Groningen and the University of Groningen, Groningen, the Netherlands, under the supervision of Prof. Sarthak Misra and Dr. Venkatasubramanian Kalpathy Venkiteswaran. His doctoral research focuses on the design, scalable fabrication, and control of magnetic soft robots for biomedical applications, including 3D magnetization programming, multi-layer screen-printing of magnetic soft robots, and targeted probiotic delivery to enhance intestinal microbial colonization.